Insights into the Controllable Chemical Composition of Metal Oxide Nanowires and Graphene Aerogels

by

Anna Patrice Goldstein

A dissertation submitted in partial satisfaction of the
requirements for the degree of
Doctor of Philosophy
in
Chemistry
and the Designated Emphasis
in
Nanoscale Science and Engineering
in the
Graduate Division
of the
University of California, Berkeley

Committee in charge:
Professor Alex Zettl, Co-Chair
Professor Peidong Yang, Co-Chair
Professor Tanja Cuk
Professor Junqiao Wu

Fall 2014

Abstract

Insights into the Controllable Chemical Composition of Metal Oxide Nanowires and Graphene Aerogels

Anna Patrice Goldstein

Doctor of Philosophy in Chemistry

University of California, Berkeley

Professor Alex Zettl, Co-Chair

Professor Peidong Yang, Co-Chair

The goal of engineering materials that absorb visible light and create fuel to store solar energy has captivated chemists for decades. In order to take part in solar water splitting, i.e. the production of hydrogen and oxygen gas from water and sunlight, electrodes must fit specific requirements in terms of their electronic structure. Zinc oxide (ZnO) and titanium dioxide (TiO_2) are both of interest for their ability to produce oxygen from photogenerated holes, but their band gaps are too large to capture a significant portion of the solar spectrum. We address this challenge by modifying the crystal structures of ZnO and TiO_2 to make lower band gap materials. Furthermore, we use nanowires as the synthetic template for these materials because they provide a large semiconductor-liquid interfacial area.

ZnO nanowires can be alloyed with In^{3+}, Fe^{3+} and other trivalent metal ions to form a unique structure with the formula $M_2O_3(ZnO)_n$, also known as MZO. We synthesize indium zinc oxide (IZO) and indium iron zinc oxide (IFZO) nanowires and study their crystal structure using atomic-resolution electron microscopy, among other methods. We elucidate a structural model for MZO that resolves inconsistencies in the existing literature, based on the identification of the zigzag layer as an inversion domain boundary. These nanowires are shown to have a lower band gap than ZnO and produce photocurrent under visible light illumination.

Another solid-state diffusion reaction is also studied by electron microscopy. TiO_2 nanowires are coated with metal oxides by a variety of deposition methods, and then converted to $MTiO_3$ at high temperatures, where M is a divalent transition metal ion, such as Mn^{2+}, Co^{2+}, or Ni^{2+}. When Co_3O_4 particles attached to TiO_2 nanowires are annealed for a short time, we observe the formation of a

$CoO(111)/TiO_2$ (010) interface. If the nanowires are instead coated with $Co(NO_3)_2$ salt and then annealed briefly, then isolated pockets of $MTiO_3$ are formed on the nanowire surface. This structure retains the conductive channel in the center of the nanowire, which would be useful for charge separation. Longer annealing times result in segmented nanowires; the segments formed from a Ni-coated nanowire are bounded by $TiO_2(01\bar{1})$ twin planes and $NiTiO_3\{100\}/TiO_2\{03\bar{1}\}$ interfaces.

Electrochemical energy storage is another approach for making solar energy competitive with fossil fuels that can be burned on-demand. One device used for energy storage is an electric double layer capacitor (EDLC). Graphene-based aerogels are porous materials composed of few-layer graphitic sheets, and they have the potential for higher surface area and higher conductivity than standard carbon aerogels, making them good EDLC electrode materials.

Graphene oxide (GO) is the precursor material for the synthesis of a graphene-based aerogel, and it has been widely studied. Yet the hydrothermal gelation is not fully understood, due to the high pressure reaction conditions and the non-uniform nature of GO. We demonstrate a number of changes that occur to the GO sheets during gelation: wrinkling, formation of a densified monolith, deoxygenation, increasing thermal stability, and color change. Plotting the time evolution of all these properties shows that they are simultaneous and likely of common origin. Possible mechanisms for gelation are explored.

Graphene-based aerogels are synthesized by vapor phase thermal reduction of GO aerogels at high temperatures. Further deoxygenation is observed in the aerogel after thermal reduction, along with greater crystallinity and an associated change in the electronic structure. If graphene-based aerogels are then exposed to high-temperature boron oxide vapor, they are converted to boron nitride (BN) aerogels. The structure of the BN is investigated and shown to be largely turbostratic. The BN aerogels are superhydrophilic and thermally stable, allowing them to adsorb oil and then be regenerated by burning in air.

Acknowledgements

I owe a great deal of thanks to many people for making this dissertation possible:

To Anthony and Chenghao, my fellow members of the Ju crew.

To every member of the Yang and Zettl groups who helped me during this period of personal and professional growth.

To Peidong and Alex for giving me the opportunity to work and learn in this outstanding research institution.

To Lauren for our many productive life troubleshooting sessions.

To Kyle for deciding to come to that Chem Keg 5 years ago, and for supporting me completely every day since then.

To Mom, Seth, and Lee for your encouragement throughout my west coast adventure.

To Bill, Ellen, and the entire extended Broaders family for making me feel loved and cared for in my adopted home state.

To my grandfather, Irving, for teaching me to love chemistry.

And to Isaac for coming along at just the right time and putting everything in perspective.

Table of Contents

Chapter 1

Introduction to Metal Oxide Nanowires for Photoelectrochemical Energy Conversion

1.1 Water splitting basics

The need for an abundant, clean and renewable source of energy has been recognized for many years. Indeed, the search for low-carbon and carbon-free energy sources is becoming more urgent with time, as climate scientists find more and more irrefutable evidence of anthropogenic climate change.[1] Of all the alternatives to fossil fuels, solar energy is the only one that has the capacity to provide for 100% of humanity's energy needs, including future projected increases in energy use.[2] A simple calculation demonstrates just how much sunlight is available on Earth. Total global energy use in 2011 was 520 quadrillion Btu,[3] which translates to a power consumption of 17.4 TW. Meanwhile, the solar flux that reaches the earth's surface through the atmosphere is 1.00 kW/m^2.[4] If we take the projected circular area of sunlight based on the radius of the earth (6.37×10^6 m), our planet receives an average of 127,000 TW of solar energy. This is enough power to provide all human energy needs for one year in *less than two hours*.

Solar radiation is an immense energy reservoir—one that could theoretically provide all of the energy that society requires, even as the global population and energy use per capita are both increasing steadily. If only a small portion of energy from the sun were captured, it could easily replace fossil fuels and prevent energy-related carbon emissions into the atmosphere. However, a major barrier to implementation of solar energy harvesting is the lack of cheap and convenient methods of storing it. Photovoltaics can provide electricity from sunlight during the day, but in order to eliminate the need for fossil fuels and usher in a future free of greenhouse gas emissions, we need the ability to store and transport energy after its conversion from sunlight.

1.1.1 The water splitting reaction

One way to store solar energy is in the form of chemical products, as plants do in photosynthesis. The quest to create high energy bonds and store the resulting chemicals as fuel is called artificial photosynthesis, and it has been referred to as the holy grail of chemistry.[5] Many efforts in this direction focus on the production of hydrogen gas from water, also known as water splitting. Hydrogen is a high energy density fuel in its liquid form, and it can be used very efficiently for electricity generation from fuel cells, with only liquid water as a byproduct.[6] However, hydrogen is currently produced from steam reforming of natural gas, in a process that releases carbon

dioxide into the atmosphere. The only products of water splitting, on the other hand, are hydrogen and oxygen gas. No water splitting material is efficient enough for mass production of hydrogen at present, but the materials challenge has been tackled with increased vigor in recent years, thanks to advances in nanoscale materials synthesis.[7]

The electrochemical half-reactions for water splitting and the overall chemical reaction are shown in Scheme 1.1 below.

$H_2O \rightarrow 2\ H^+ + 2e^- + ½\ O_2$ $\quad$ $E°(O_2/H_2O) = 1.23$ V vs. SHE

$2\ H^+ + 2\ e^- \rightarrow H_2$ $\quad$ $E°(H^+/H_2) = 0$ V vs. SHE

$H_2O\ (l) \rightarrow H_2\ (g) + ½\ O_2\ (g)$ $\quad$ $\Delta E° = 1.23$ V

Scheme 1.1. The water splitting reaction and its two component half-reactions: the oxygen evolution reaction (OER) and the hydrogen evolution reaction (HER). Reaction potentials listed are for pH = 0, based on the definition of a standard hydrogen electrode (SHE).

It should be noted that hydrogen can be produced from sunlight if a solar cell is used to supply external bias of at least 1.23 V to overcome the thermodynamic barrier of electrolysis. Indeed, hydrogen can be produced from sunlight via an even more circuitous route through the reforming of biomass, which was grown originally by harnessing solar energy. However, if one aims to produce industrial quantities of hydrogen, the simplest technology is the most attractive. For this reason, we choose to investigate the production of hydrogen directly from a photocatalyst suspended in water, with neither wires nor organisms as intermediaries for energy conversion.

1.1.2 Energy requirements for water splitting

A semiconductor or other chromophore that absorbs photons of energy greater than 1.23 eV is needed to drive water splitting directly, through the creation of electron-hole pairs to be consumed in the two half-reactions. Unfortunately, both hydrogen evolution and oxygen evolution may require a significant overpotential, depending on the kinetic properties of the semiconductor surface. Therefore, the band gap required for a single semiconductor to be able to accomplish water splitting is typically at least 2 eV.[8] The solar spectrum has a large photon flux in the visible region that would be wasted using a higher band gap material.[4]

To limit the overpotential and maximize efficient use of sunlight, the system should also be designed with catalytic properties in mind, either of the semiconductor itself or a co-catalyst coated on the surface of the water splitting material. There are many well-studied electrocatalytic materials,[8] such as RuO_2 for oxygen evolution and Pt for hydrogen evolution, as well as some intriguing newer materials based on transition metal complexes.[9,10] It is important to optimize the density of co-catalyst coverage, in order to prevent excessive light absorption by the co-catalyst rather than the electrode itself.

In addition to having a band gap large enough to drive the water splitting reaction, a semiconductor must have a conduction band with higher energy than the hydrogen reduction

potential, and the valence band must be lower energy than the water oxidation potential. When band edges have been determined by non-electrochemical methods, they may be stated as energy values rather than potentials. The values of energy and potential carry opposite sign, and they can be interconverted using the relation $\Delta G = -n \cdot F \cdot E$, where n is the number of electrons transferred and F is the Faraday constant. Band energies of some materials will change with pH, because the potential distribution at the surface can depend on the concentration of surface adsorbates, i.e. H^+ and OH^-.[11,12] Furthermore, the standard electrochemical potentials for the HER and OER also shift with pH based on the Nernst equation: $E = E^o - 0.059 \cdot pH$. For this reason, it is advisable to measure band energies (using methods described in Section 1.2) at the particular pH of interest and compare with the OER/HER potentials at that pH.

The alignment of band energies with the reaction potentials for several common semiconductors is illustrated graphically in Figure 1.1. There are few materials that can fulfill all of the requirements for water splitting; these tend to be complex compounds, with mixtures of anions such as oxynitrides used to achieve the ideal band placement.[13]

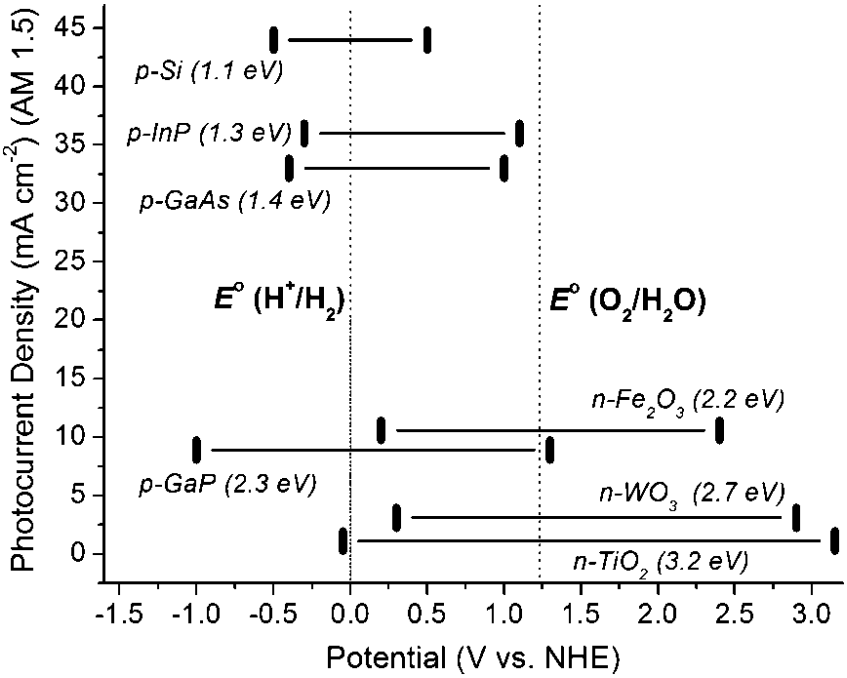

Figure 1.1. Band gaps (in parentheses), conduction band (left bar) and valence band (right bar) energies are plotted vs. the maximum possible photocurrent under solar illumination for several common semiconductors. The HER and OER potentials shown at the dotted lines are for pH = 0. Reproduced from Walter et al.[8]

Once an electron-hole pair has been created, there must be an electronic driving force for the charges to migrate to the semiconductor surface and react with adsorbed species in the OER/HER. This driving force comes from the phenomenon of band-bending.[11] When the semiconductor equilibrates with the Nernst potential of the redox couple in solution, the majority

carrier is depleted at the surface and the bands "bend" toward the solution potential. This encourages the minority charge carrier to move toward the surface, where it can take part in either oxygen or hydrogen evolution. For example, if an n-type semiconductor is immersed in a liquid with a solution potential that is lower in energy than the semiconductor's Fermi level, then equilibrium is achieved when electrons from the conduction band cross the interface into solution. Then, when light is absorbed, any holes created in the positively-charged depletion region will drift toward the surface and take part in the OER. This scenario is depicted in Figure 1.2.

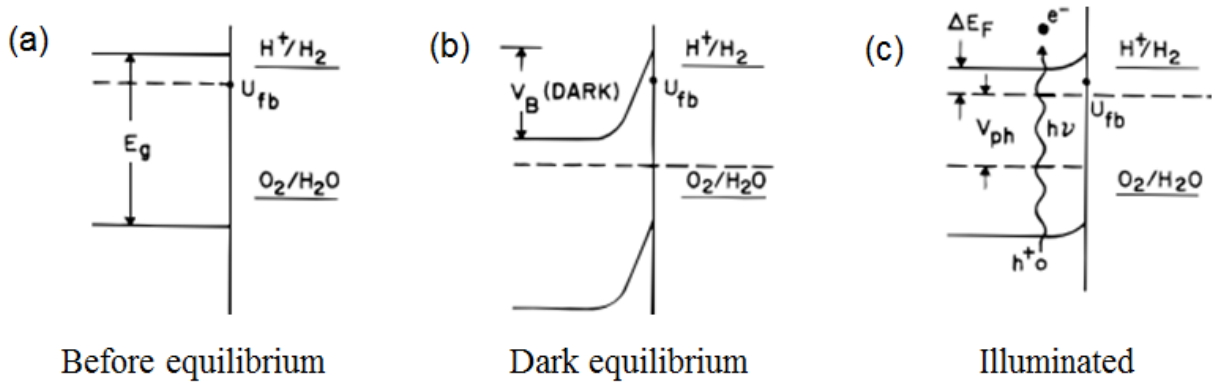

Figure 1.2. Relative energy levels of an n-type semiconductor (left) and the redox couples for water splitting (right) under different conditions. Band bending in (b) is due to electron depletion at the surface. Under illumination in (c), the electron-hole pairs generated in the depletion region are separated, and the holes migrate to the surface to take part in water oxidation. The dashed line represents the average electron energy, i.e. Fermi level, of the entire system. Adapted from Nozik and Memming.[11]

If, on the other hand, the Nernst potential of the redox couple is *higher* in energy than the Fermi level of the n-type semiconductor, the bands will bend in the opposite direction and electrons will accumulate rather than being depleted at the surface. This will prohibit rapid charge transfer of holes and render the material unable to perform as an anode. Moreover, it is not the vacuum potential of the Fermi level that is important in determining solution phase reactivity, but rather the average electronic potential of the ZnO surface when exposed to water. This value is known as the flat band potential, because it is the potential that would be measured in the semiconductor when the bands are flat, i.e. before electronic states across the interface have equilibrated, as in Figure 1.2a. Because band bending is so critical to electron transport at a surface, it is important to determine both the carrier type and the flat band potential of a semiconductor in order to predict its performance in a water splitting scheme. Methods for determining these values experimentally are described in Section 1.2.

An n-type semiconductor is likely to have appropriate band bending for the OER, as shown in Figure 1.2b and 1.2c. However, this means that the material's ability to perform HER at the same surface is limited. If a single material is intended to perform complete water splitting, then there will be a trade-off in terms of optimizing the electronic properties for both electron and hole reactivity at the surface. Additionally, it is challenging to synthesize a semiconductor which has

band energies straddling the HER and OER potentials, while also having a band gap small enough to absorb visible light. For these reasons, many researchers have chosen instead to use a so-called Z-scheme, in analogy with biological photosynthesis. A Z-scheme uses dual light absorbers, so that the anode and cathode can be optimized separately to perform their separate reactions. When the two materials are allowed to have different band gaps and different band energies, the maximum possible efficiency of the system increases.[14] The Z-scheme reaction system is depicted in Figure 1.3. Electrons are collected on the surface of the cathode, and holes are collected on the surface of the anode. The electron from the anode and the hole from the cathode eventually recombine, either at the interface between the two materials or via an electrochemical mediator.

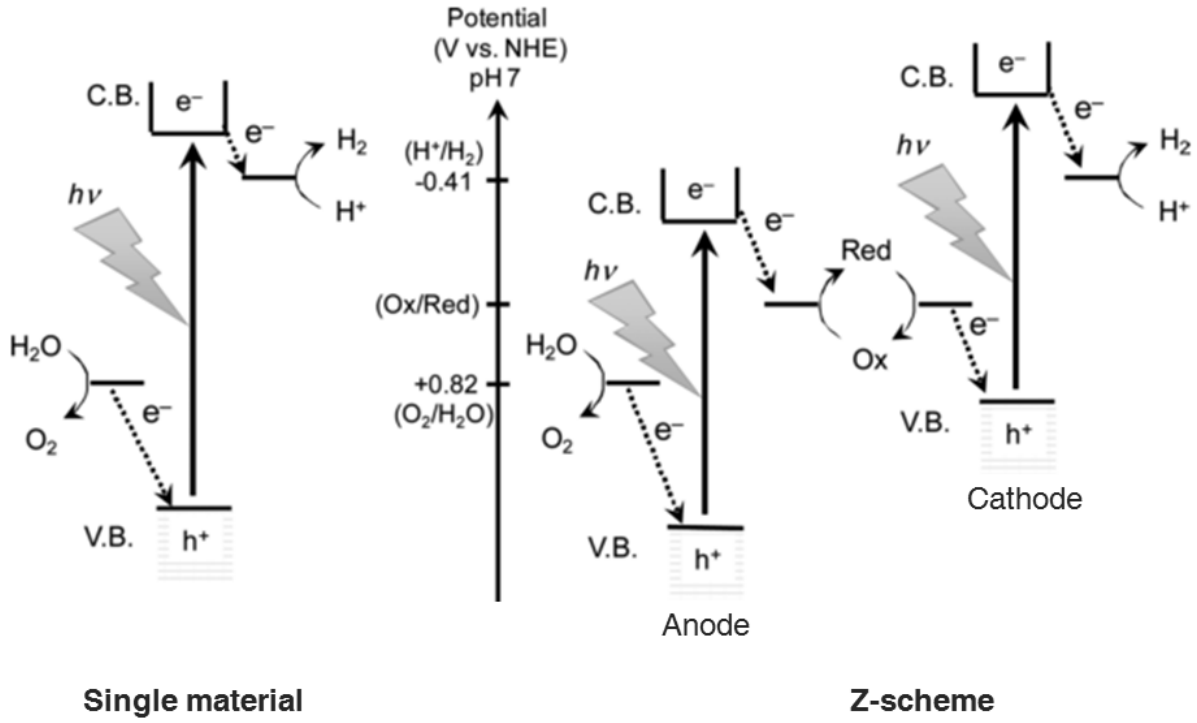

Figure 1.3. Water splitting depicted with either a single light absorber (left) or a Z-scheme with two tandem light absorbers (right). Energy efficiency is reduced in the Z-scheme configuration, due to the offset between the conduction band of the anode and the valence band of the cathode, where extra energy is lost as heat during recombination. Adapted from Maeda et al.[15]

1.1.3 Key properties of a photoelectrochemical anode

As discussed above, there are several requirements that must be satisfied for a material system to function effectively at water splitting. Our work here pertains specifically to anodes for water splitting, so the focus will be on the following qualities that must be optimized in anodic performance:

1. Band gap absorbs a large portion of the solar spectrum
2. Valence band energy is lower than OER potential

3. Conduction band energy is higher than the valence band of the cathode
4. Electrons are the majority charge carrier
5. Surface is catalytic for hole reactivity
6. Stable in water and light for long periods of time

Any of these characteristics that are lacking in a particular material will inhibit its performance as a water splitting anode.

1.2 Evaluating performance of a photoelectrochemical system

The efficacy of a water splitting system can be tested by construction of a photoelectrochemical (PEC) device. An anode and cathode are electrically connected to each other and immersed in aqueous solution, so that they can function as the working and counter electrode (or vice versa) in an electrochemical cell. The cell is exposed to light that is passed through either a monochromator or a spectral filter. For best results, the cell should have a flat window of quartz or other UV-transparent material, and the intensity of light should be measured by a photodiode at the position of the cell.

Electron flow from the anode to the cathode is measured by a potentiostat before and after illumination, and the difference between these values is recorded as the photocurrent. Much can be learned by plotting the photocurrent as a function of experimental conditions, such as wavelength, applied voltage, surface preparation, and immersion time. In the case of a single-material water splitting system, the working device would simply be the material immersed in water; however, in order to do electrochemical performance testing, one must use two identical electrodes of the water splitting material. For a Z-scheme, the anode and cathode materials can be tested together to simulate the working device, or they can be tested separately versus a standard counter electrode and compared to other anodes and cathodes. Platinum wire or mesh is a popular choice for counter electrode, because its surface is catalytic but otherwise chemically inert. Some measurements require a reference electrode as a standard for potential; a common choice is the Ag/AgCl electrode in saturated KCl solution, which has a potential of E^o = +0.197 V vs. SHE.

1.2.1 Band gap and flat band potential

The electronic properties of the electrode materials that are relevant to water splitting, such as the band gap (E_g) and the flat band potential (V_{fb}), can be characterized in a PEC cell. Materials exhibit an increase in absorption coefficient roughly in the vicinity of their E_g. Equation 1.1 gives the relationship between absorption coefficient (α) and E_g.[16]

Equation 1.1

$$(\alpha \cdot h\nu)^n \propto h\nu - E_g$$

If photocurrent (I) increases proportionally as more photons are absorbed, then I and α should rise concurrently. To obtain an accurate value of E_g from PEC testing, measure the photocurrent with respect to incident frequency, and then scale those data points by the measured intensity of light at each frequency. Plot $(I \cdot h\nu)^n$ vs. $h\nu$, where n = 2 for direct transitions and n = ½ for

indirect transitions. Then simply extrapolate from a linear region of the data to determine the x-intercept; that value is E_g.

There are three methods for measuring a material's V_{fb} in a PEC cell.[17,18] In the first method, linear voltammetry is conducted in the cell and the onset of photocurrent is measured. When the potential in the electrode equals V_{fb}, then the bands are flat and no charge separation occurs. In the case of an n-type material, a decrease in the electrode energy (i.e. more positive potential) will cause more band bending and greater photocurrent. Specifically, the relationship in Equation 1.2 has been derived for photocurrent in a semiconductor-electrolyte interface.[16] Therefore, in order to obtain a value for V_{fb}, plot applied voltage (V) vs. I^2 and extrapolate to the x-intercept.

Equation 1.2

$$I^2 \propto V - V_{fb}$$

Alternatively, the open circuit potential can be measured under intense illumination. In this method, the potentiostat prevents the flow of current while the electrodes are illuminated, so charges that are generated in the depletion region are forced to accumulate at the surface, thus counteracting the effect of band bending at equilibrium. As illumination increases, open circuit voltage (V_{oc}) shifts more negative for n-type electrodes and more positive for p-type electrodes. If photon flux is high enough that the bands completely flatten, then the measured value of V_{oc} is equal to the E_{fb}. For some materials, it may be difficult to generate sufficient light to saturate the depletion region.

A third method for flat band determination is to conduct Mott-Schottky measurements using electrochemical impedance spectroscopy (EIS).[19,20] This method takes advantage of the capacitive behavior of the depletion region, also known as the space charge region. The capacitance of the semiconductor surface depends on the amount of charge stored in the depletion region, which in turn depends on both the carrier concentration in the semiconductor and the potential difference across the semiconductor-electrolyte interface. This is expressed mathematically in Equation 1.3. V_{fb} can be roughly determined by extrapolating to the x-intercept of C^{-2} vs. V; at room temperature, the term kT/e is less than 10 mV and introduces an insignificant amount of error.

Equation 1.3

$$\frac{1}{C^2} \propto \frac{2}{\epsilon_r \epsilon_o e N_D}\left(V - V_{fb} - \frac{kT}{e}\right)$$

In order to calculate capacitance (C) of the semiconductor surface, impedance spectra should be collected at each potential in the range of interest. The potentiostat introduces a small, sinusoidal potential modulation (5-10 mV) around the applied potential at a particular frequency, and then it measures the phase shift of the current output, i.e. how quickly the electrode is able to respond to the modulating signal. A non-capacitive electrode would produce a perfect linear response. The impedance at each frequency is calculated and plotted vs. frequency in a Bode plot; alternatively, the real impedance vs. the imaginary impedance are plotted for each frequency in a Nyquist plot. These plots are fit to a particular model circuit to determine the capacitance and resistance of the circuit elements.

One circuit that is commonly used and relatively simple is the Randles circuit, with one capacitive element representing the semiconductor surface and resistors both in series and in parallel, representing the charge transfer resistance (Faradaic) and the electrolyte resistance (non-Faradaic), respectively. However, in real systems, more complex circuit elements may be required to obtain a reasonable fit of the impedance spectra. Automated EIS software routines should be avoided until the circuit model for a particular PEC cell has been experimentally confirmed.

While there are a variety of methods for measuring V_{fb}, the more important metric for evaluating the ability of a material to oxidize water is the comparison of its band energies to the OER and HER potentials. In order to calculate the conduction band and valence band levels, E_{cb} and E_{vb}, we must know N_D, the donor density or carrier concentration.[21] If the material of interest is nanostructured, then the accurate determination of N_D is not possible by standard bulk methods. However, the Mott-Schottky method can be used to determine carrier concentration (N_D) of a material based on the slope of the C^{-2} vs. V plot. Equation 1.3 assumes a flat surface, and therefore a planar depletion region, but the same concepts can be applied to nanowires, which have a cylindrical junction with the electrolyte. Mora-Seró et al. developed a model for radial capacitance in nanowire arrays which allows the calculation of carrier density from electrochemical measurements.[22]

1.2.2 Efficiency measurements

When a system of interest (either a single material or a Z-scheme) has been assembled into an electrochemical cell, then its efficiency of converting solar energy to hydrogen fuel can be quantified and compared to that of other systems. The standards for this comparison have been reviewed by Chen et al.[18] The most important metric for benchmarking the performance of a PEC system is the solar-to-hydrogen efficiency (STH), which is the overall efficiency of the entire water splitting process. STH is a ratio of chemical energy output to photon energy input (Equation 1.4). For a Z-scheme, stored energy is a product of the photocurrent (j_{ph}) and the thermodynamic potential of the water splitting reaction, 1.23 V. In order to calculate a true efficiency, measurements should be taken at zero bias in a 2-electrode cell, rather than a 3-electrode cell where the working electrode and the counter electrode are held at separate voltages.

Equation 1.4

$$\mathrm{STH} = \frac{j_{ph}(mA/cm^2)\cdot 1.23(V)}{P_{total}(mW/cm^2)}$$

Calculating STH requires an accurate spectral simulation of sunlight, such as the AM 1.5 spectrum recorded by the American Society of Testing and Materials,[4] and it assumes a linear relationship between light intensity and hydrogen production. If the evolved hydrogen gas is measured by gas chromatography, in the absence of any sacrificial reagents, then the numerator in Equation 1.4 can be calculated instead by multiplying the rate of gas production by the chemical energy stored in an H-H bond (ΔG = 237 kJ/mol).

Another key number used to compare PEC performance is the incident photon-to-current efficiency (IPCE), also known as external quantum efficiency (EQE).[18] IPCE refers to the combined efficiency of 3 processes—electron-hole pair formation, charge separation, charge transport—at a particular wavelength (Equation 1.5). The relationship between IPCE and STH is simply that IPCE is measured using monochromated light and is reported at a single wavelength rather than using a broadband light source. A system with high IPCE in a particular spectral region may have very poor STH if that region does not overlap considerably with the solar spectrum.

Equation 1.5

$$\text{IPCE} = \frac{j_{ph}(mA/cm^2)\cdot 1240(V\cdot nm)}{P_{total}(mW/cm^2)\cdot \lambda(nm)}$$

1.3 Metal oxide nanowires as water splitting anodes

One-dimensional nanostructures have been a burgeoning area of research since the late 1990's, thanks to their unique applications in many areas of science and engineering.[23] The nanowire geometry is particularly exciting for researchers with an interest in solar water splitting. Hydrogen evolution is a heterogeneous reaction, so a high surface area material is necessary in order to maximize opportunities for reaction with the solution phase. Nanowires have a great advantage in surface area over bulk materials. For example, nanowires that are 50 nm wide and 1 μm long deposited in a vertical array with 1 x 10^{10} nanowires per cm^2 adds nearly 16 times more reactive surface area than a flat surface with the same geometric surface area.

Another advantage of nanowires for solar energy harvesting is that the charge separation can occur radially across the depletion region, while the majority carrier can be shuttled away through the undepleted, conductive center channel of the nanowire.[24–26] In this configuration, the nanowire is not acting purely as a one-dimensional material, since the radial dimension is important for efficient charge separation. The optimal design is a nanowire with a radius approximately equal to the minority carrier diffusion length, and with a carrier concentration such that the depletion region does not penetrate the core of the wire.[27]

Metal oxides are a popular choice for a water splitting anode, for several reasons. Oxide semiconductors are typically n-type materials, which is beneficial for obtaining the appropriate band bending for anodes in solution. They are highly tunable materials, with many crystal structures and mixtures of cations available to form oxides with slightly different properties. A large number of the photocatalytic materials that have been studied to date happen to share similar electron configurations, with respect to their d orbitals. Many of them have d^0 metal cations, such as Zn^{2+}, Ga^{3+}, or In^{3+}; others are d^{10}, such as Ti^{4+} or W^{6+}.[28,29] The d orbitals being either completely empty or completely full contributes to an ideal band structure for water splitting. In the d^0 and d^{10} oxides, valence bands are primarily composed of oxygen 2p orbitals, which have an appropriate energy level for water oxidation.

Additionally, metal oxides can often be derived cheaply from abundant minerals, and they are generally stable in air. One downside for some oxide materials is the possibility of dissolution in

aqueous media. In a typical dissolution reaction, holes generated in the valence band are captured at the surface.[30] Rather than oxidizing aqueous species as intended in the OER, the holes are used to oxidize the semiconductor directly, evolving oxygen gas and solvated metal cations. The potential of this redox couple, i.e. $E^o(M^{2x+}/MO_x)$, relative to the energy of the conduction band determines the likelihood of dissolution. More negative potentials result in less stable oxides. The dissolution is pH-independent, so as E_{FB} and $E^o(O_2/H_2O)$ both shift to more negative potentials with increasing pH, the semiconductor will typically become more stable.

1.3.1 Zinc oxide nanowires

Zinc oxide (ZnO) is a wide band gap semiconductor which has been a subject of frequent study for many years, due to its useful optical properties.[31] It has a direct band gap of 3.37 eV, therefore it is only able to absorb UV or near-UV photons of wavelengths less than 368 nm. For this reason, ZnO is not a good candidate for an all-in-one PEC strategy for water splitting, because its band gap is much too high for efficient capture of the solar spectrum. In the following chapters, we investigate a modified crystal structure for ZnO that would be more suitable as a water splitting material. This requires tailoring the band energies such that the band gap is reduced.

In order to devise a strategy for band gap engineering, we must consider where the conduction band minimum and valence band maximum of ZnO fall relative to the HER and OER, respectively, which can be calculated from the flat band potential as discussed above in Section 1.2. The flat band potential of ZnO has been determined by Mott-Schottky measurements to be V_{fb} = -0.10 V at pH = 4.8.[19] For simplicity, all potentials cited will be vs. standard hydrogen electrode (SHE) unless otherwise noted. The flat band value for ZnO is pH dependent; the flat band energy increases to V_{fb} = -0.30 V at pH = 9.2, which is a shift of ~45 mV per unit of pH. As discussed above, the HER and OER undergo a negative shift 59 mV for each unit of pH.

Using an approximate value of for carrier concentration ($N_D = 10^{17}$ cm^{-3}), the conduction band edge (E_C, stated here as a potential) is calculated to be -0.20 V at pH = 4.8. Subtracting the band gap from E_C yields a value for the valence band edge of E_V = +3.17 V. For comparison, $E^o(O_2/H_2O)$ = +0.95 V at pH = 4.8, therefore the valence band of ZnO is well below the OER potential. In fact, there is an energy difference of 2.22 eV that drives water oxidation from the ZnO valence band. However, at pH = 4.8, the potential for the HER is -0.28 V, so the E_C value of ZnO is not positioned favorably to produce hydrogen. The difference between the energy levels is only 0.08 eV, but it is likely that ZnO would require the help of a separate cathode material in a Z-scheme configuration in order to complete the water splitting reaction.

Based on the above measured band positions, we have some guidance in how to best modify the ZnO structure in order to reduce the band gap and achieve a more effective water splitting anode. Alloying ZnO with Cd ($Cd_yZn_{(1-y)}O$) has been shown to narrow the band gap to be less than 3.0 eV.[31] Others have shown that doping ZnO nanowires with nitrogen can produce hydrogen production under visible illumination, due to a lower energy onset of visible light absorption.[32] In Chapter 2, we investigate a class of materials where zinc oxide nanowires are alloyed with indium and iron. This substitution of Zn^{2+} with other d^0 ions (In^{3+} and/or Fe^{3+}) produces a binary or ternary oxide which absorbs visible light.

1.3.2 Titanium dioxide nanowires

Titanium dioxide (TiO_2) is another wide band gap semiconductor that has been used for decades in PEC studies.[33] As early as 1972, Fujishima and Honda had demonstrated that TiO_2 could be used to generate photocurrent in a PEC cell with a platinum counter electrode.[34] Like ZnO, TiO_2 is not able to independently split water because its conduction band level is not high enough in energy. Instead, it has been commonly studied as an anode in water splitting Z-schemes as well as dye-sensitized solar cells.[8]

TiO_2 is most commonly found in the anatase and rutile crystal structures. The rutile form has a band gap of 3.0 eV, and can be modified to form different crystal structures with mixed metal cations that have smaller band gaps, making them good visible light absorbers. These compounds have the formula $MTiO_3$, where M^{2+} can be one of many different metal cations. When M is a larger Group I or Group II atom, such as Ca or Sr, then $MTiO_3$ tends to be in the perovskite family. On the other hand, if M is a transition metal, such as Ni or Co, then the structure tends to be ilmenite, which is an ordered version of corundum. Conversion of TiO_2 nanowires to ilmenite structures is considered in detail in Chapter 3.

References

(1) IPCC. In *Climate Change 2013: The Physical Science Basis. Contribution of Working Group I to the Fifth Assessment Report of the Intergovernmental Panel on Climate Change*; Stocker, T. F.; Qin, D.; Plattner, G.-K.; Tignor, M.; Allen, S. K.; Boschung, J.; Nauels, A.; Xia, Y.; Bex, V.; Midgley, P. M., Eds.; Cambridge University Press, Cambridge, United Kingdom and New York, NY, USA, 2013.

(2) Lewis, N. S.; Nocera, D. G. *Proc. Natl. Acad. Sci. U. S. A.* **2006**, *103*, 15729–15735.

(3) U.S. Energy Information Administration. International Energy Statistics http://www.eia.gov/cfapps/ipdbproject/IEDIndex3.cfm.

(4) American Society for Testing and Materials. Reference Solar Spectral Irradiance: Air Mass 1.5 http://rredc.nrel.gov/solar/spectra/am1.5/.

(5) Bard, A. J.; Fox, M. *Acc. Chem. Res.* **1995**, *28*, 141–145.

(6) Crabtree, G. W.; Dresselhaus, M. S. *MRS Bull.* **2008**, *33*, 421–429.

(7) Liu, C.; Dasgupta, N.; Yang, P. *Chem. Mater.* **2014**, *26*, 415–422.

(8) Walter, M. G.; Warren, E. L.; McKone, J. R.; Boettcher, S. W.; Mi, Q.; Santori, E. a; Lewis, N. S. *Chem. Rev.* **2010**, *110*, 6446–6473.

(9) Kanan, M. W.; Nocera, D. G. *Science* **2008**, *321*, 1072–1075.

(10) Reece, S. Y.; Hamel, J. A.; Sung, K.; Jarvi, T. D.; Esswein, A. J.; Pijpers, J. J. H.; Nocera, D. G. *Science* **2011**, *645*.

(11) Nozik, A. J.; Memming, R. *J. Phys. Chem.* **1996**, *100*, 13061–13078.

(12) Nozik, A. J. *Annu. Rev. Phys. Chem.* **1978**, *29*, 189–222.

(13) Breault, T. M.; Brancho, J. J.; Guo, P.; Bartlett, B. M. *Inorg. Chem.* **2013**, *52*, 9363–9368.

(14) Bolton, J.; Strickler, S.; Connolly, J. *Nature* **1985**, *8*, 495–500.

(15) Maeda, K.; Higashi, M.; Lu, D.; Abe, R.; Domen, K. *J. Am. Chem. Soc.* **2010**, *132*, 5858–5868.

(16) Butler, M. *J. Appl. Phys.* **1977**, *48*, 1914–1920.

(17) Turner, J. A. *J. Chem. Educ.* **1983**, *60*, 327.

(18) Chen, Z.; Jaramillo, T. F.; Deutsch, T. G.; Kleiman-Shwarsctein, A.; Forman, A. J.; Gaillard, N.; Garland, R.; Takanabe, K.; Heske, C.; Sunkara, M.; McFarland, E. W.; Domen, K.; Miller, E. L.; Turner, J. A.; Dinh, H. N. *J. Mater. Res.* **2010**, *25*, 3–16.
(19) Cardon, F.; Gomes, W. *J. Phys. D. Appl. Phys.* **1978**, *11*, L63–L67.
(20) Natarajan, A.; Oskam, G.; Searson, P. C. *J. Phys. Chem. B* **1998**, *102*, 7793–7799.
(21) Sze, S. M.; Ng, K. K. *Physics of Semiconductor Devices*; 3rd ed.; Wiley & Sons: Hoboken, NJ, 2006; pp. 24–25.
(22) Mora-Seró, I.; Fabregat-Santiago, F.; Denier, B.; Bisquert, J.; Tena-Zaera, R.; Elias, J.; Lévy-Clément, C. *Appl. Phys. Lett.* **2006**, *89*, 203117.
(23) Xia, Y.; Yang, P.; Sun, Y.; Wu, Y.; Mayers, B.; Gates, B.; Yin, Y.; Kim, F.; Yan, H. *Adv. Mater.* **2003**, *15*, 353–389.
(24) Garnett, E. C.; Yang, P. *J. Am. Chem. Soc.* **2008**, *130*, 9224–9225.
(25) Boukai, A.; Haney, P.; Katzenmeyer, A.; Gallatin, G. M.; Talin, A. A.; Yang, P. *Chem. Phys. Lett.* **2011**, *501*, 153–158.
(26) Hwang, Y. J.; Boukai, A.; Yang, P.; About, M.; Article, T. *Nano Lett.* **2009**, *9*, 410–415.
(27) Kayes, B. M.; Atwater, H. A.; Lewis, N. S. *J. Appl. Phys.* **2005**, *97*, 114302.
(28) Kudo, A.; Miseki, Y. *Chem. Soc. Rev.* **2009**, *38*, 253–278.
(29) Inoue, Y. *Energy Environ. Sci.* **2009**, *2*, 364.
(30) Bard, A. J.; Wrighton, M. S. *J. Electrochem. Soc.* **1977**, *124*, 1706–1710.
(31) Özgür, U.; Alivov, Y. I.; Liu, C.; Teke, A.; Reshchikov, M. A.; Doğan, S.; Avrutin, V.; Cho, S.-J.; Morkoç, H. *J. Appl. Phys.* **2005**, *98*, 041301.
(32) Yang, X.; Wolcott, A.; Wang, G.; Sobo, A.; Fitzmorris, R. C.; Qian, F.; Zhang, J. Z.; Li, Y. *Nano Lett.* **2009**, *9*, 2331–2336.
(33) Hashimoto, K.; Irie, H.; Fujishima, A. *Jpn. J. Appl. Phys.* **2005**, *44*, 8269–8285.
(34) Fujishima, A.; Honda, K. *Nature* **1972**, *238*, 37–38.

Chapter 2

Determination of the Crystal Structure of Indium Zinc Oxide-Based Nanowires and their Use as a Photoelectrochemical Anode

2.1 The MZO class of materials

Indium zinc oxide (IZO) has a remarkable structure that has generated significant interest in the 25 years since its discovery. Annealing a mixture of the precursor oxide powders (ZnO and In_2O_3) for several days at or above 1100 °C produces a material with thin lines of contrast visible by transmission electron microscopy (TEM).[1] Cannard and Tilley originally observed that these lines were very thin In-rich layers, parallel to the (0002) basal plane and separated by thick regions of ZnO.[1] We refer to these as basal inclusions. The chemical formula of IZO can be stated as $In_2O_3(ZnO)_n$. Basal inclusions are often, but not always, regularly-spaced; the spacing depends on the relative amounts of ZnO to In_2O_3, i.e. the value of n, as well as annealing time and temperature.

Kimizuka *et al*. later showed that similar layers form in indium iron zinc oxide (IFZO); In_2O_3 and Fe_2O_3 can be annealed with ZnO to form $InFeO_3(ZnO)_n$.[2] Further TEM studies of IZO and IFZO revealed a modulated layer of contrast in the slab between the basal layers, known as a zigzag.[3,4] Both types of contrast are visible in Figure 2.1. The known range of materials with this structure is not limited to indium and iron. Isostructural compounds can be formed from certain combinations of ZnO and other trivalent metals, in addition to In and Fe, including Ga, Al, Lu, Sc, Yb, Tm.[5–7] The generic trivalent metal ion that is incorporated into ZnO will be referred to herein as M^{3+}, and the class as a whole is labeled $M_2O_3(ZnO)_n$, or MZO.

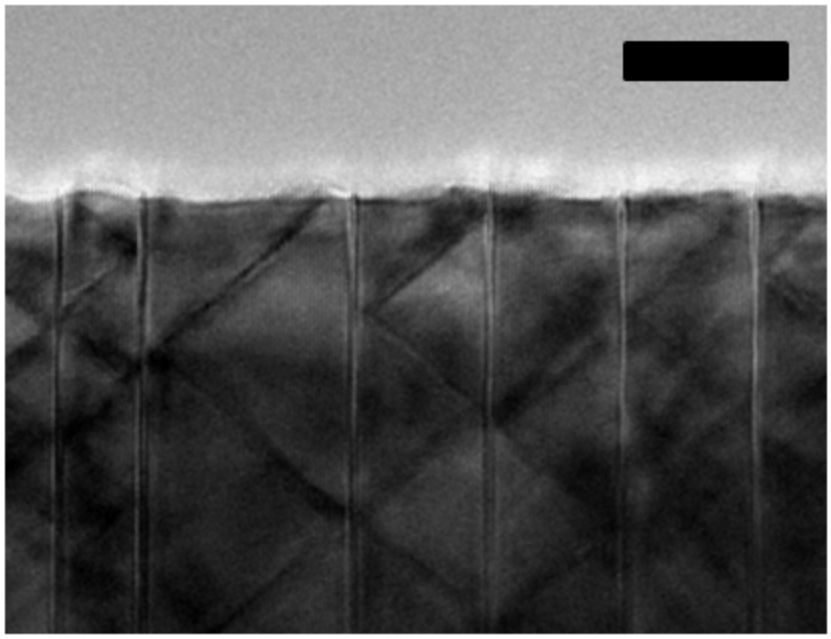

Figure 2.1. TEM image of an IZO nanowire, produced by annealing ZnO nanowires coated with In. The two types of inclusions are shown here: *basal inclusions* that are perpendicular to the surface, and *zigzags* that modulate between the basal inclusions.

IZO has shown significantly enhanced electron conductivity and mobility over zinc oxide, making it useful in touch-sensitive or photo-active devices that require a transparent conducting oxide.[8–10] Research has also shown that IZO has a smaller band gap than either ZnO or In_2O_3, thus making it useful for visible light absorption.[11,12] To increase the utility of IZO and other MZO materials, their structure and formation mechanism must be thoroughly understood.

2.2 A new structural model for $M_2O_3(ZnO)_n$

The structure of MZO materials has been investigated in detail by XRD and TEM. The chemical structure of the basal inclusions has been identified as a single atomic layer of edge-sharing MO_6 octahedra with an overall formula of MO_2^-, separated from the other octahedral layers by n+1 units of ZnO.[2,13] Each oxygen atom in these octahedra is tetrahedrally coordinated by three M^{3+} and one Zn^{2+}; thus, the basal inclusions act as inversion domain boundaries (IDB) by flipping the orientation of the ZnO_4 tetrahedra in the adjacent wurtzite region. This atomic structure of the basal inclusion has been confirmed by aberration-corrected TEM.[14,15]

Given the constraints on the observed structure, there must be a second IDB in the ZnO to restore the orientation of the tetrahedra between two basal inclusions.[14–16] Additionally, because the charge balance of the crystal is disturbed by the MO_2^- composition of the basal layer, there must be extra M^{3+} ion substitutions to balance the overall charge. Further complexity is presented by the balance between the two substituent elements in IFZO and other ternary MZO materials. There are a number of competing structural models that attempt to identify the second IDB, as well as the location of the additional M^{3+}.

Li *et al*. suggested that the center of mass in the wurtzite tetrahedra gradually shifts, yielding a trigonal bipyramidal layer in the center of the slab Figure 2.2a.[17] Here, zigzag contrast is supposedly caused by substitution of M^{3+} for Zn^{2+}, which form $\{1\bar{2}12\}$ planes that are sharply visible along the $<10\bar{1}0>$ zone axis. (In this work, we will use the 4-index notation of wurtzite to describe crystal directions, because these are perpendicular to the crystal planes of the same index. See Figure 2.5 below for more detailed explanation.) Hörlin *et al*. claimed that the zigzag for IFZO is a $\{1\bar{2}14\}$ plane, based on its incident angle with the basal plane by TEM. They also found that the indium resides predominantly in the basal inclusions, while iron is located mainly in the wurtzite slabs.[4]

More recently, drawing on DFT calculations, Yan *et al*.[18] and Da Silva *et al*.[19] suggested that the IZO zigzags are composed of trigonal bipyramidal indium atoms that serve as the second IDB (Figure 2.2b). The indium layer is placed on the $\{10\bar{1}1\}$ plane, where it would be sharply visible along $<11\bar{2}0>$, contrary to experimental reports.[3,4,14–17] Recent calculations using density functional theory (DFT) concluded that the model of Yan *et al*. has a similar formation energy to that of Li *et al*.[20]

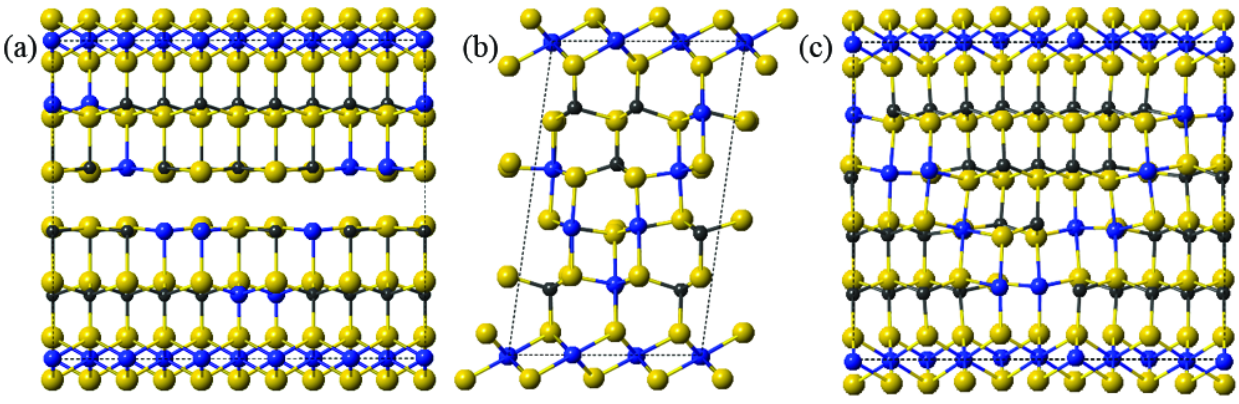

Figure 2.2. Zigzags in the model proposed by Li *et al*. are shown (a) along the $<10\bar{1}0>$ zone axis, with oxygen (yellow), zinc (gray), and indium (blue) atoms. The Yan *et al*. model (b) is viewed along the $<11\bar{2}0>$ zone axis. Our proposed structure (c) is more favorable than any alternative model tested, as described in Section 2.4. Selected oxygen atoms have been hidden for clarity.

None of these structure models for IZO can fully account for prior experimental observations. We have developed a new model for the MZO structure that is supported both by high-resolution electron microscopy and DFT calculations on IZO and IFZO.[21] A defining feature of our model is the inversion of the metal and oxygen positions across a zigzag region, facilitated by 5-coordinate indium or iron atoms. These regions of inversion align themselves along a particular plane, depending on the local metal composition. This model resolves the discrepancies between previous reports, and it suggests that the zigzag plays a key role in the formation mechanism of IZO and IFZO from the native oxides.

2.3 Synthetic methods

Vertical arrays of ZnO nanowires can be grown by a well-established chemical vapor transport (CVT) synthesis, which relies on a vapor-liquid-solid (VLS) mechanism for nanowire formation.[22,23] ZnO nanowires can be grown more cheaply in the solution phase via hydrothermal growth on a seeded substrate.[24] A typical nanowire array is shown in Figure 2.3; this array was grown epitaxially from a thin film of ZnO platelets deposited on an Si wafer from an aqueous solution of $Zn(NO_3)_2$, poly(ethylenimine) (PEI), and hexamethylenetetramine (HMTA) at 90 °C. The resulting nanowires are vertically-oriented and uniform across the array. The area of the array, and therefore the quantity of nanowires synthesized by this method, can be quite large—easily tens of square centimeters using standard size lab equipment. This area is much larger than a ZnO array grown by, where the growth area is typically limited to only a few square millimeters.

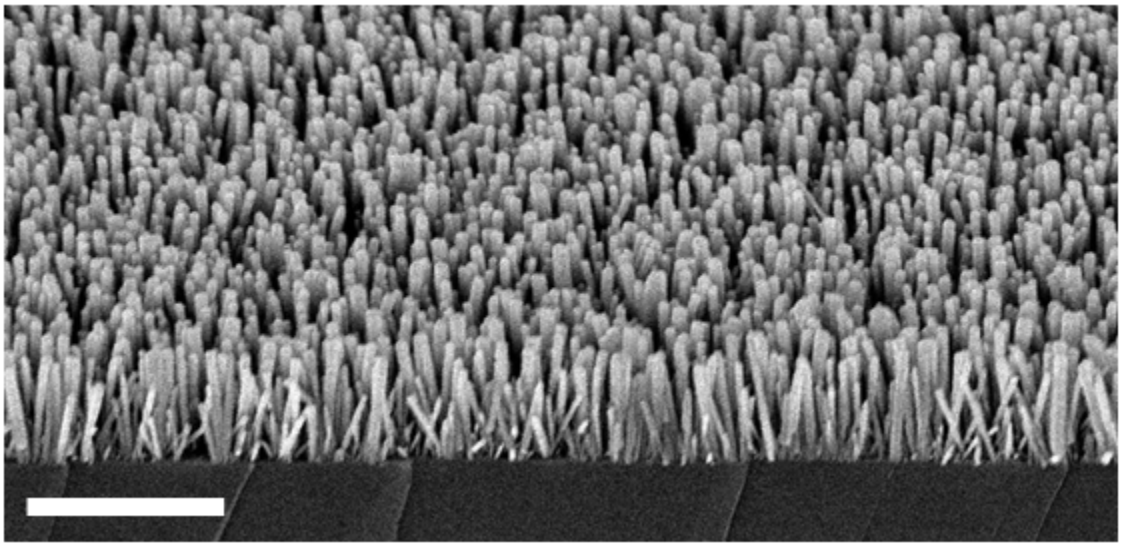

Figure 2.3. A hydrothermally grown ZnO nanowire array, imaged by SEM at a 45° cross-section. Scale bar is 1 μm.

ZnO arrays were converted to IFZO or indium gallium zinc oxide (IGZO) using a method previously reported by this group.[25] Briefly, a ZnO nanowire array was coated with indium and either iron or gallium by physical deposition methods, including thermal evaporation and sputtering. No significant difference was observed between samples made by different techniques of metal deposition. Both metal coatings were approximately 10 nm thick as measured by quartz crystal monitor. The array was then exposed to oxygen plasma and annealed for 30 minutes at 900 °C in an oxygen atmosphere. After conversion, a high density of inclusions can be seen in low-resolution TEM, resulting from incorporation of both In and Fe from the nanowire surface. Segments along the length of an IFZO nanowire are expected to vary slightly in their ratio of indium to iron. Both sputtering and thermal evaporation deposit metal more heavily at the top of the array, so that segments at the nanowire tips have a higher concentration of inclusions than the segments close to the substrate. Additionally, the total amount of coated

metal relative to the amount of ZnO, and therefore the final concentration of M^{3+} in the converted nanowire, varies between samples. The amount of metal deposited was measured during deposition in terms of its planar thickness, but the concentration of M^{3+} depends instead on the conformal thickness, which in turn depends on both the height and density of the nanowire array. Neither the height nor the density of the nanowire array was precisely controlled in this work.

Another parameter that can vary somewhat between nanowire segments is the relative proportion of the two coating metals for ternary compounds. The molar volume of Fe is approximately 2.2 times that of In, therefore a ratio of 2.2:1 of In:Fe coating thickness is required in order to achieve an average atomic ratio of 1:1 across the sample. The corresponding In:Ga ratio is 1.3:1. The IFZO synthesis in particular was found to be less uniform if an excess of Fe was deposited; results shown in this work are from samples with roughly a 1:1 atomic ratio. See the discussion by Moore for greater detail on the variation of coating thickness and metal ratios for a variety of MZO nanowires.[26]

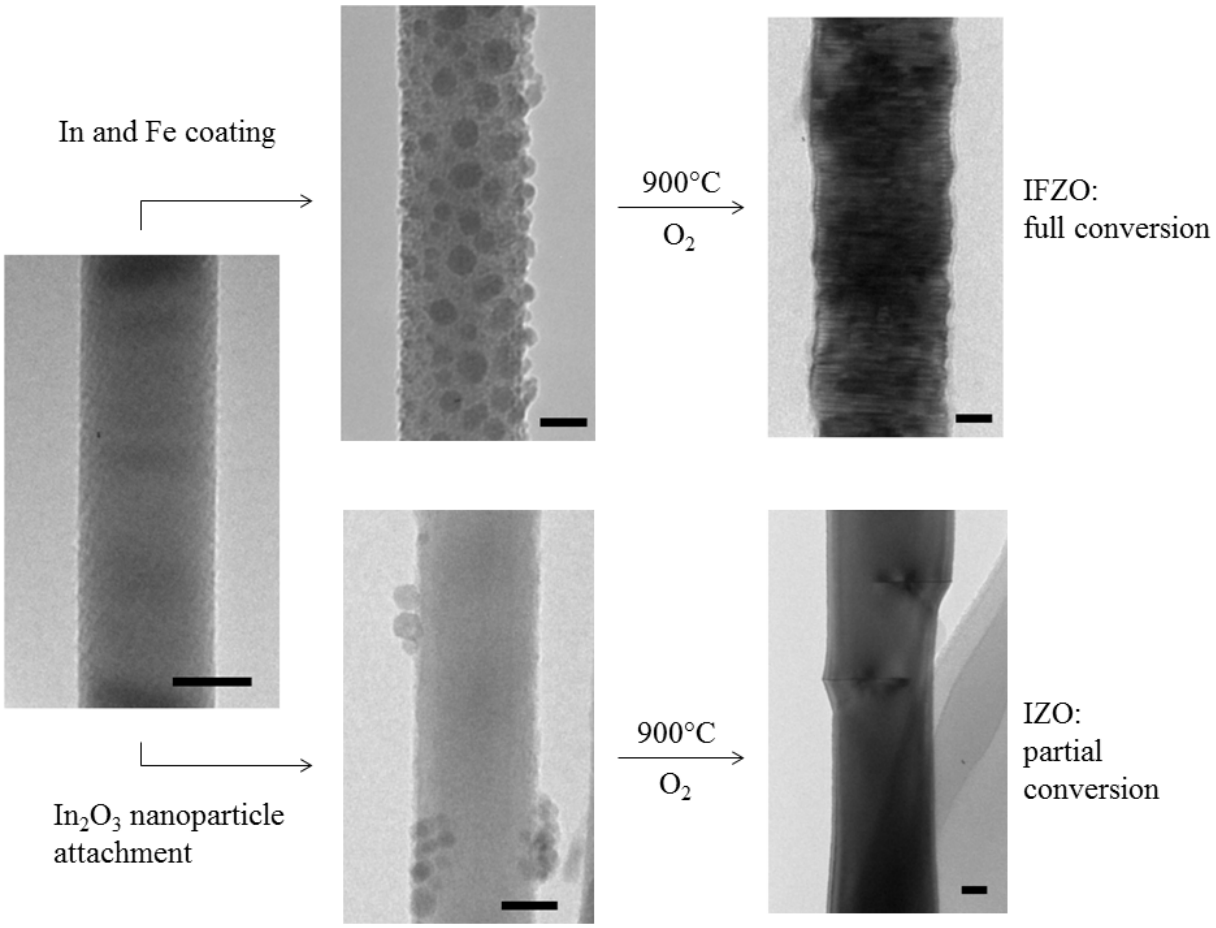

Figure 2.4. Two synthetic methods used to incorporate In and/or Fe into ZnO nanowires are shown, beginning from a VLS-grown ZnO nanowire on the left. Scale bars are 20 nm. The nanowires depicted here by low-resolution TEM are representative of other nanowires from similar samples. For the top path to full IFZO conversion, the sample shown was sputtered with

10 nm of Fe and then thermally evaporated with 10 nm of In, followed by brief exposure to oxygen plasma before annealing. For the bottom path to partially converted IZO, the ZnO array was soaked for two hours in a dilute hexanes solution of In_2O_3 nanoparticles.

In order to observe the mechanism of metal diffusion in detail, sparse metal coatings were desired. Indium oxide nanoparticles were synthesized from $In(acac)_3$ in oleylamine, following the procedure of Seo *et al*.,[27] and attached to the ZnO nanowire surface by soaking the array in a dilute solution of particles dispersed in hexanes. The distribution of these particles was less homogeneous and lower density than the evaporated and/or sputtered samples, so the In atoms could diffuse from an isolated point on the nanowire surface. The array was partially converted to IZO at the points of nanoparticle attachment by annealing in oxygen for 30 minutes at 900 °C. A schematic of both synthetic routes used in this work is shown in Figure 2.4.

2.4 Atomic structure of IZO and IFZO nanowires

Arrays of IZO and IFZO nanowires were dispersed on holey carbon support films for electron microscopy. High resolution, aberration-corrected TEM was done on the TEAM 0.5 microscope at the National Center for Electron Microscopy (NCEM) at Lawrence Berkeley National Laboratory. High angle annular dark field (HAADF) scanning transmission electron microscopy (STEM) images and electron energy loss (EELS) data were collected at 300 kV.

The nanowire growth direction is the c-axis of wurtzite; therefore, nanowires dispersed on TEM grids were all close to either the $<11\bar{2}0>$ or the $<10\bar{1}0>$ zone axis, the latter of which is distinguishable by its rectangular pattern of metal atoms. For a quick guide in labeling the 4-index Miller notation for hexagonal lattice directions, refer to Figure 2.5. There is a common misconception that the third index, labeled *i* in [*hkil*], can be always ignored to convert between 4-index and 3-index notation. Although the third index is redundant when describing planes, where $i = -(h + k)$ in (*hkil*), it is evident from the labels in Figure 2.5 that the same is not true for lattice directions.

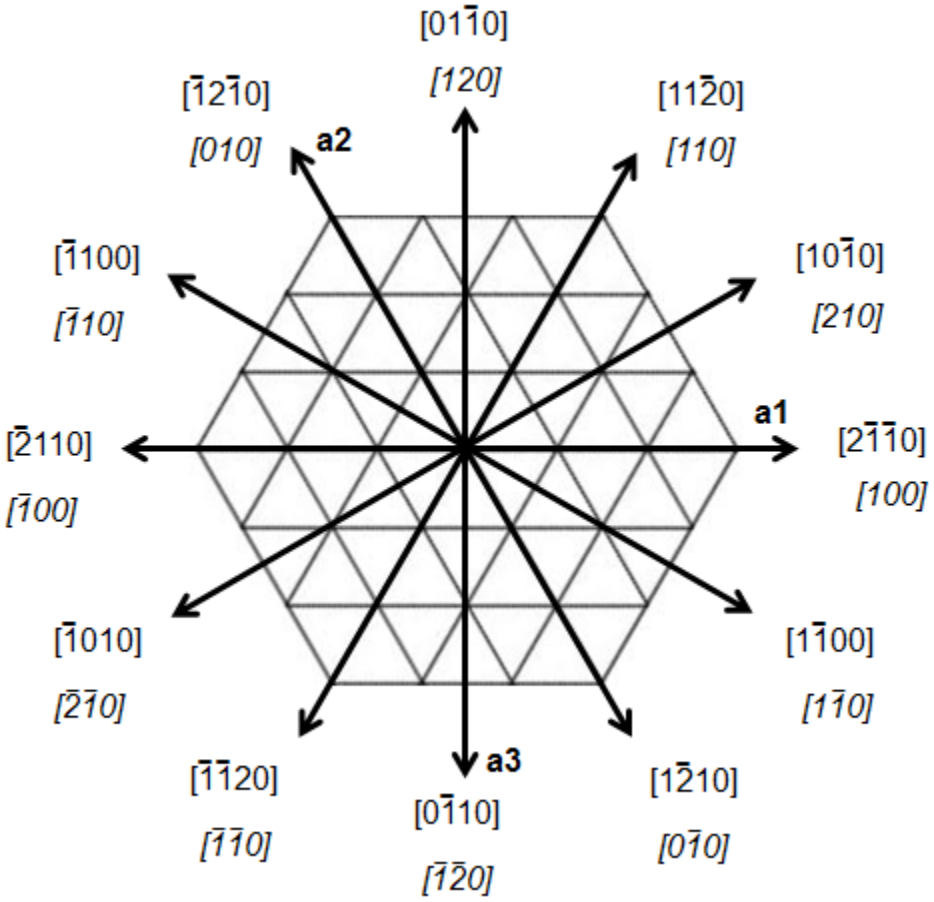

Figure 2.5. The *c* plane of a hexagonal lattice, where 3 indices (a_1, a_2, and a_3) are used to map 2-dimensional space. Each direction is labeled with the 4-index notation on top and the 3-index notation on bottom (italics).

Because the <10$\bar{1}$0> zone axis is 30° around the *c*-axis from the nearest member of the <11$\bar{2}$0> family, it is rare to find a nanowire that allows access to both zone axes within the limited range of the double tilt stage (≤ 20° for both α and β). The nanowire segment shown in Figure 2.6 allowed such a rotation, and thus we could observe the same feature from two directions. This segment contains a pair of edge dislocations that point along the <10$\bar{1}$0> direction, as evidenced by the extra half-plane of Zn atoms at the termination of each basal inclusion. Figure 2.6a shows zigzag contrast both above and below basal inclusions, where none is visible in Figure 2.6b on the <11$\bar{2}$0> zone axis.

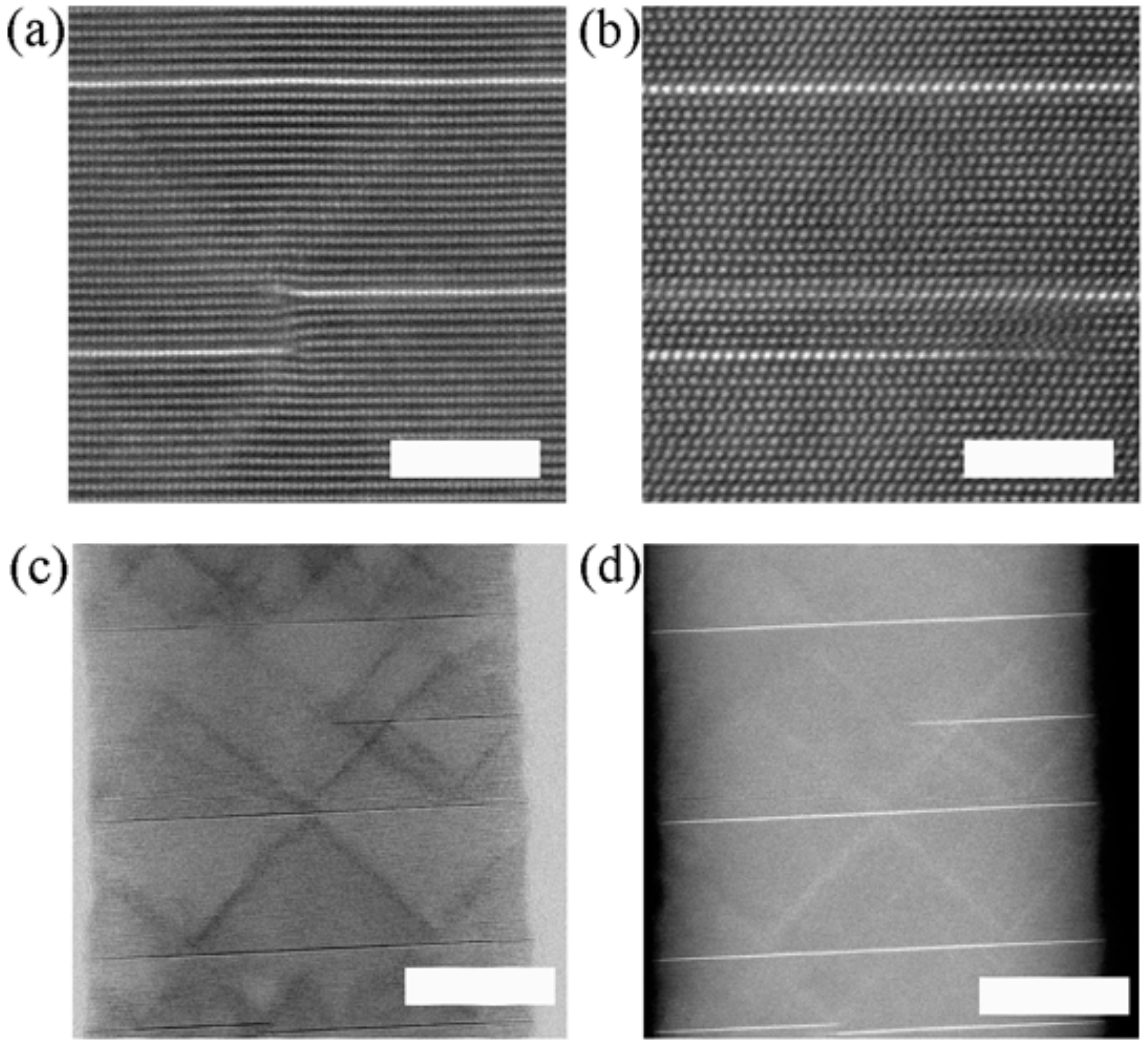

Figure 2.6. Two basal inclusions meet in the body of an IFZO nanowire, as imaged along the (a) $<11\bar{2}0>$ and (b) $<10\bar{1}0>$ zone axes by aberration-corrected STEM (scale bar is 2 nm). Another nanowire segment of IFZO was imaged along $<10\bar{1}0>$ using (c) bright field and (d) high-angle annular dark field detection (scale bar is 8 nm).

Another IFZO nanowire was imaged simultaneously by bright field and dark field STEM (Figure 2.6c and 2.6d). The contrast in both images overlaps perfectly, where the dark contrast in bright field shows that the zigzags are regions of strain (as expected for an IDB) while the bright contrast in dark field proves that these same areas are also indium rich. Contrary to the model of Li *et al*., these images demonstrate that the second IDB lies along the zigzag itself.

Observation of partially-formed IZO wires made from nanoparticle coatings rather than metal films provides further evidence that the zigzag is an IDB. These nanowires were only converted from ZnO locally where nanoparticles attached to the wire surface (Figure 2.7). Along the length of the nanowire, each basal inclusion is paired with a zigzag. Based on this pairing, we deduce that the zigzag accompanies the basal inclusion to allow the IZO structure to penetrate the native

ZnO. This confirms the identity of the zigzag as an IDB, as it is required in order to restore the orientation of the ZnO_4 tetrahedra in the bulk ZnO. Both inclusions terminate at an edge dislocation, as seen in Figure 2.6a. Assuming a plentiful source of In_2O_3, our results suggest that a pair of inclusions will grow together as the dislocation travels into the body of the nanowire. These inclusions encompass a region of ZnO that has been inverted compared to the original wurtzite orientation of the nanowire.

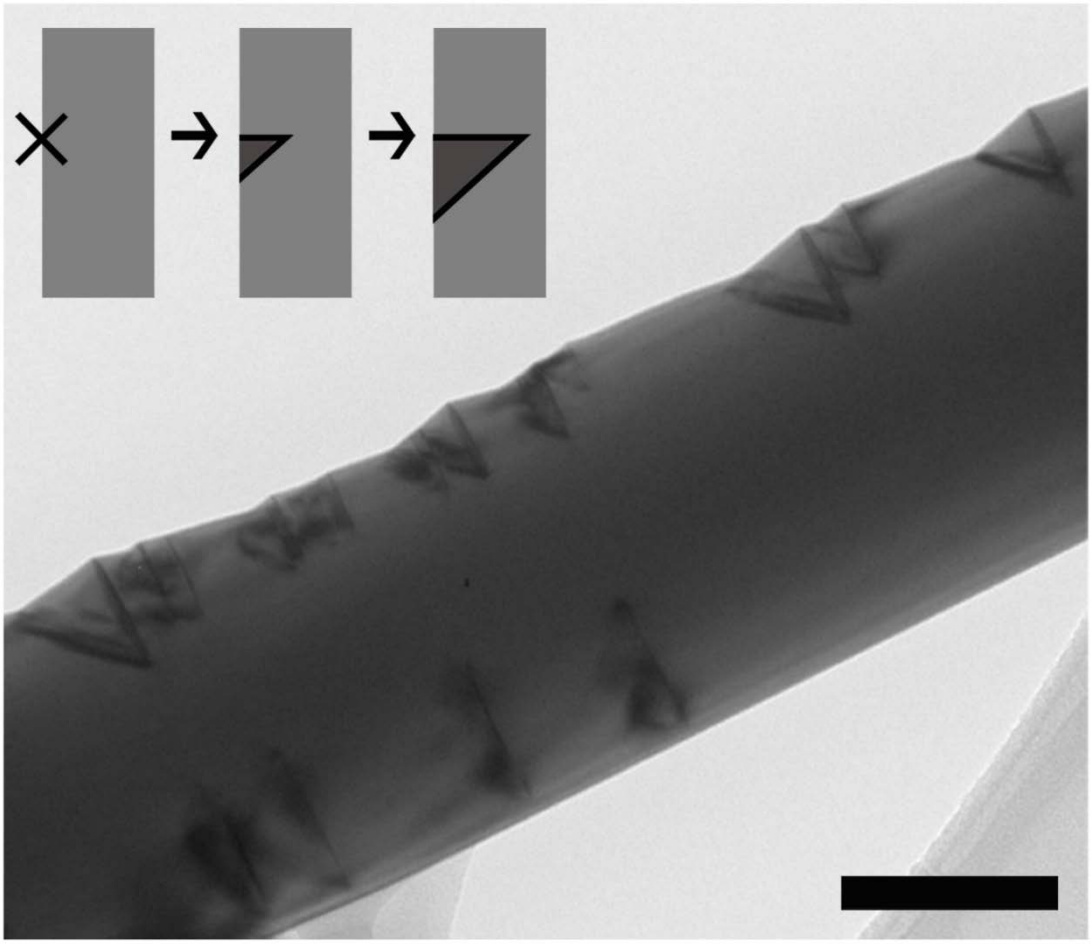

Figure 2.7. Low magnification TEM of an IZO nanowire formed from attached In_2O_3 nanoparticles shows basal/zigzag inclusion pairs as triangles on the nanowire surface. Scale bar is 100 nm. The cartoon inset depicts conversion of a ZnO nanowire to IZO, beginning from a dislocation formed at the surface (marked by an x) and progressing as a pair of inclusions (black lines) surrounding an inverted region (shown in dark gray).

In some atomically-resolved images of IZO, we see that the basal inclusion is a stacking fault; for example, ABAB stacking of zinc atoms above the inclusion may be converted to BCBC on the other side. In these cases, the zigzag is also observed to be a stacking fault, so that the stacking of the bulk ZnO lattice is restored. Similar to the domain inversion, this allows the crystal outside of the region encompassed by the pair of inclusion to remain intact with perfect

stacking as the diffusion front progresses. An example of the two stacking faults is shown in Figure 2.8.

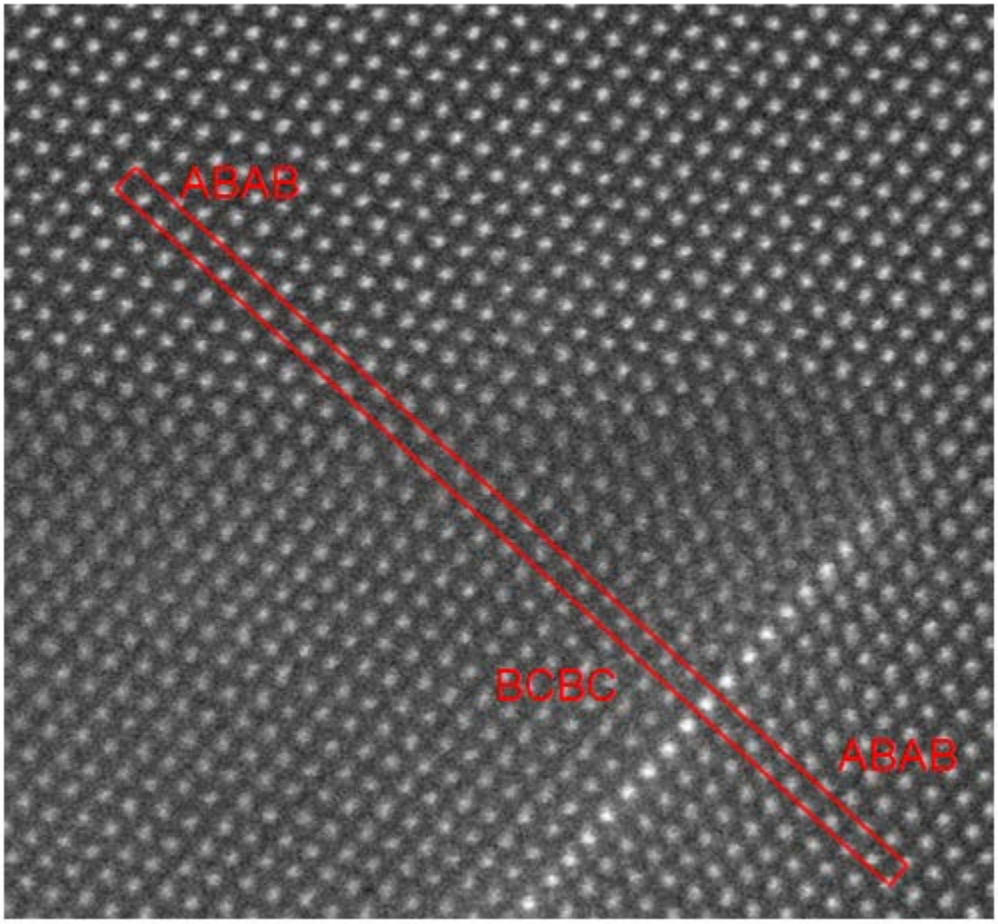

Figure 2.8. Aberration-corrected STEM shows a paired zigzag and basal inclusion, where both layers serve as stacking faults for the ZnO wurtzite lattice. The red lines are intended to guide the eye along a column of atoms that represent the A position.

The dual nature of the zigzag as an IDB and site of indium substitution is also shown by DFT calculations of $In_2O_3(ZnO)_3$. Density functional theory (DFT) within the generalized gradient approximation (PBE)[28] was used to optimize atomic positions and compute total energies of several IZO and IFZO systems. For all calculations, we used the VASP package[29] and projector augmented-wave potentials.[30] Electrons taken to be valence were In $5s^2 4d^{10} 5p^1$, Fe $3p^6 4s^2 3d^6$, Zn $4s^2 3d^{10}$, and O $2s^2 2p^4$. A plane-wave cutoff of 500 eV was used throughout. In systems with iron, Fe 3d states were treated with an effective Hubbard term $U_{eff} = U - J = 3$, 4 or 6 eV.[31,32] Due to the rapid increase in computational expense with unit cell size, calculations were limited to $In_2O_3(ZnO)_3$ and $InFeO_3(ZnO)_3$. The structure in Figure 2.2c (110 atoms) is treated with a 5x2x2 k-point mesh, with k-points for other unit cells scaled accordingly.

Using the starting geometry of a *c*-plane IDB in the center of the slab (as in the model of Li *et al.*), we allow the atomic positions to relax to a local minimum. The resulting structure verifies

that the IDB does lie along the zigzag itself. Within the zigzag, the indium atoms are 5-fold coordinated and they serve to flip the orientation of the ZnO tetrahedra on either side (Figure 2.2c). The most stable structure of the type we propose has a total energy per formula unit that is 18 meV lower than the energy calculated by Da Silva *et al*. The basal inclusion is modeled here with no stacking fault, so the zigzag is also not a stacking fault in the relaxed structure.

For simplicity, we depict the zigzag as a well-defined atomic plane, thus enabling relative comparisons of different single-plane structures, as is the convention in previously published structure models. However, even the atomically-resolved images of zigzags in Figure 2.6 show a distribution of bright contrast across a region of 5-10 atoms, approximately 0.5-1 nm. We conclude that the zigzag is in fact composed of randomly distributed indium, iron and zinc atoms within a diffuse region. A gradual transition between inverted domains, rather than a discrete plane of substitutions, provides several expanded sites that the indium could occupy. Additionally, zigzag movement requires diffusion of the M^{3+} ions, so the ions in the zigzag must remain mobile. In this light, it is not surprising that the zigzag is several atoms wide, rather than a perfect crystal plane.

2.5 Zigzag angle

To assign crystallographic notation to a zigzag plane, we note that it must contain the $[10\bar{1}0]$ vector, which is the viewing angle of the atomically-resolved image in Figure 2.6a. The planes containing this vector are in the family $\{1\bar{2}1\ell\}$, where $1/\ell$ is the fractional intersection of the plane with the *c* axis. The angle formed between (0002) and $(1\bar{2}1\ell)$ is calculated using Equation 2.1.

Equation 2.1

$$\theta = \tan^{-1}[(2/\ell) \cdot (c/a)]$$

Using the *c*/*a* ratio of 1.6 for ZnO, the expected angles for a given ℓ value are listed in Table 2.1. The measured zigzag angles for IZO are in the range of 49-59°, so we assign them ℓ=2-3.

ℓ	θ	$In_2O_3(ZnO)_3$	$InFeO_3(ZnO)_3$ (U=4)
2	58.0°	38 meV	202 meV
3	46.8°	0 meV	31 meV
4	38.7°	18 meV	0 meV
5	32.6°	54 meV	—
6	28.1°	83 meV	—

Table 2.1. Calculated energy per formula unit of two crystal compositions over a range of zigzag angles (θ), relative to the most stable zigzag angle for a given composition.

Elsewhere on the nanowire segment that contained the features in Figures 2.6a and 2.6b, there is a zigzag that does not become sharp upon rotation from [11$\bar{2}$0] to [10$\bar{1}$0]. The IFZO zigzag shown in Figure 2.9a and 2.9b appears to be high angle (~57°) and poorly defined. Because there are three symmetrically equivalent zone axes in the <10$\bar{1}$0> family, this zigzag could be attached to a defect that is 60° rotated from the zone axis. If we assume that the zigzag is bounded by a linear edge orthogonal to the diffusion front, then we can predict the relationship between the true zigzag angle and the apparent angle (depicted in Figure 2.9c). The formula for this calculation is shown in Equation 2.2.

Equation 2.2

$$\tan\theta_o/\cos\alpha = \tan\theta_a$$

where θ_o is the true zigzag angle, α is the rotation around the c axis from the edge dislocation, and θ_a is the apparent angle. For an ℓ=4 zigzag rotated 60° around the c axis, $\theta_a = 58°$; thus, we conclude that the zigzag in Figure 2.9a and 2.9b was in fact ℓ=4.

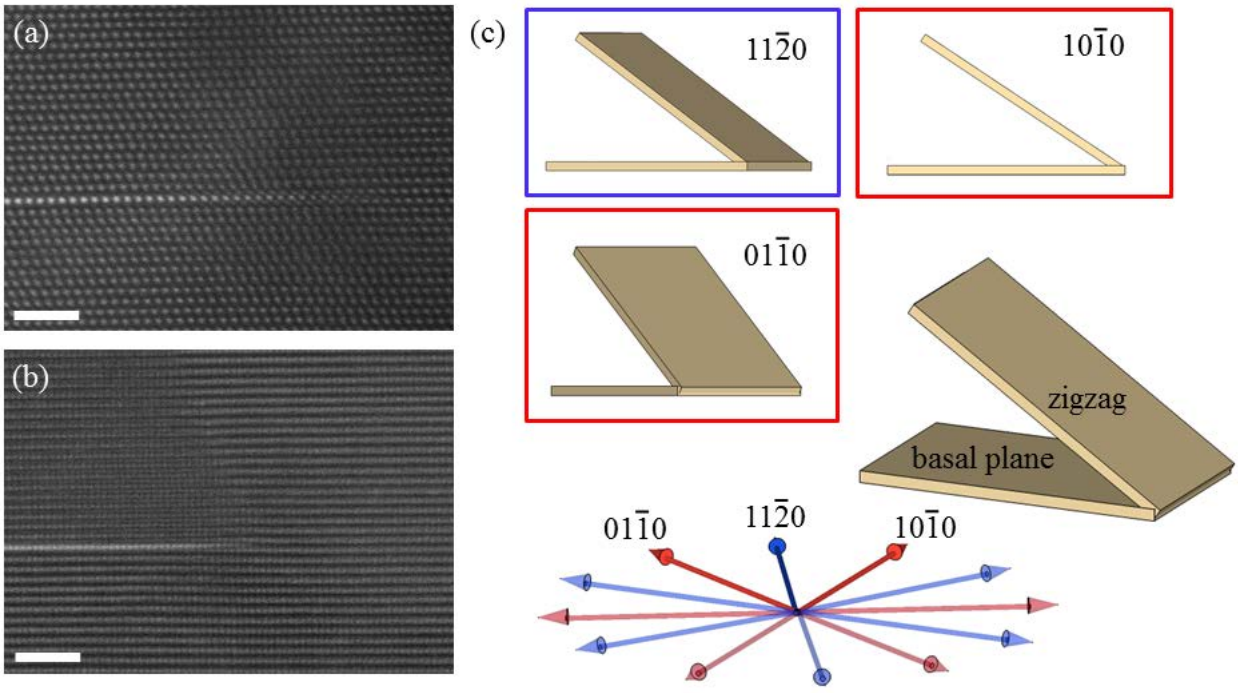

Figure 2.9. A partially formed basal inclusion in an IFZO nanowire was imaged by STEM along the [1120] (a) and the [10$\bar{1}$0] (b) zone axes. Scale bar is 5 nm. The inclusion is terminated by an edge dislocation, which we can assign as a [01$\bar{1}$0] defect. The zone axis has a strong impact on the apparent zigzag angle, as demonstrated by the insets in (c), which are different views of a [10$\bar{1}$0] dislocation.

Using HRTEM, Yu and Mader showed that the displacement of the metal atoms in the IZO lattice are small compared to the shift that would be required to invert the tetrahedra, so the oxygen sublattice must also be displaced.[9] Indeed, our calculated structure predicts that both the metal and the oxygen atoms shift in the *c*-direction as they switch positions across a zigzag. This displacement of the metal atoms is seen in Figures 2.9a and 2.9b where the projections of the *c*-planes on either side of the zigzag are directly overlapped.

Experimental observations by several groups over two decades are unified under our model of zigzags as $\{1\bar{2}1\ell\}$ IDBs, based on STEM and EELS analysis of nanowires synthesized by solid state diffusion between ZnO and iron and/or indium oxide coatings. DFT calculations on this structure in IFZO and IZO yield a lower energy than other proposed structures. The zigzag consists of a region of inverting oxygen and zinc layers, around trigonal bipyramidal substitutions of In^{3+} and/or Fe^{3+} in the Zn sites. This development will enable further optimization and design of these complex oxides.

2.6 Elemental composition of inclusion layers

We find that the zigzag angle depends on the metal composition. A range of 31-48° is observed for samples that contained various proportions of indium and iron, yielding ℓ values of 3-5 for IFZO. DFT total energy calculations of $In_2O_3(ZnO)_3$ and $InFeO_3(ZnO)_3$ confirm this trend (Table 2.1). In IZO, the most stable computed structure corresponds to ℓ=3 (shown in Figure 2.2c). Calculations of IFZO systems are limited in size to $\ell \leq 4$, due to the added computational expense of spin polarization. Three different values of the effective Hubbard term U_{eff} were applied (3, 4, and 6 eV) with no qualitative change in the results. For all zigzag angles, antiferromagnetic ordering of Fe spins was more stable than ferromagnetic ordering (not shown), in agreement with past literature.[4] We find that in IFZO, the most stable zigzag angle corresponds to $\ell \geq 4$ and is shallower than that of IZO, in agreement with experiment.

EELS data on IFZO further illustrate the dependence of the zigzag angle on the metal composition. Local quantities of iron and indium oxide on the nanowire surface determine the availability of each metal to diffuse and the resulting composition of the inclusions in IFZO, as expressed by the chemical formula $In_{2-x}Fe_xO_3(ZnO)_n$. To identify the relative proportion of In and Fe within either the basal or zigzag layers, EELS line scans were performed across both types of inclusions. Signal from the In $M_{4,5}$ edge was integrated from 481-525 eV, and the Fe $L_{2,3}$ edge was integrated from 708-743 eV. In Figure 2.10a, a line scan shows a small Fe concentration across an entire region of IFZO, while the In peak has a sharp increase at the basal inclusion and a small rise at the zigzag. This indicates that the x value for this nanowire segment is low (<1), and indium is the majority M^{3+} ion.

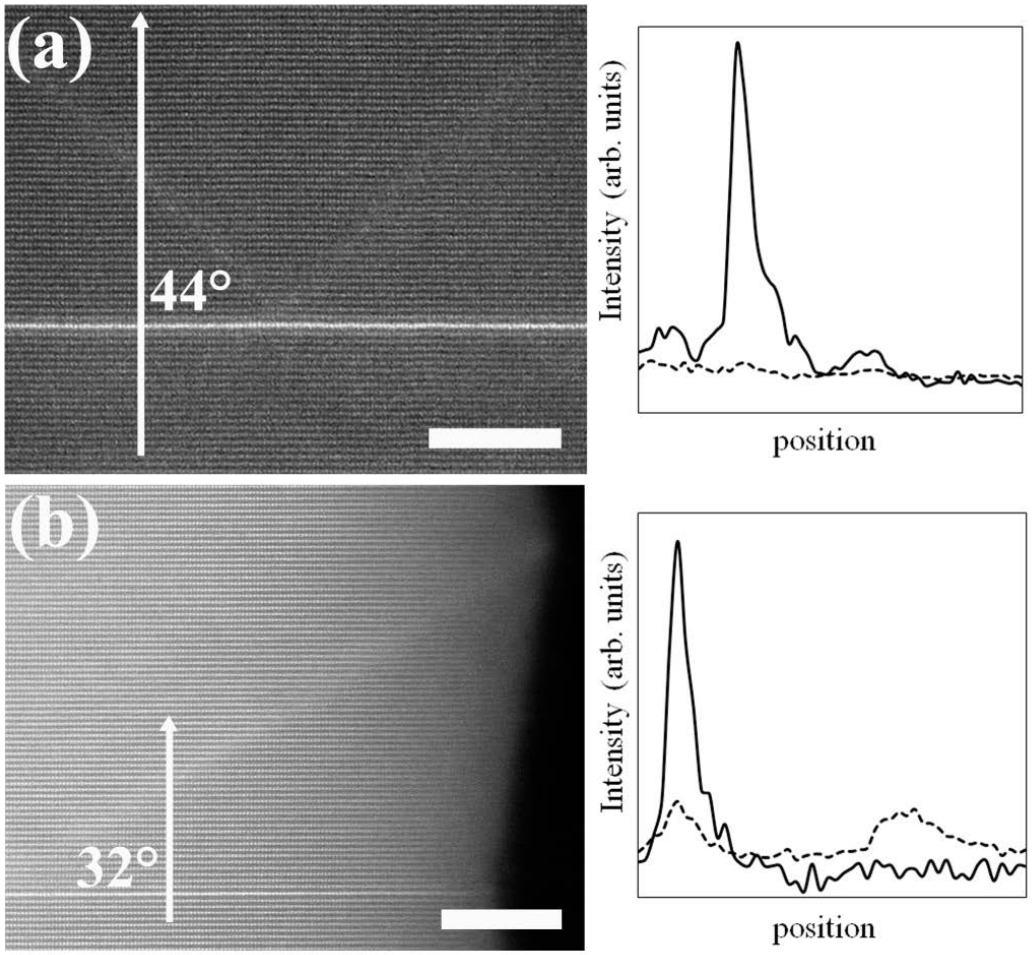

Figure 2.10. EELS line scans were performed across two areas of an IFZO nanowire, and the integrated peaks of In (solid line) and Fe (dashed line) are plotted in the inset. The zigzag in (a) has a higher incident angle on the basal plane, and shows In in both inclusions and no peak for Fe, while the zigzag in (c) has a lower incident angle and a higher ratio of Fe:In. Scale bar is 5 nm.

Analysis of another nanowire segment (Figure 2.10b) shows that the Fe peaks across both types of inclusions are equally strong in this case, and there is no In peak observed in the zigzag. This segment of IFZO therefore has a higher x value than the one shown in Figure 2.10a, and the angle of this inclusion pair is also noticeably lower (32° *vs*. 44°). The distribution of indium and iron between the zigzag and the basal inclusion is likely determined by the stability of the respective ions in those coordination environments. The In^{3+} ion is larger than Fe^{3+} (0.80 Å for 6-coordinate In^{3+} *vs*. 0.65 for high spin Fe^{3+}).[33,34] This contributes to the stability of indium in the octahedral site, making the zigzag the preferred site for iron when both species are present.

The size of each metal ion also contributes to a zigzag's range of preferred angles, depending on its metal composition (e.g. ℓ=3-5 for IFZO). In terms of bonding, zigzag angle indicates how many adjacent MO_5 trigonal bipyramids can be accommodated in a given region of the c-plane. For a shallow zigzag angle, several 5-coordinate metal-oxygen polyhedra may be side by side;

for example, there are two adjacent polyhedra per zigzag for ℓ=4, on average. The angles for selected integer ℓ values and an approximation of which Zn^{2+} positions would be substituted with M^{3+} are shown in Figure 2.11. Due to the diffuse nature of the zigzag, the ℓ index is not required to take a discrete integer value. In ℓ=3 structures, like the one shown in Figure 2.2c, the average number of M^{3+} per plane of ZnO in a given zigzag is 1.5; it is easy to imagine other fractional amounts of metal substitutions between 1 (ℓ=2) and 3 (ℓ=6). DFT calculations support the observed trend of shallower zigzag angles with increasing Fe composition, which is likely due to the large size of the indium ion compared to iron. Steeper zigzags like those found in pure IZO are expected to have fewer MO_5 polyhedra per c-plane of ZnO, because of the strain induced in the surrounding area by the larger cation.

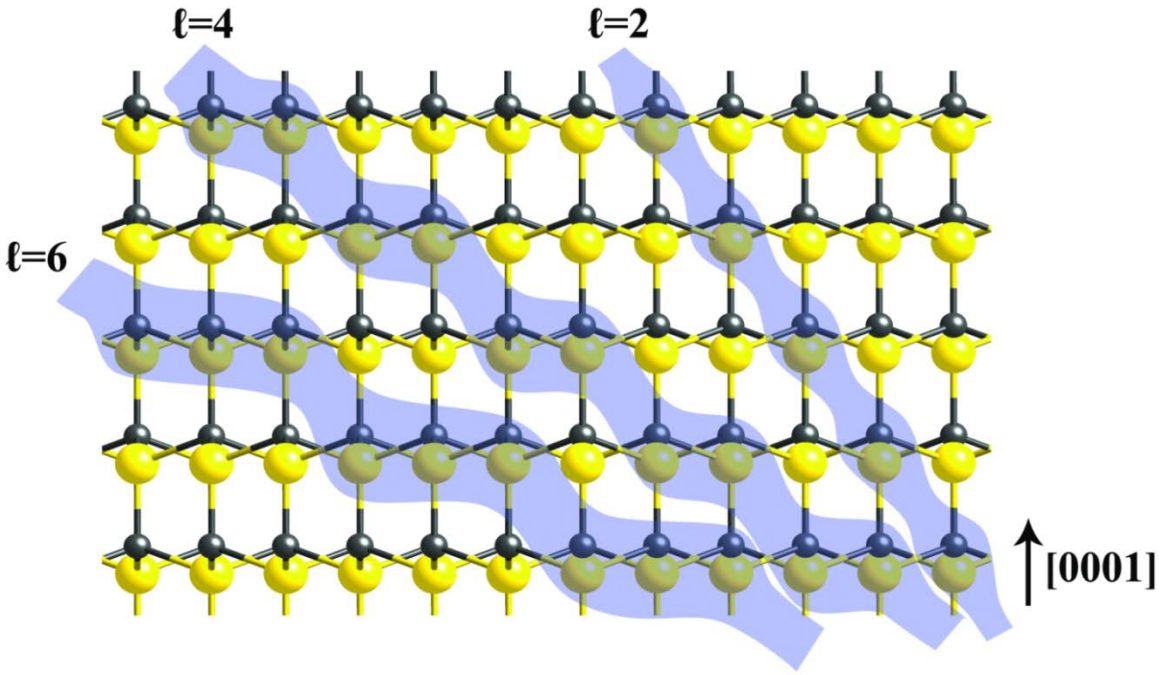

Figure 2.11. Steeper zigzag angles correspond to fewer substituted polyhedra in a given region of the c-plane; thus, smaller ℓ values may be preferred for zigzags composed of larger substituent atoms such as In.

2.7 Deduction of formation mechanism

In addition to clarifying the crystal structure of IZO, our data suggest a mechanism for conversion of ZnO to IZO, depicted in Figure 2.7. During formation of an IZO nanowire, basal inclusion layers move from the surface toward the center as indium diffuses into the ZnO lattice at high temperatures. Because the basal inclusion is an IDB, it must be accompanied by a second IDB during this movement, *i.e.* the zigzag layer. The IDB requires a transition from tetrahedra through trigonal bipyramids, so there must be a plane of metal atoms with coordination number greater than 4. Indium atoms tend to occupy these sites rather than zinc, because of the +3 charge and the longer In-O bond. The identity of the substituted plane is $\{1\bar{2}1\ell\}$, where ℓ depends on the metal composition, rather than $\{10\bar{1}1\}$ as in the model of Yan *et al*.

IZO formation is likely initiated by the creation of a misfit dislocation at the interface between ZnO and the indium/iron oxide coating. For the dislocation to move into the nanowire body, it must undergo positive dislocation climb, which occurs by vacancy annihilation.[35] Because indium diffuses into zinc oxide by a vacancy-mediated mechanism,[36] the concentration of zinc vacancies is higher in the nanowire core; therefore, the chemical potential of vacancies in the core of the nanowire is higher than that in the region of the inclusions. This encourages diffusion of vacancies toward the dislocation, facilitating its climb.

Meanwhile, the zigzag follows the edge dislocation into the center of the nanowire, and the M^{3+} cations diffuse to stabilize the zigzag, due to their larger size and preference for larger coordination number compared to Zn^{2+}. Our proposed mechanism assumes that there is a plentiful supply of M^{3+} in the crystal, as well as Zn vacancies in the ZnO lattice. This assumption is valid for IZO at high temperatures, due to the high diffusion constants of both species in ZnO.[36–38] Recent *in situ* TEM studies have shown how the diffusion of In through ZnO can have very different dynamics, depending on the orientation of the diffusion front.[39] Iron diffusion in ZnO is less well-studied than that of indium, but it is evidently somewhat significant at high temperature, based on the formation of iron zinc oxide (FZO).[40]

There is an alternative description of the dislocation climb during IZO formation, based on the forces near an edge dislocation. The extra half-plane puts compressive stress on the crystal, while the missing half-plane exerts tensile stress.[17] In a homogeneous crystal, these forces are in equilibrium and there is no net movement. However, when a partial inclusion is formed in IZO, the space left by the missing half plane is partially filled by the expanded lattice around the InO_2^- layer, and the tensile stress is reduced. Therefore the dislocation undergoes positive climb to relieve compressive stress in the crystal, while In^{3+} ions dissolved in the lattice continue to precipitate along the dislocation because of the longer bond lengths in that region. This is akin to the Suzuki effect, where a stacking fault width increases in response to adsorption of a large solute atom.[17]

2.8 Assessment of MZO nanowires for visible light harvesting

ZnO and In_2O_3 are both wide band gap materials with no significant light absorption in the visible region, but it has been reported that IZO and related materials are better visible light absorbers than their constituent oxides. Kudo and Mikami found a redshift in absorption onset for IZO that increases for higher inclusion density, up to an onset of 485 nm for $In_2O_3(ZnO)_3$.[11] Tin-doped IZO nanowires have also been shown to have a smaller band gap than ZnO by UV-visible absorption and photoluminescence.[41] If the band gap of IZO and related MZO complex oxides can be controlled, then these materials will hold promise as photoelectrochemical anodes for solar energy conversion.

Using DFT, Walsh et al. calculated the band structure for IZO in an attempt to explain the increased visible light absorption compared to the component oxides.[12] They found that the optical absorption in IZO is a direct transition from the valence band maximum in ZnO to a hybridized conduction band minimum composed of In, Zn, and O states. However, these calculations were based on the crystal structure proposed by Yan et al., which we have shown

earlier in this chapter to be problematic.[21] Further studies in this area will necessitate repeating these calculations using the crystal structure shown in Figure 2.2c, in case the orientation of the zigzag has an effect on the band structure.

IZO was synthesized to test experimentally for enhanced visible light absorption. ZnO and In_2O_3 powders were mixed by mortar and pestle in a 2:1 atomic ratio and then sintered in an oxygen atmosphere at 900 °C. Reflectance (R) of the samples were measured inside an integrating sphere; for simplicity, absorption was calculated to be $A = R_{max} - R$.[42,43] After conversion to IZO, the pale-colored powder of mixed constituent oxides becomes bright yellow (Figure 2.12b), demonstrating that the resulting material is absorbing the higher energy portion of the visible spectrum. Following Equation 1.1, we calculate a band gap of 2.65 eV for IZO in the 2:1 Zn:In ratio, or nominally $In_2O_3(ZnO)_4$.

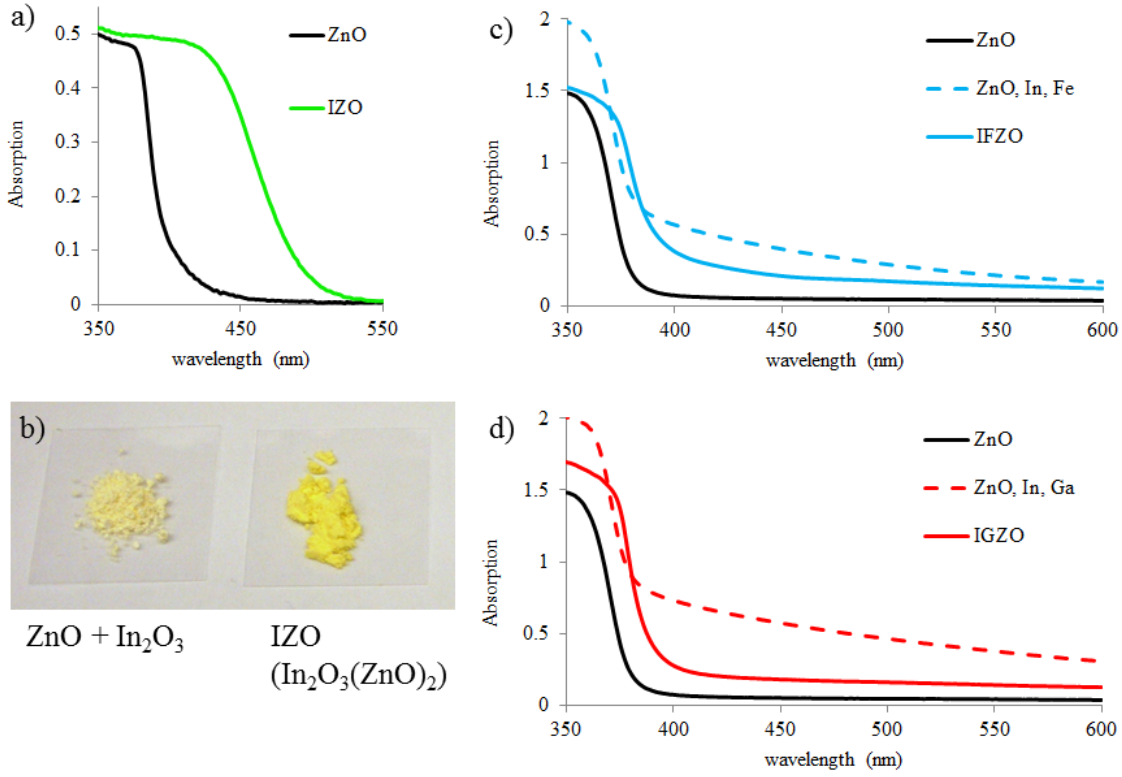

Figure 2.12. UV-visible light absorption of MZO materials. (a) IZO bulk powder has a lower energy absorption onset compared to ZnO, calculated as 1-R. (b) There is a noticeable color change of IZO compared to the mixture of starting materials. (c) IFZO nanowires made with 20 nm of In and 10 nm of Fe (solid blue line). (d) IGZO nanowires made with 20 nm of In and 20 nm of Ga (solid red line). Both IFZO and IGZO nanowire arrays demonstrate the same effect, compared to the ZnO nanowire array before (black line) and after metal deposition (dashed line). Absorption data in (c) and (d) were calculated as –log(T).

Nanowire arrays of IFZO and IGZO were synthesized (as described above) on quartz substrates for optical testing. Optical absorption traces of nanowires with and without metal coating and after annealing are shown in Figure 2.12c and 2.12d. Absorption of the nanowire arrays was

calculated from the transmission (T) as –log(T). Reflection from the metal coating attenuates the transmitted light, causeing an apparent enhancement in absorption across a broad portion of the visible spectrum. After annealing, the metal has been incorporated into the nanowires, so the background absorption between 400 and 600 nm is diminished. Meanwhile, the onset of $(\alpha \cdot h\nu)^2$ has shifted to lower energy, from 3.31 eV for ZnO nanowires to 3.21 eV for IFZO and 3.23 eV for IGZO, verifying that the band gaps of these materials are also smaller than that of ZnO.

Enhanced light absorption enables IZO to act as an effective catalyst for PEC energy conversion. IZO powder was tested for its ability to evolve hydrogen gas under illumination. RuO_2 (1% by mass) was deposited on the powder from $Ru_3(CO)_{12}$ in acetone, followed by solvent evaporation and annealing in air at 350 °C. The catalyst powder was then dispersed in water and illuminated by the full spectrum of a 450 W Xe lamp, and gas output was measured by gas chromatography. As shown in Figure 2.13, the powder produced approximately 0.5 μmol of H_2 per gram of IZO per hour of illumination. The linear rate of hydrogen evolution over 11 hours indicates that the catalyst is not quickly saturated; this is beneficial, as saturation would be detrimental to long-term solar fuel production.

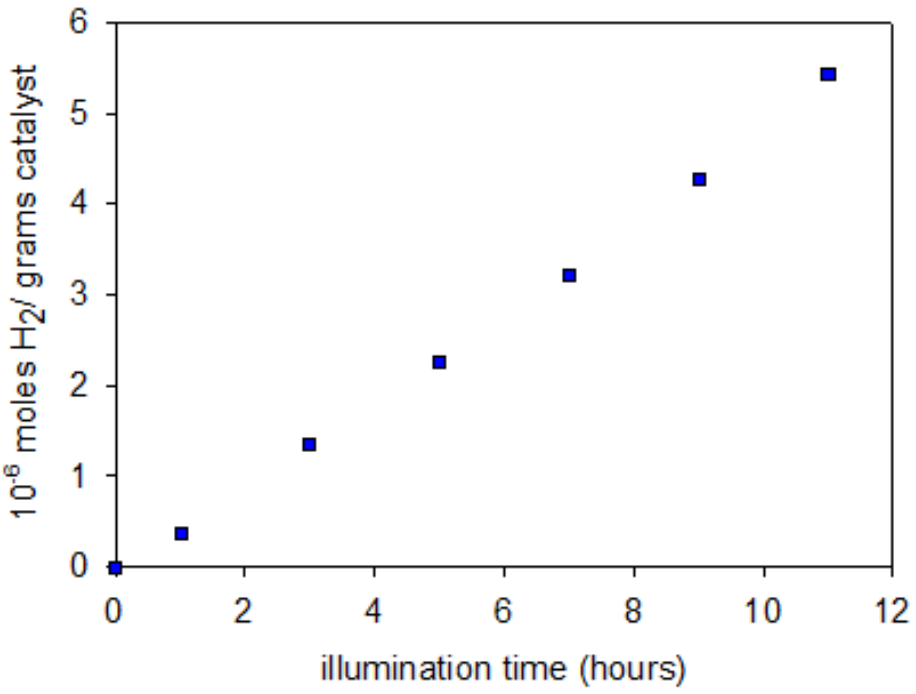

Figure 2.13. H_2 gas produced by IZO powder with 1% RuO_2 co-catalyst under combined visible and UV illumination.

The STH efficiency was not calculated from these data, due to the difficulty of accurately measuring the illumination input. Standards for comparing water splitting materials, as detailed in Chapter 1, are easily applied to 2D electrodes, which can be placed normal to the light source to simulate real-world device activity. Turbid solutions of powder, on the other hand, will receive different intensity of light (and therefore produce hydrogen at different rates) depending on the path length of the cell and the solution concentration. An additional limitation of this

experiment is that the rate of oxygen evolution over the same time period (not shown) was greater than expected based on the 2:1 H_2:O_2 ratio of complete water splitting (Scheme 1.1). These tests may have suffered from excess oxygen due to air leakage into the evacuated cell; alternatively, some portion of the evolved hydrogen may have adsorbed to the catalyst surface and/or undergone further chemical reaction.

IGZO nanowire arrays were synthesized on planar ITO, in order to provide electrical contact between the substrate and the nanowire surface. These arrays were assembled into electrodes using an In/Ga eutectic and silver paint to connect the ITO surface with a copper wire for easier handling and interfacing with the potentiostat. Results from electrochemical characterization of these electrodes are shown in Figure 2.14. Photocurrent under 500 mW/cm^2 illumination through an AM 1.5 spectral filter (i.e. 5 suns) appears to have a slow onset beginning at negative voltages, but the data are noisy and the plot of I^2 (not shown) does not have an obvious linear region which can be fit to determine V_{fb}. Mott-Schottky analysis of these electrodes did not lead to a value for V_{fb}, due to complicated circuit fits for the EIS plots, which obscured the true value of C in the depletion region. Additionally, using the model of cylindrical capacitance from Mora-Seró et al.,[44] the calculated V_{fb} was found to be very sensitive to the physical dimensions of the nanowire array. Density of our nanowire arrays can be estimated from SEM, but should be measured more accurately for use in this model.

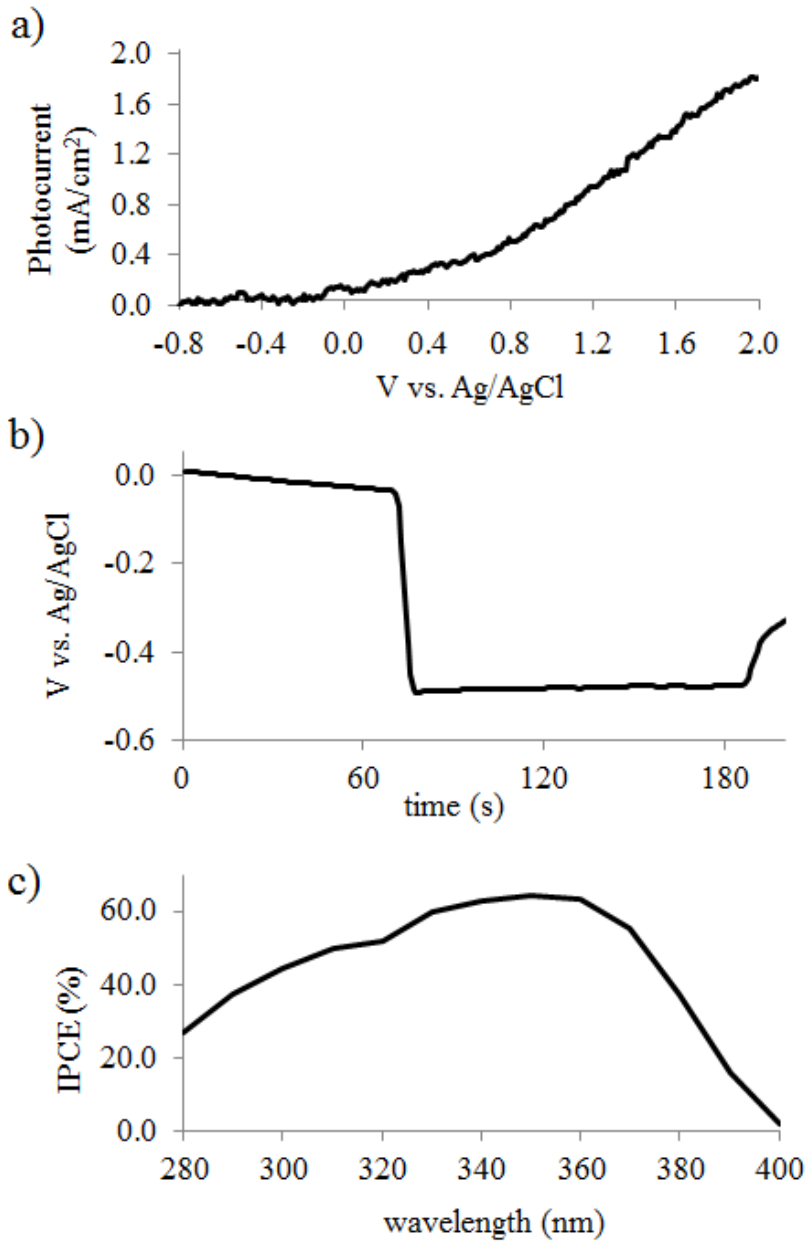

Figure 2.14. Results from electrochemical testing of IGZO nanowire electrodes made with 10 nm In and 7.5 nm Ga coatings. Linear voltammetry (a) and open circuit potential (b) were measured under 5 suns of simulated AM 1.5 solar illumination. (c) The IPCE spectrum was collected at 2 V. Photocurrent values in (a) were calculated by subtracting the dark response from the illuminated response. All experiments were performed in 0.5 M Na_2SO_4 (aq) at pH = 7.

Fortunately, the measurement of V_{oc} under intense illumination was relatively straightforward (Figure 2.14b) and allowed us to measure V_{fb} for IGZO. Under 5 suns light intensity, we get a value of V_{fb} = -0.48 V vs Ag/AgCl, or -0.28 V vs. SHE. The lamp was at maximum intensity for this measurement; it is possible that the electrode was not fully saturated, so the true V_{fb} may be slightly higher energy. If we interpolate to pH = 7 for V_{fb} = -0.2 V vs SHE based on

measurements of ZnO in the literature,[45] then our result suggests that the flat band of IGZO has been shifted to slightly higher energy. We also find that the IPCE of IGZO nanowires is high in the UV region, as much as 64% at 350 nm (Figure 2.14c). Meanwhile, the onset of $(\alpha \cdot h\nu)^2$ for this sample is 3.2 eV, which matches the band gap determined above in Figure 2.12.

The stability of ZnO in water has been investigated previously, and it was found to dissolve significantly under conditions of both high and low pH exposure in the dark, as well as UV illumination.[46,47] We observed this instability here, as nanowire arrays were prone to etching during electrochemical testing, especially under intense light and stirring. This dissolution may be the cause of some of the above mentioned difficulties with photocurrent and Mott-Schottky measurements on nanowire arrays. IPCE of the same IGZO sample measured in Figure 2.14 was no higher than 40% after a second exposure to measurement conditions. A ZnO array was allowed to soak overnight in a pH = 7 buffered phosphate solution and was significantly etched afterwards. Figure 2.15a shows the array before etching, where the tips of nanowires are narrow and easily differentiated, while Figure 2.15b shows the etched array with exposed cracks in substrate and wider stumps where the base of the array was formed.

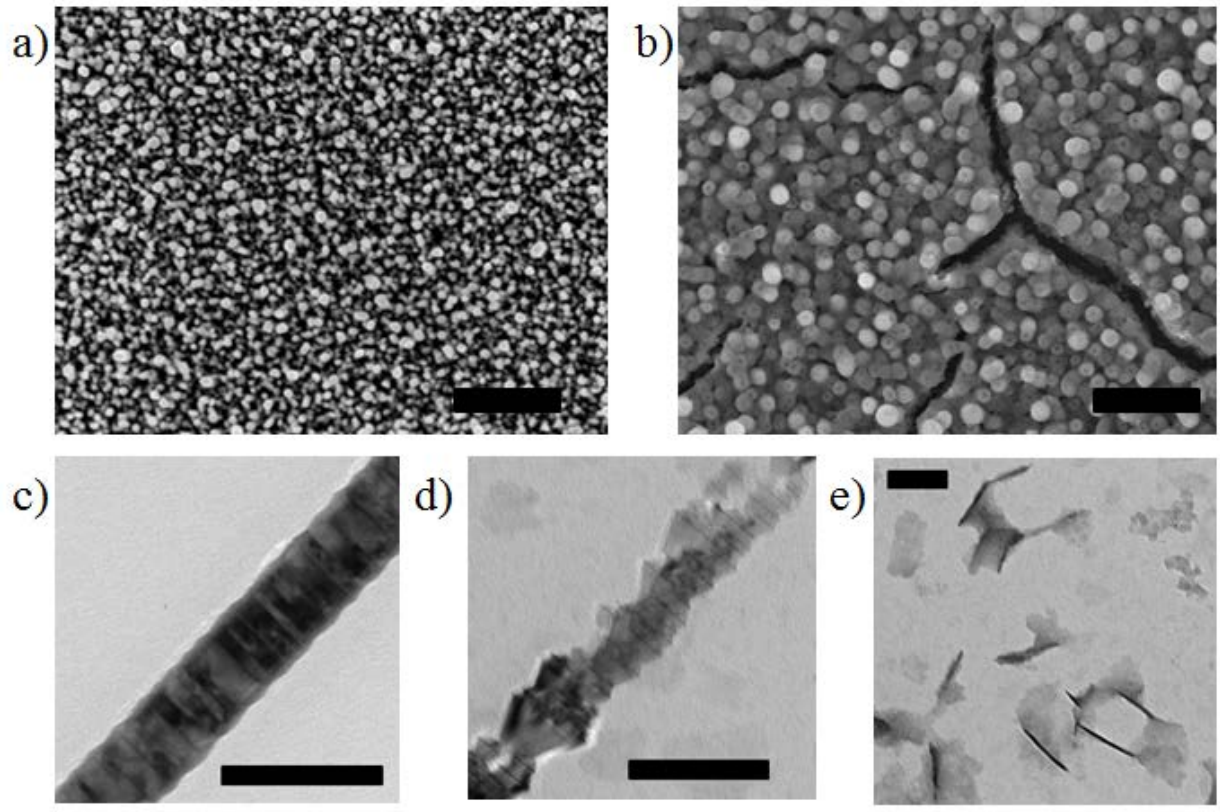

Figure 2.15. Top row shows SEM images of a ZnO array (a) before and (b) after overnight soaking in a pH = 7 buffer (scale bars for are 1 μm). Bottom row shows TEM images of IZO nanowires (a) before etching and after (b) 1 minute and (c) 2 minutes of immersion in dilute HCl (scale bars are 100 nm).

MZO arrays are also etched in solution, and their etching is anisotropic along the length of the nanowire. To observe the etching of MZO nanowires in greater detail, a suspension of IZO nanowires in IPA was mixed with dilute HCl to make a 2 mM acid solution. The nanowires were allowed to soak for a short period of time; the suspension was dropcast and dried on a thin film carbon membrane for TEM analysis at 1 minute intervals (Figure 2.15c-e). After 1 minute of etching, the patterned surface of the nanowire demonstrates that the ZnO exposed between inclusions is etched much faster than the inclusions themselves. After 2 minutes, there are deposits that appear to be isolated inclusion layers with little or no ZnO between them. This simple experiment open up the possibility of a top-down synthesis of atomically thin layers of In_2O_3, binary oxide compounds incorporating Fe^{3+} or Ga^{3+}, or even more complex alloys depending on the elemental distribution in the MZO starting material.

References

(1) Cannard, P. J.; Tilley, R. J. D. *J. Solid State Chem.* **1988**, *73*, 418–426.
(2) Kimizuka, N.; Mohri, T.; Matsui, Y.; Siratori, K. *J. Solid State Chem.* **1988**, *74*, 98–109.
(3) Uchida, N.; Bando, Y.; Nakamura, M.; Kimizuka, N. *J. Electron Microsc. (Tokyo).* **1994**, *43*, 146–150.
(4) Hörlin, T.; Svensson, G.; Olsson, E. *J. Mater. Chem.* **1998**, *8*, 2465–2473.
(5) Kimizuka, N.; Isobe, M.; Nakamura, M.; Mohri, T. *J. Solid State Chem.* **1993**, *103*, 394–402.
(6) Kimizuka, N.; Mohri, T.; Matsui, Y.; Siratori, K. *J. Solid State Chem.* **1988**, *74*, 98–109.
(7) Kimizuka, N.; Mohri, T. *J. Solid State Chem.* **1989**, *107*, 98–107.
(8) Ohta, H.; Seo, W.-S.; Koumoto, K. *J. Am. Ceram. Soc.* **1996**, *79*, 2193–2196.
(9) Hiramatsu, H.; Seo, W.-S.; Koumoto, K. *Chem. Mater.* **1998**, *10*, 3033–3039.
(10) Nomura, K.; Ohta, H.; Ueda, K.; Kamiya, T.; Hirano, M.; Hosono, H. *Science* **2003**, *300*, 1269–1272.
(11) Kudo, A.; Mikami, I. *Chem. Lett.* **1998**, 1027–1028.
(12) Walsh, A.; Da Silva, J. L.; Yan, Y.; Al-Jassim, M.; Wei, S.-H. *Phys. Rev. B* **2009**, *79*, 073105.
(13) Kimizuka, N.; Isobe, M.; Nakamura, M. *J. Solid State Chem.* **1995**, *116*, 170–178.
(14) Schmid, H.; Okunishi, E.; Mader, W. *Ultramicroscopy* **2013**, *127*, 76–84.
(15) Schmid, H.; Okunishi, E.; Oikawa, T.; Mader, W. *Micron* **2012**, *43*, 49–56.
(16) Yu, W.; Mader, W. *Ultramicroscopy* **2010**, *110*, 411–417.
(17) Li, C.; Bando, Y.; Nakamura, M.; Onoda, M.; Kimizuka, N. *J. Solid State Chem.* **1998**, *139*, 347–355.
(18) Yan, Y.; Da Silva, J. L. F.; Wei, S.-H.; Al-Jassim, M. *Appl. Phys. Lett.* **2007**, *90*, 261904.
(19) Da Silva, J.; Yan, Y.; Wei, S.-H. *Phys. Rev. Lett.* **2008**, *100*, 255501.
(20) Wen, J.; Wu, L.; Zhang, X. *J. Appl. Phys.* **2012**, *111*, 113716.
(21) Goldstein, A. P.; Andrews, S. C.; Berger, R. F.; Radmilovic, V. R.; Neaton, J. B.; Yang, P. *ACS Nano* **2013**, *7*, 10747–10751.
(22) Huang, M. H.; Mao, S.; Feick, H.; Yan, H.; Wu, Y.; Kind, H.; Weber, E.; Russo, R.; Yang, P. *Science* **2001**, *292*, 1897–1899.
(23) Huang, M. H.; Wu, Y.; Feick, H.; Tran, N.; Weber, E.; Yang, P. *Adv. Mater.* **2001**, *13*, 113.

(24) Greene, L. E.; Yuhas, B. D.; Law, M.; Zitoun, D.; Yang, P. *Inorg. Chem.* **2006**, *45*, 7535–7543.
(25) Andrews, S. C.; Fardy, M. A.; Moore, M. C.; Aloni, S.; Zhang, M.; Radmilovic, V. R.; Yang, P. *Chem. Sci.* **2011**, *2*, 706–714.
(26) Moore, M. C. Metal Oxide Nanostructured Materials for Optical and Energy Applications, 2013.
(27) Seo, W.-S.; Jo, H. H.; Lee, K.; Park, J. T. *Adv. Mater.* **2003**, *15*, 795–797.
(28) Perdew, J.; Burke, K.; Ernzerhof, M. *Phys. Rev. Lett.* **1996**, *77*, 3865–3868.
(29) Kresse, G.; Furthmüller, J. *Phys. Rev. B* **1996**, *54*, 11169–11186.
(30) Kresse, G.; Joubert, D. *Phys. Rev. B* **1999**, *59*, 1758–1775.
(31) Dudarev, S. L.; Botton, G. A.; Savrasov, S. Y.; Humphreys, C. J.; Sutton, A. P. *Phys. Rev. B* **1998**, *57*, 1505–1509.
(32) Wang, L.; Maxisch, T.; Ceder, G. *Phys. Rev. B* **2006**, *73*, 195107.
(33) Van Horn, J. D. Electronic Table of Shannon Ionic Radii http://v.web.umkc.edu/vanhornj/shannonradii.htm (accessed Dec 30, 2011).
(34) Shannon, R. D. *Acta Crystallogr.* **1976**, *A32*, 751–767. Electronic table by J. David Van Horn, (2.
(35) Hirth, J. P.; Lothe, J. *Theory of Dislocations*; 1982.
(36) Nakagawa, T.; Matsumoto, K.; Sakaguchi, I.; Uematsu, M.; Haneda, H.; Ohashi, N. *Jpn. J. Appl. Phys.* **2008**, *47*, 7848–7850.
(37) Erhart, P.; Albe, K. *Appl. Phys. Lett.* **2006**, *88*, 201918.
(38) Tomlins, G. W.; Routbort, J. L.; Mason, T. O. *J. Appl. Phys.* **2000**, *87*, 117–123.
(39) Wang, S.; Lu, M.; Manekkathodi, A.; Liu, P.; Lin, H.-C.; Li, W.-S.; Hou, T.-C.; Gwo, S.; Chen, L.-J. *Nano Lett.* **2014**, *14*, 3241–3246.
(40) Li, C.; Bando, Y.; Nakamura, M.; Kimizuka, N. *J. Solid State Chem.* **1999**, *142*, 174–179.
(41) Na, C. W.; Bae, S. Y.; Park, J. *J. Phys. Chem. B* **2005**, *109*, 12785–12790.
(42) Khan, S. U. M.; Al-Shahry, M.; Ingler, W. B. *Science* **2002**, *297*, 2243–2245.
(43) Murphy, a. *Sol. Energy Mater. Sol. Cells* **2007**, *91*, 1326–1337.
(44) Mora-Seró, I.; Fabregat-Santiago, F.; Denier, B.; Bisquert, J.; Tena-Zaera, R.; Elias, J.; Lévy-Clément, C. *Appl. Phys. Lett.* **2006**, *89*, 203117.
(45) Cardon, F.; Gomes, W. *J. Phys. D. Appl. Phys.* **1978**, *11*, L63–L67.
(46) Fruhwirth, O.; Herzog, G.; Poulios, J. *Surf. Technol.* **1985**, *24*, 293–300.
(47) Han, J.; Qiu, W.; Gao, W. *J. Hazard. Mater.* **2010**, *178*, 115–122.

Chapter 3

Conversion of TiO_2 Nanowires to Ternary Titanates by Surface Decoration with Transition Metal Oxides

3.1 TiO_2 nanowires as a precursor for ternary titanates

The family of compounds with the formula $MTiO_3$, which are isostructural with the mineral $FeTiO_3$ or ilmenite, are known to be visible-light-absorbers. Their band gaps are reduced compared to TiO_2, due to the appearance of a new electronic excitation between metal ions, known as metal-metal charge transfer (MMCT) or intermetallic charge transfer (IMCT).[1,2] For example, in $NiTiO_3$, the MMCT is from the 3d band of Ni^{2+}, which has a d^8 electron configuration, to the 3d band of Ti^{4+}, which is d^0. The onset of absorption from this event is at 2.8 eV. Band gaps for other $MTiO_3$ materials have been measured as low as 2.4 eV.[1] Because of their optical properties, these materials have attracted attention previously as possible photoanodes for water splitting. However, photocurrent obtained from ilmenite electrodes is less impressive than what would be expected from their visible absorption spectrum.[3,4] One reason for this deficiency may be reduced mobility of the charge carriers excited by MMCT due to the formation of polarons.[2,5]

Aside from improving the bulk property of visible light absorption, conversion of TiO_2 to ternary titanates is interesting for its possible effect on the material's surface properties. The OER performance in complex oxides with perovskite structure has been shown to be highly tunable based on elemental composition and d orbital filling.[6] Analogously, predicted rates of oxygen evolution for a wide range of oxide surfaces have been shown to depend on the binding energy of reaction intermediates.[7–9] The requirement for each intermediate steps to be catalyzed by the same energy of electrons results in a "volcano curve", where the maximum oxygen yield is expected from mid-range value of the descriptor ($\Delta G_{O*} - \Delta G_{HO*}$).[7] This means that the reaction $HO* \rightarrow O* + H^+ + e^-$ should proceed somewhat uphill, but not so much that it introduces an overpotential into the following steps of OER.

This principle was used to optimize the choice of transition metal incorporated into the TiO_2 rutile surface for maximum efficiency of OER catalysis.[10] Mn in particular stood out as one of the more advantageous surface substituents. Doping TiO_2 nanowires with Mn and other transition metals has been shown to increase their usefulness as a photoanode.[11] Attracted by the possibility of both increased light absorption and increase surface reactivity, we investigate methods of incorporating Mn, Co, and Ni into TiO_2 nanowires using surface coatings.

The ideal structure would benefit from some surface penetration of the alloying elements, while falling short of complete conversion to $MTiO_3$ throughout the nanowire, so that the single-crystal TiO_2 at the center of the nanowire as a 1D conductive channel is retained. This area of nanoscale synthesis is relatively unexplored, so it is useful to explore a range of synthetic conditions in order to optimize the partial conversion process. In this work, we use metal oxide coatings to decorate the TiO_2 nanowires and provide a source of M^{2+} ions for conversion into a ternary structure. Several varieties of oxide coatings are employed: salt coating, chemical bath deposition, and physical attachment of nanoparticles. After coating the nanowire, the system is annealed in order for the metal ions to become mobile and diffuse across the boundary into the TiO_2.

3.2 Nanoparticle coating of nanowires for local conversion

To investigate the local conversion of TiO_2 to $MTiO_3$, nanoparticles of MnO and Co_3O_4 were synthesized. These materials were chosen because their synthesis in the form of size- and shape-controlled nanoparticles have been well established.[12–15] We expect that MnO can combine directly with TiO_2 to form an ilmenite structure (Scheme 3.1), whereas Co_3O_4 contains a mixture of both Co^{3+} and Co^{2+}, and therefore requires preliminary conversion to CoO before reacting to form $CoTiO_3$. Phase diagrams for the Mn-Ti-O and Co-Ti-O system for varying temperature and partial pressure of oxygen are available in the literature.[16]

$$MnO + TiO_2 \rightarrow MnTiO_3$$

$$CoO + TiO_2 \rightarrow CoTiO_3$$

Scheme 3.1. Chemical reactions involved in the synthesis of ilmenite ($MTiO_3$) from the constituent oxides.

TiO_2 nanowires were grown using a molten salt synthesis from Liu *et al*.[11] Briefly, NaCl and Na_2HPO_4, and TiO_2 nanoparticles (P25 from Degussa) were ground by mortar and pestle and then heated over the melting point of the salts (825 °C). The rutile phase nanoparticles seed the growth of rutile nanowires in the [001] direction with (100) side walls and a rectangular cross-section. One major advantage of the molten salt synthesis is that it doesn't require any surfactant or organic compounds; the bare nanowire surface is hydrophilic, so the nanowires can be dispersed easily in water.

MnO nanoparticles were synthesized from a mixture of manganese acetate, oleic acid, water, and trioctylamine. The mixture was refluxed under nitrogen flow at 320°C until the solution turned from clear and yellow to opaque and green.[13] The resulting solids were washed with ethanol and hexanes, and then centrifuged at low speed (300 rpm) to obtain a solution of isolated particles in the supernatant. Particles were roughly hexagonal in cross-section (presumed to be octahedra, also known as hexapods) and mostly monodisperse in size at approximately 30 nm.

In order to observe the reaction between MnO and TiO_2 on the nanoscale, we attempt to assemble a sparse coating of MnO nanoparticles on the surface of the TiO_2 nanowires. A holey

Si_3N_4 membrane was dropcast first with an aqueous suspension of TiO_2 nanowires, and then with a hexane solution of MnO nanoparticles. The nanoparticles mostly self-assembled on the flat {100} nanowire facets. These superstructures prevent us from analyzing a single wire-particle interface for MnO-TiO_2. Instead, we observe the aggregation and loss of shape in the particles at high temperature (800 °C), followed by a merging of the nanowire and nanoparticles after prolonged annealing, as shown in Figure 3.1.

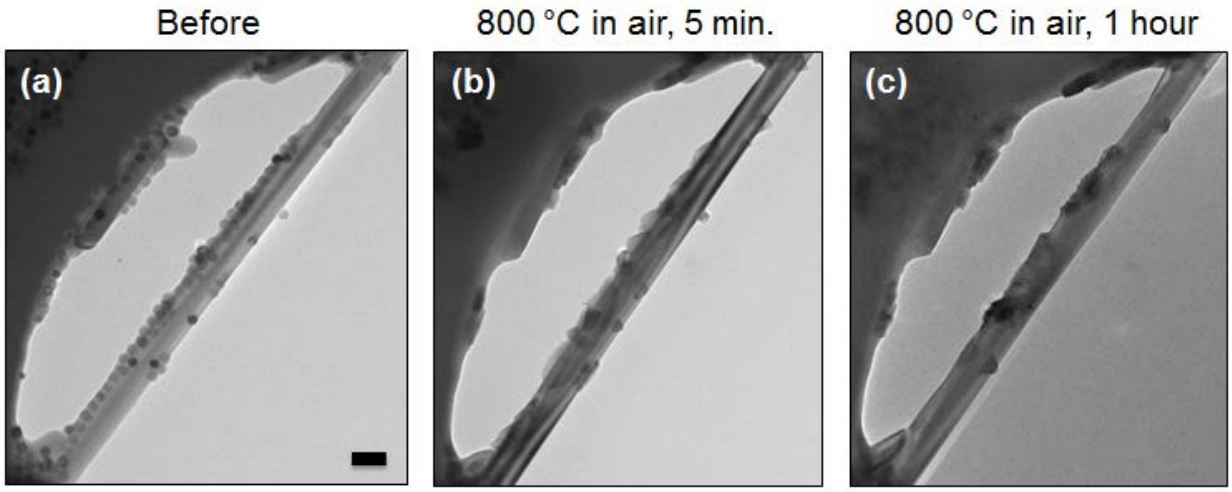

Figure 3.1. MnO particles deposited on TiO_2 nanowires for *ex situ* heating and imaging by TEM. Particles aggregate and change shape after short annealing times (b) and begin to incorporate into the nanowire during longer anneals (c). Scale bar is 100 nm.

Turning to the Co-Ti-O system, we synthesized Co_3O_4 cubic-shaped particles with no surfactant in an aqueous medium, following a method in the literature.[14] Briefly, an aqueous solution of NaOH and $NaNO_3$ was heated in an oil bath, and $Co(NO_3)_2$ (aq) was introduced by hot injection. The reaction proceeded for 19 hours until the solution turned black; the solids were then washed with HCl and removed by centrifugation. The nanoparticles were cubic with a diameter of approximately 50 nm.

A holey Si_3N_4 grid was dropcast with a dilute aqueous mixture of TiO_2 nanowires and Co_3O_4 cubic nanoparticles. Several regions were found containing an interface between a nanowire and a single particle or a group of several particles, and these were imaged by low-resolution TEM. The grid then underwent rapid thermal annealing (RTA) at 785 °C in Ar gas for 30 seconds. After annealing, there are noticeable changes to the nanowire-nanoparticle system. Several examples of these transformations are shown in Figure 3.2.

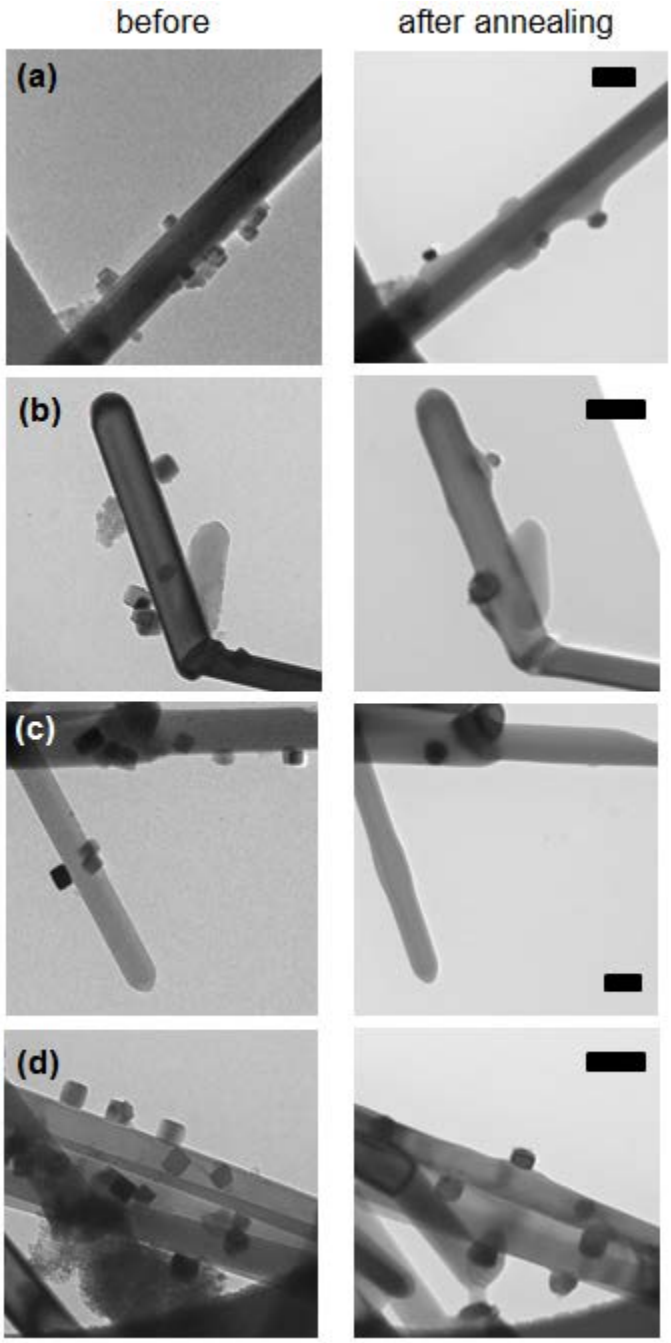

Figure 3.2. Low-resolution TEM of several *ex situ* annealing experiments. Nanoparticle-nanowire interfaces are shown before and after heating at 785 °C in Ar for 30 seconds. Scale bars are all 100 nm.

In some places where there had been a group of several particles, the particles have coalesced to form a single particle (Figure 3.2a). Some particles appear to have fused with the nanowire (Figure 3.2b); in these cases, the nanowire has swollen at the points of particle attachment, and the particles themselves have changed shape and size. In other cases, the particles have disappeared during the annealing process, and the nanowire has swollen where the particles had

been previously attached (Figure 3.2c). Similar particles along the same nanowire can undergo different transformations (Figure 3.2d), and it is not clear from these results what determines the fate of any particular nanoparticle.

3.3 Structure determination of a CoO/TiO_2 interface

One nanowire-nanoparticle (NW-NP) interface was chosen for imaging by high-resolution TEM. The elemental composition of the system was also mapped by electron energy loss spectroscopy (EELS) in STEM mode. The EELS line scan traversed the radial dimension of the nanowire and into the nanoparticle. Two energy windows of the spectra were analyzed in order to quantify the signal intensity from each of the two metals present: Ti $L_{2,3}$ signal was observed near the 475 eV region, and Co $L_{2,3}$ signal was observed in the region near 800 eV. Exact energy values for these peaks differ from those found here due to imperfect calibration of the zero-loss peak, but they are found to be within 10-20 eV of the reference values for these metals.[17] Each peak was background subtracted and integrated. Plots of the integrated signal intensity from the EELS line scan for both Ti and Co are shown in Figure 3.3. It is apparent from these data that the nanoparticle remains Co-rich after annealing, while the nanowire is increasingly doped with Co as the line scan proceeds toward the nanoparticle. Therefore, we conclude that bulging portion of the nanowire, where the surface was smooth before annealing, represents the growth of the rutile phase and incorporation of Co ions by mass transfer from the nanoparticle.

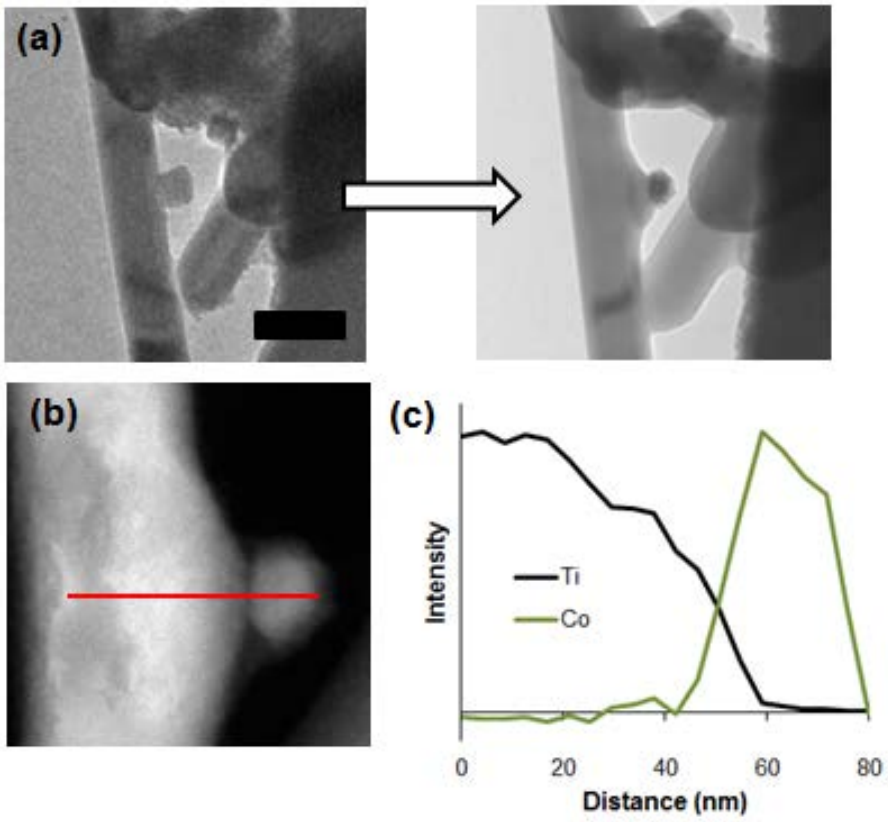

Figure 3.3. (a) Low-resolution TEM of a TiO_2 nanowire interfaced with a cobalt oxide nanoparticle, shown before and after *ex situ* heating at 785 °C in Ar for 30 seconds. Scale bar 100 nm. (b) The same interface in STEM imaging mode, where the red line indicates the path of the EELS line scan. (c) Results of the EELS line scan, where intensity is the normalized integral of the signal intensity in the region of the Ti $L_{2,3}$ region (black line) and the Co $L_{2,3}$ region (green line). EELS spectra were background subtracted before integration.

Further evidence for the diffusion of Co into the nanowire comes from HRTEM imaging of the interface itself, depicted in Figure 3.4. We rotated the nanowire/nanoparticle system in TEM so that they are both simultaneously aligned to a particular zone axis. Because the nanowire lies flat on the grid, and because the growth axis for the nanowire is known to be [001], all of the angles within the possible range of tilt motion of the TEM stage are expected to be near (i.e. within 10° of) the [100] zone axis. The atomic contrast pattern appears to be roughly hexagonal in the body of the nanowire near the interface, where the measured lattice parameters range between 2.3 and 2.5 Å by Fast Fourier transform (FFT) of the TEM images. This pattern is identified as rutile TiO_2 with a viewing axis of [100]. The assignment is corroborated by the fact that nanowire points along the [001] direction, as expected.

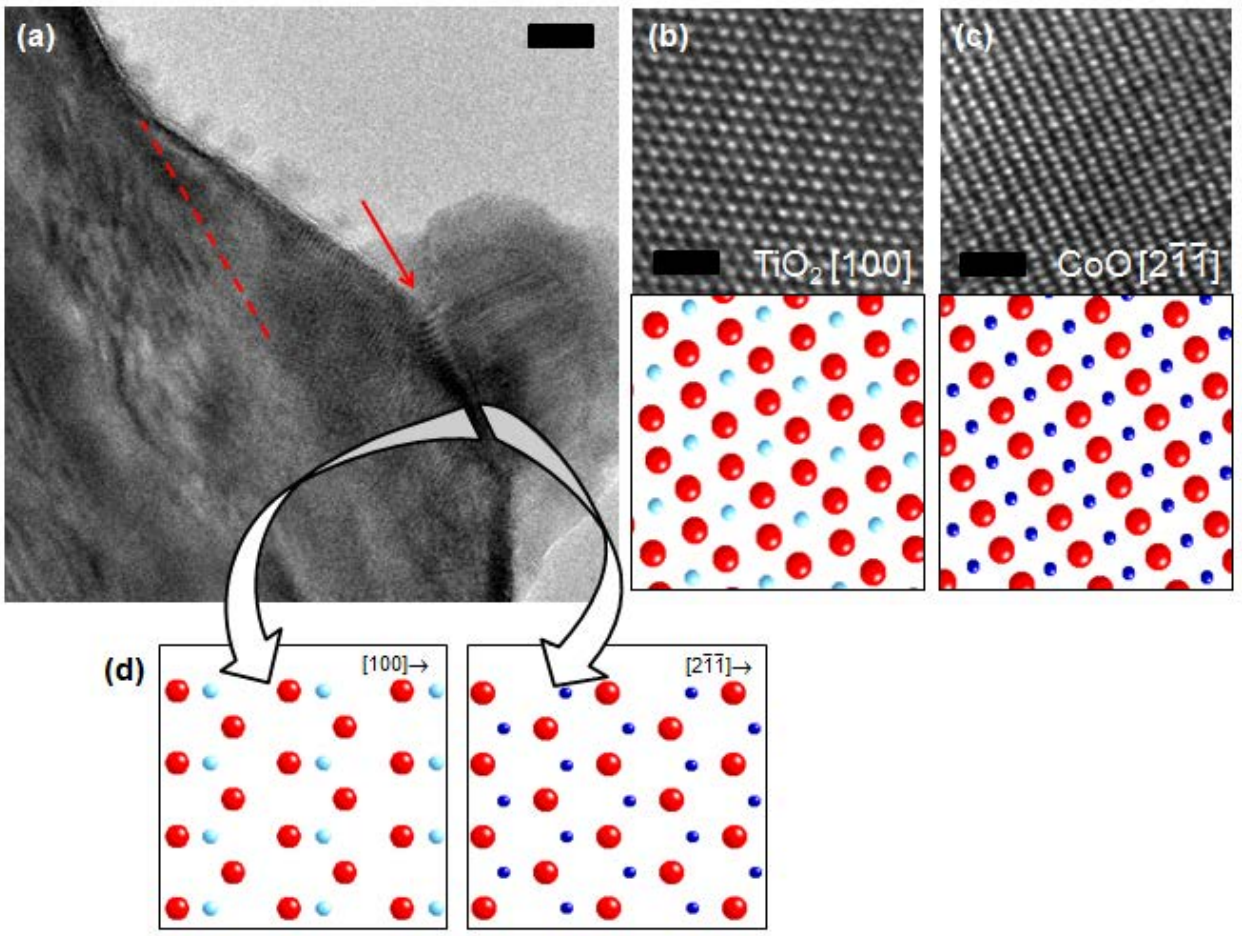

Figure 3.4. The same NW-NP interface from Figure 3.3 is shown here by HRTEM. (a) The red arrow indicates the location of the nanoparticle-nanowire interface, and the red dashed line is

shown to demonstrate that the interface and the nanowire growth axis are parallel. Higher magnification TEM is shown of (b) the nanowire and (c) the nanoparticle. Both images were taken near the interface. Crystal structure models for (b) CoO and (c) rutile TiO_2 viewed along the assigned zone axis are also shown for comparison. The atoms depicted are oxygen (red), titanium (light blue), and cobalt (dark blue). Structure models are depicted at 4x magnification. Scale bars are (a) 10 nm, (b) and (c) 1 nm. Slices from the [100] surface of TiO_2 and the $[2\bar{1}\bar{1}]$ surface of CoO are shown in (d) to demonstrate similarity between the oxygen sublattices.

Meanwhile, a rectangular pattern of contrast appears in the nanoparticle. FFT of these images yields spacings of ~2.5 Å and ~1.5 Å. This pattern is assigned to CoO with a viewing angle of $[2\bar{1}\bar{1}]$; CoO has a rock salt structure with a = 4.26 Å.[18] The change in crystal structure of the cobalt oxide from Co_3O_4 to CoO indicates that the Co^{3+} ions in the mixed oxide were reduced during the high temperature anneal in an Ar environment, as would be expected from the phase diagram of Co content vs. oxygen presence.[18]

The interface itself appears as a dark border parallel to the [001] growth axis of the nanowire; using this information, we attempt to identify the interfacial plane. If the interface is in fact a plane lying parallel to the viewing angles labeled in Figure 3.4, then we only need to find a plane that contains the vectors for both the viewing angle and the crystallographic direction of the dark border; this is done by calculating the cross-product of the two vectors—the interface plane will be normal to the resulting vector.

For TiO_2, the plane that contains both [001] and [100] is (010). This result is expected based on the rectangular cross-section of the nanowires; since the TiO_2 is bounded by four {100} facets, these are the most likely surface for particle attachment. For CoO, we assign the direction of the interface to be $[02\bar{2}]$ based on the atomic spacing, and the plane that contains both $[02\bar{2}]$ and $[2\bar{1}\bar{1}]$ is (111). Therefore, the NW-NP interface formed in this instance is CoO(111)/TiO_2(010). Without a systematic study of additional interfaces, we cannot know if this identity is shared by each interface in the annealed NW-NP system, but it is apparent that this particular interface forms a stable atomic configuration.

Slices of the two crystals in the plane of the interface are shown in Figure 3.4d. The two models are oriented here as they would be in the interface itself, with the viewing angle of the TEM images parallel. This orientation allows us to compare the geometry of the oxygen atoms in each slice and evaluate the likelihood of these two surfaces forming an epitaxial interface. In the (111) slice of CoO, oxygen atoms form a hexagonal 2D lattice with an O-O distance of 3.0 Å. Meanwhile, the oxygen atoms in the (010) slice of TiO_2 are slightly offset from each other rather than being co-located in a single plane. The projection of the oxygen atoms onto the (010) surface forms a rhombic 2D lattice, with O-O distances of 2.7 and 3.0 Å. The angles between the rhombohedral lattice vectors are 122.7° and 114.6° in this case, as opposed to 120° in the hexagonal lattice.

The visual comparison in Figure 3.4d between the two oxygen sublattices demonstrates that they are compatible, though is obvious from the 2D lattice parameters that there will be some strain at the CoO/TiO_2 interface. Of course, diffusion is possible even between two oxide crystals that

have no epitaxial relationship, but we expect that diffusion is expedited when the anion sublattice is retained across the phase boundary.[19]

3.4 Metal salt coating of nanowires for local conversion

In the previous section, pre-made nanoparticles were used successfully as a source of metal ions on the surface of the TiO_2 in order to produce a solid-state reaction at the interface. However, only certain nanowire regions were found with suitable NW-NP interfaces by this approach. When a solution of nanowires and nanoparticles were mixed, even when they were both hydrophilic as in the case of the Co_3O_4/TiO_2 mixture, a majority of the solid is found to be aggregated during mixing and drying. This prevents the study of a well-defined nanoscale conversion from TiO_2 to $CoTiO_3$. On the other hand, formation of nanoparticles directly on the nanowire surface is a promising route to a uniform coating, without excess uncoated TiO_2 or unreacted Co_3O_4.

Coating nanowires with metal salts and then annealing at intermediate temperatures in air produces a uniform metal oxide particle coating around the nanowires. This approach is shown schematically in Figure 3.5, and TEM images of the different stages are shown in Figure 3.6. First, a Co^{2+} salt was used to produce a uniform coating on TiO_2. Mixing TiO_2 nanowires with $Co(NO_3)_2$ (aq) and then quickly vacuum filtering the solution and drying the solid product produces a pink powder. Most nanowires from this powder observed by TEM are evenly coated with a salt layer, which roughens the nanowire surface. The use of vacuum filtration is important for obtaining a uniform film; gravity filtration will lead to spatially non-uniform drying patterns of the salt solution.

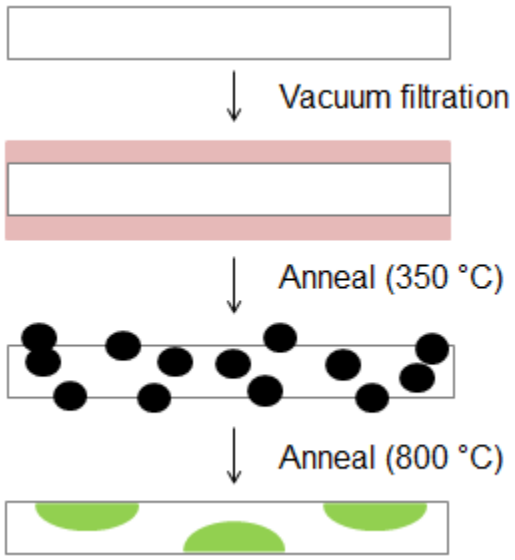

Figure 3.5. A schematic depicting the steps involved in coating a TiO_2 nanowire with pockets of $MTiO_3$. The nanowires are dispersed in aqueous salt solution, such as $Co(NO_3)_2$, and vacuum filtered, after which each nanowire is coated in a thin film of solid $Co(NO_3)_2$ (shown in pink

above). This film oxidizes when annealed in air to form nanoparticles of Co_3O_4 (black). When the nanowire-nanoparticle system is annealed to higher temperatures in Ar, Co diffuses into the nanowire and forms pockets of $CoTiO_3$ (green).

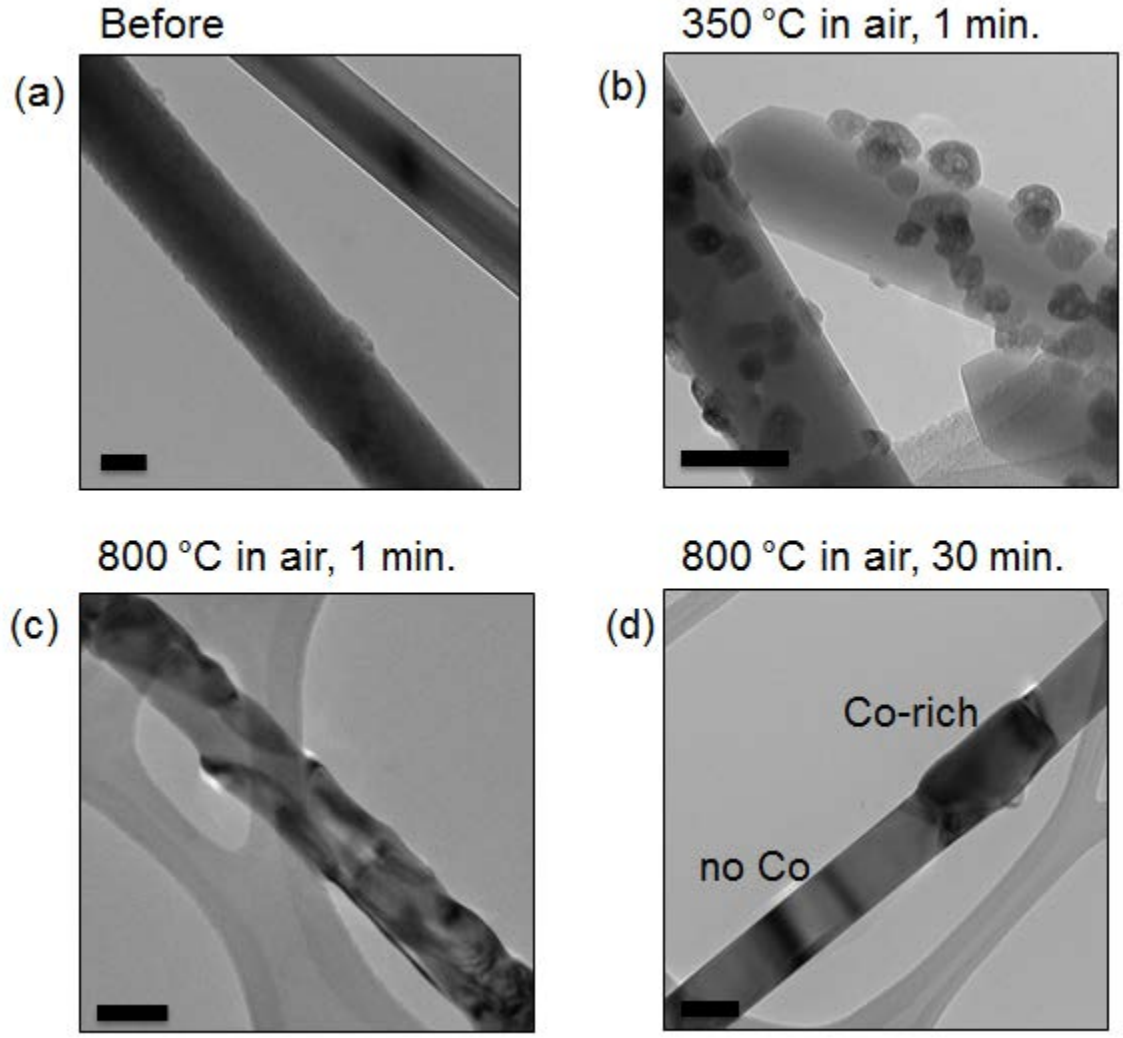

Figure 3.6. TEM images of the stages of Co_3O_4 particle formation on the TiO_2 nanowire surface and subsequent conversion to $CoTiO_3$. Scale bars are all 100 nm.

When the $Co(NO_3)_2$-coated TiO_2 is annealed in air at 350 °C, the powder becomes dark gray or black. By TEM, we see that the cobalt has coalesced on the nanowire surface to form particles roughly 20-50 nm in diameter, and by XRD we learn that these particles are Co_3O_4. The particles have poorly-defined shapes, and they appear to be porous or partially hollow. Particle size is controllable by the cobalt concentration in solution before filtration; a higher concentration of Co^{2+} relative to TiO_2 nanowires in solution leads to thicker salt coatings and larger oxide particles.

A subsequent anneal at 800°C for 30 minutes in air produces a green powder. Based on XRD results, this powder is composed entirely of TiO_2 and $CoTiO_3$, which is the source of the green

color. By TEM, we see that the nanowire has been converted into alternating segments of rutile and $CoTiO_3$. Energy-dispersive x-ray spectroscopy (EDS) results indicate that segments with darker contrast are Co-rich, e.g. the top segment in Figure 3.6d has a Ti:Co ratio of 1.0:0.7. A shorter anneal was done in the same conditions for just 1 minute, shown in Figure 3.6c. Here we find that conversion is limited to pockets on the nanowire surface, as originally intended. For the nanowire in Figure 3.6c, the Ti:Co ratio by EDS was 2.9:1.0.

In an attempt to observe local conversion to $CoTiO_3$ *in situ*, a sample of Co_3O_4-coated TiO_2 produced by the method above was loaded onto a heating stage in a Philips CM200 TEM at 200 kV. The particles on a particle pair of nanowires were tracked while heating the stage from room temperature to nominally >900 °C. Unfortunately, the particles do not appear to have initiated conversion of the TiO_2. A possible reason for this result include the effect of vacuum inside the TEM chamber, as opposed to the air environment present during previous anneals. Additionally, thermal conduction across the TEM grid may not have been sufficient to heat the nanowires to the temperature measured by the heating stage's thermocouple, as the nanowires are suspended over vacuum from a Si_3N_4 membrane. Nonetheless, this experiment provided the opportunity to observe particles changing shape and migrating freely along the surface of the nanowire, as shown in Figure 3.7.

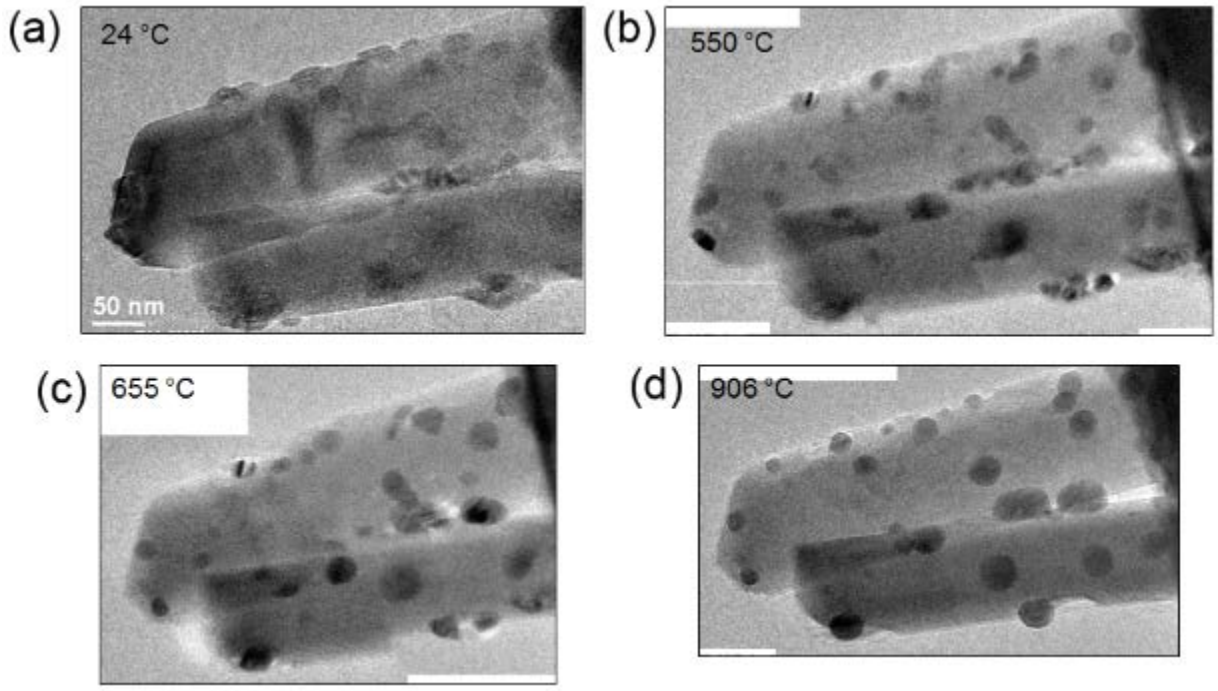

Figure 3.7. An *in situ* heating experiment on a TiO_2 nanowire that had been coated in $Co(NO_3)_2$ and then annealed at 350 °C to form particles of Co_3O_4. Temperature of the heating stage increases from (a) through (d). Local temperature at the nanowire may differ from the value measured at the thermocouple.

3.5 Structure determination of $NiTiO_3/TiO_2$ interfaces

Chemical bath deposition (CBD) is a general process wherein a solid substrate nucleates the heterogenous growth of another solid from solution species. We use it here as an alternative method for producing uniform coatings of transition metal oxides on TiO_2. A sample of TiO_2 nanowires were coated in Ni by CBD from a solution of $Ni(NO_3)_2$ and urea.[20] The CBD method resulted in sheets of $Ni(OH)_2$ wrapped around the nanowire. These coated nanowires were annealed at 900 °C in an Ar environment, producing composite nanowires: both $NiTiO_3$ and rutile TiO_2 appear in the XRD pattern.[20] Nanowires from this sample were dropcast on a lacey carbon membrane and imaged by TEM and STEM (Figure 3.8). Certain segments of the nanowire have converted to a different phase after annealing, based on the sharp lines between areas of different contrast. To characterize these phases and the interfaces between them, we analyze the data from EELS and high-resolution imaging.

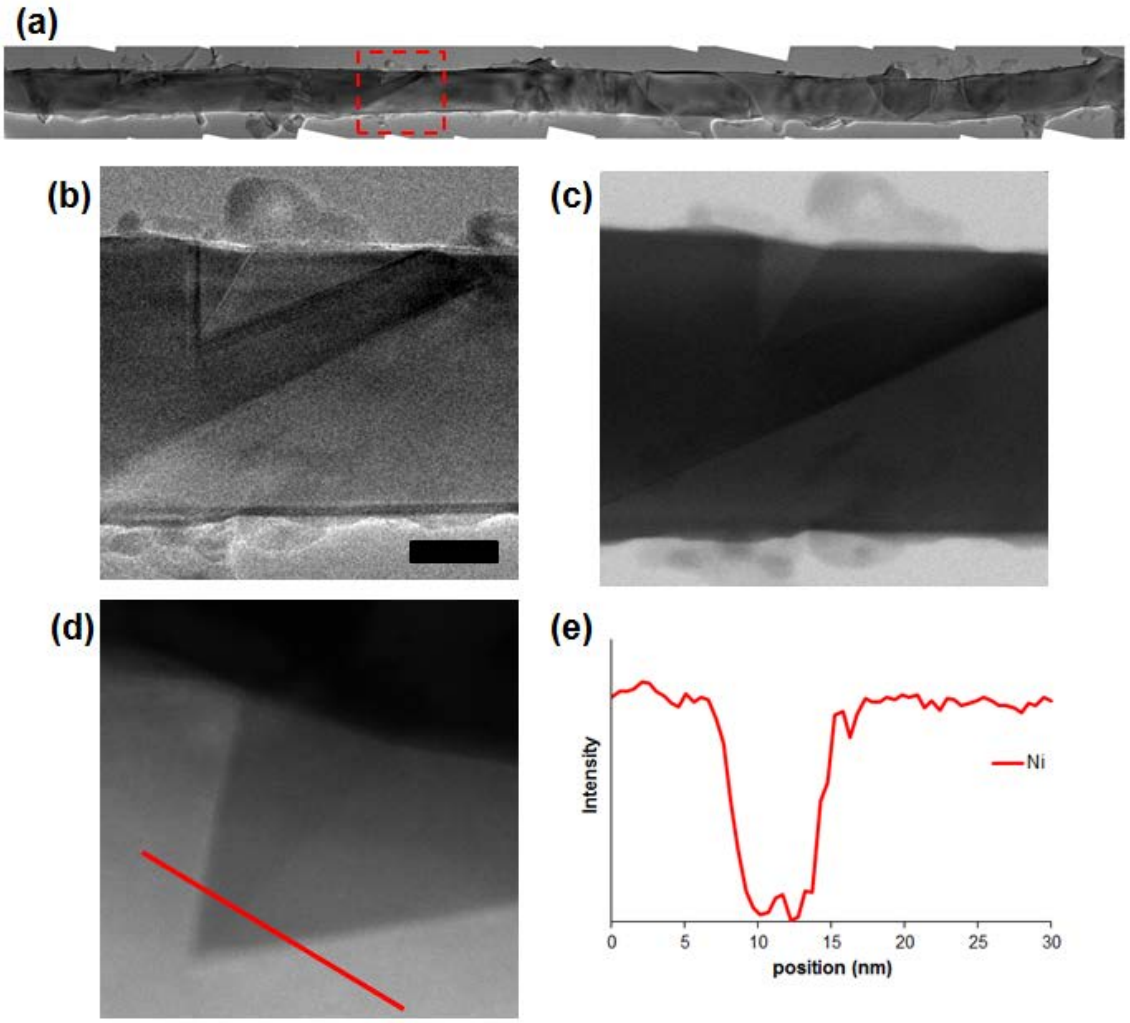

Figure 3.8. (a) A composite image of a TiO_2/Ni nanowire after annealing. The image is constructed by blending 14 separate TEM images of overlapping regions along the body of a nanowire. The area in the dashed red line is the enlarged region in parts b-e. (b) Low-resolution TEM of a set of interfaces found in the nanowire. Scale bar is 20 nm. (c) Bright-field STEM of the same region. (d) Dark-field STEM of the same region. The red line indicates the path of the

EELS line scan. (e) Results of the EELS line scan, where intensity is the normalized integral of the signal intensity in the region of the Ni $L_{2,3}$ region. EELS spectra were background subtracted before integration.

An EELS line scan was performed in STEM mode across a particular region of the nanowire, which contains 3 interfaces. The line scan crossed these interfaces such that the electron beam traveled from an area of bright contrast to a darker area and back again to bright contrast. Each spectrum was background subtracted and integrated over the Ni $L_{2,3}$ peak near 875 eV, and the resulting line scan data are plotted in Figure 3.8e. Drift in the sample prevents precise determination of the location on the nanowire where the Ni signal disappears and reappears in the spectrum, so we look to other evidence of which regions have Ni present. Because these STEM data were collected by a high-angle annular dark field (HAADF) detector, contrast is proportional to the atomic number (Z) of the atoms in the material.[21] Ni is a heavier atom than Ti (atomic number 28 vs. 22), so one would expect the Ni-rich region of the nanowire to appear brighter, and indeed, we see a dip in the Ni content to nearly zero across the region of darker contrast. Therefore, based on the EELS analysis, each segment of the nanowire can be easily identified as either TiO_2 or $NiTiO_3$.

A more complete understanding of the relative orientation of the two phases required HRTEM. The nanowire was rotated and aligned to a zone axis. The FFT patterns of the atomic contrast seen on either side of the interfaces were indexed and assigned to a particular crystal structure. For example, in Figure 3.9d, the top-left portion of the image produces a hexagonal FFT pattern, with six spots at 2.5 Å and 60° rotation from each other, which matches the [001] zone axis of $NiTiO_3$. The bottom-right portion of the image produces a rhombohedral FFT pattern, with four spots at 2.5 Å and 2 spots at 2.3 Å. The angles separating these spots are 57° and 66°, so we assign this pattern to the [100] zone axis of TiO_2. The same procedure was followed for images of the other interfaces, and the resulting assignments are depicted in Figure 3.9.

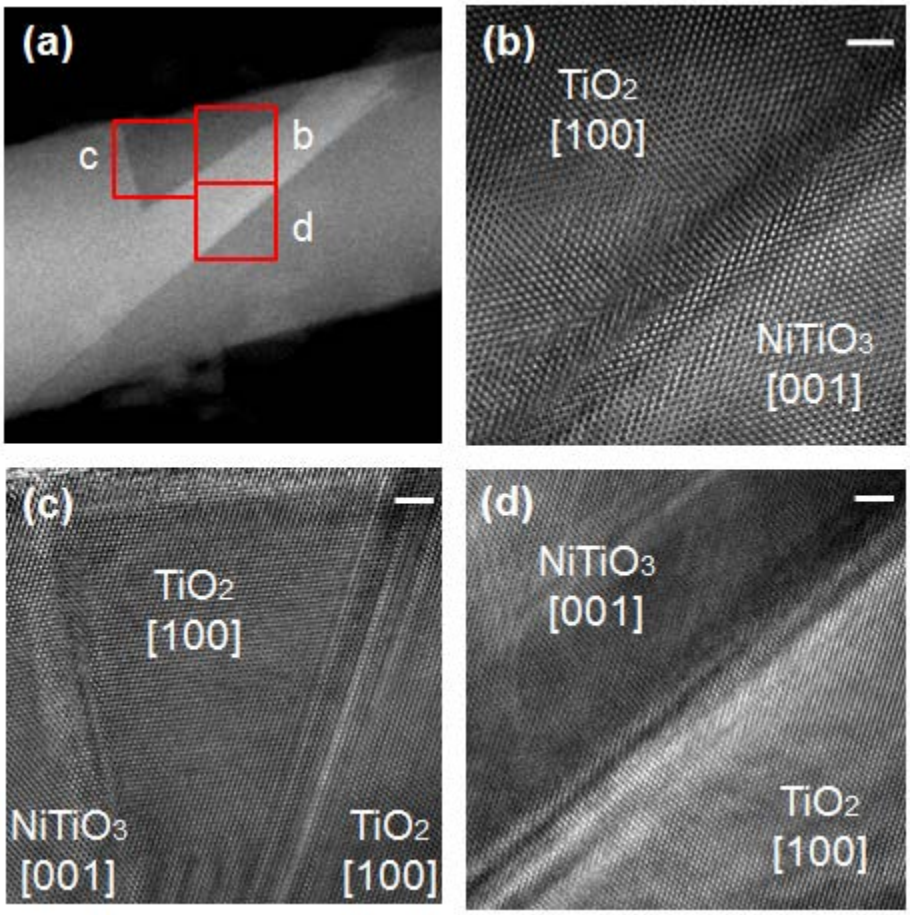

Figure 3.9. (a) Dark-field STEM of the nanowire region analyzed in Figure 3.8. (b-d) High-resolution TEM of the various interfaces in the region, along with the crystallographic assignments based on FFT of the atomic contrast. The labeled lattice directions are the viewing axes for each region. See Table 3.1 and Figure 3.11 for more detailed identification of the interfaces. Scale bars are 2 nm.

Along the length of the nanowire, three distinct types of interfaces are observed. Using evidence from both EELS and low-resolution TEM, we may categorize them based on angle and bounding material. First is an interface between TiO_2 and $NiTiO_3$ that lies perpendicular to the nanowire surface, which we call Type A. Second, there is another TiO_2/$NiTiO_3$ interface, but this one is oblique to the nanowire surface with an angle less than 45° (Type B). And finally, an interface between two regions of is observed that is oblique but at an angle greater than 45° (Type C). Fourteen Type B interfaces along this particular nanowire were measured to be an average of 27° from the nanowire surface based on low-resolution TEM, while ten interfaces of Type C gave an average of 59°. Thirteen Type A interfaces were also recorded at approximately 90°. The limitation of low-resolution TEM for this analysis is that the angles are measured relative to the annealed nanowire surface, which itself has quite a bit of texture and local curvature.

We learn from HRTEM that Type A and Type C interfaces are boundaries between $NiTiO_3$ and TiO_2, and Type B interfaces two areas of TiO_2. These three interfaces can be arranged in several

different configurations, aside from the one shown in Figures 3.8 and 3.9. Two additional structures which are repeatedly observed in the composite nanowires are shown in Figure 3.10, and the phases are labeled based on the above HRTEM analysis.

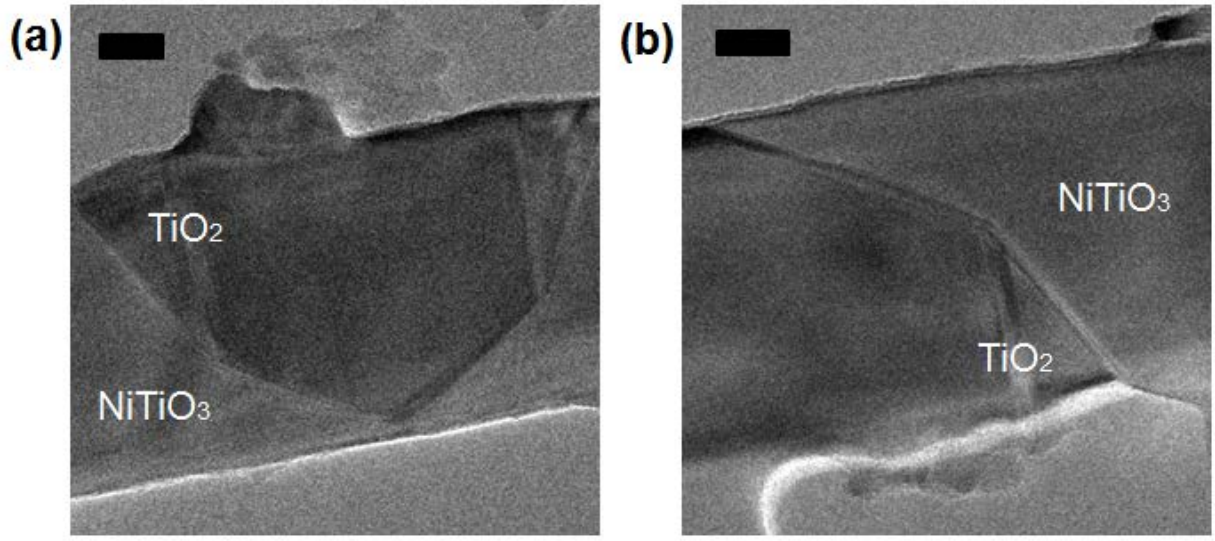

Figure 3.10. TEM of two additional types of interfaces observed in segmented $NiTiO_3/TiO_2$ nanowires.

To learn more about the nature of these three interfaces, we assume that the interfaces shown in Figure 3.9 are representative of their particular type and we investigate their atomic structure. First, based on the sharp transition in STEM contrast, we may assume that these interfaces all lie parallel to the zone axis used for imaging. Then, we are able to obtain a crystallographic assignment for all three types by recognizing that the interfacial plane must contain two vectors: 1) the zone axis from TEM and 2) the direction of the line representing the interface (i.e. the line formed when the interface is projected onto the imaging plane).

When calculating the vector cross-product, it is important to note that the ilmenite $NiTiO_3$ structure has a rhombohedral lattice, therefore its lattice directions are not orthogonal; it is conventionally described in terms of a hexagonal unit cell. We choose to use the three-index Miller notation for simplicity to refer to the ilmenite lattice directions and planes, even with the downside that the vector [hkl] is not necessarily orthogonal to the plane (hkl), e.g. (100) is orthogonal to [210] in $NiTiO_3$. Neglecting this fact will lead to an incorrectly assigned plane, because the cross-product of vectors 1 and 2 will not have the same index as the orthogonal plane.

Using the interfaces shown in Figure 3.9b and 3.9d, the Type C interface is identified by this method as $NiTiO_3(100)/TiO_2(03\bar{1})$. The vector normal to $(03\bar{1})$ forms an angle of 27.4° with the [001] growth direction of TiO_2, which is a good match for our average measurement of 27°. This result is corroborated by the natural occurrence of $FeTiO_3(010)/TiO_2(301)$ boundaries in mineral samples of rutile interspersed with ilmenite.[22] The Type B interface, shown on the right side of Figure 3.9c, is a $(01\bar{1})$ twin plane of TiO_2; it is identified as a twin plane because the TiO_2

crystals are reflected across either side of the boundary. The angle between this plane and the nanowire growth direction is 57.2°, differing only slightly from our average measurement of 59°.

One effect of the reflection across the twin plane in the Type B interface is that the axial direction of the nanowire is no longer [001] inside the central region of Figure 3.9c. In fact, the axial direction is now normal to $(03\bar{1})$, so we identify the Type A interface as $NiTiO_3(010)/TiO_2(03\bar{1})$. And finally, we recognize that the (010) and (100) directions of $NiTiO_3$ are identical by symmetry, so Types A and C are both $NiTiO_3\{100\}/TiO_2\{03\bar{1}\}$ interfaces, where curly brackets denote a family of equivalent planes. These results are summarized shown in Table 3.1, which identifies the angle of each interface and the material planes on either side, based on the characterization above.

Interface	Measured angle vs. nanowire surface	Identity
A	90°	$NiTiO_3(010)/TiO_2(03\bar{1})$
B	~59°	$TiO_2(01\bar{1})$ twin plane
C	~27°	$NiTiO_3(100)/TiO_2(03\bar{1})$

Table 3.1. Types of interfaces observed in the $TiO_2/NiTiO_3$ nanowire, and their measured angles and crystallographic assignments.

Though the crystal structures of ilmenite $NiTiO_3$ and rutile TiO_2 are very different, they are able to match up favorably inside the annealed nanowire as described above. To confirm that this configuration is feasible in terms of the oxygen sublattice, a comparison similar to the one in Figure 3.4d was completed again here. A model of each crystal was sliced along the interfacial planes. For both Type A and Type C interfaces, the oxygen atoms on the two surfaces appear to have a very similar layout, as shown by the modeled planar slices in Figure 3.11. The orientation of the slices are matched by making the viewing axes identified by TEM parallel in each model, e.g. the z axis for $NiTiO_3$ and the x axis for TiO_2. The oxygen sublattices are both fairly complex, due to the large unit cell for $NiTiO_3$ and the high index plane for TiO_2. It is apparent from the normal view and the side-on rotated views in Figure 3.11 that the oxygen placement in these slices is similar, though not identical.

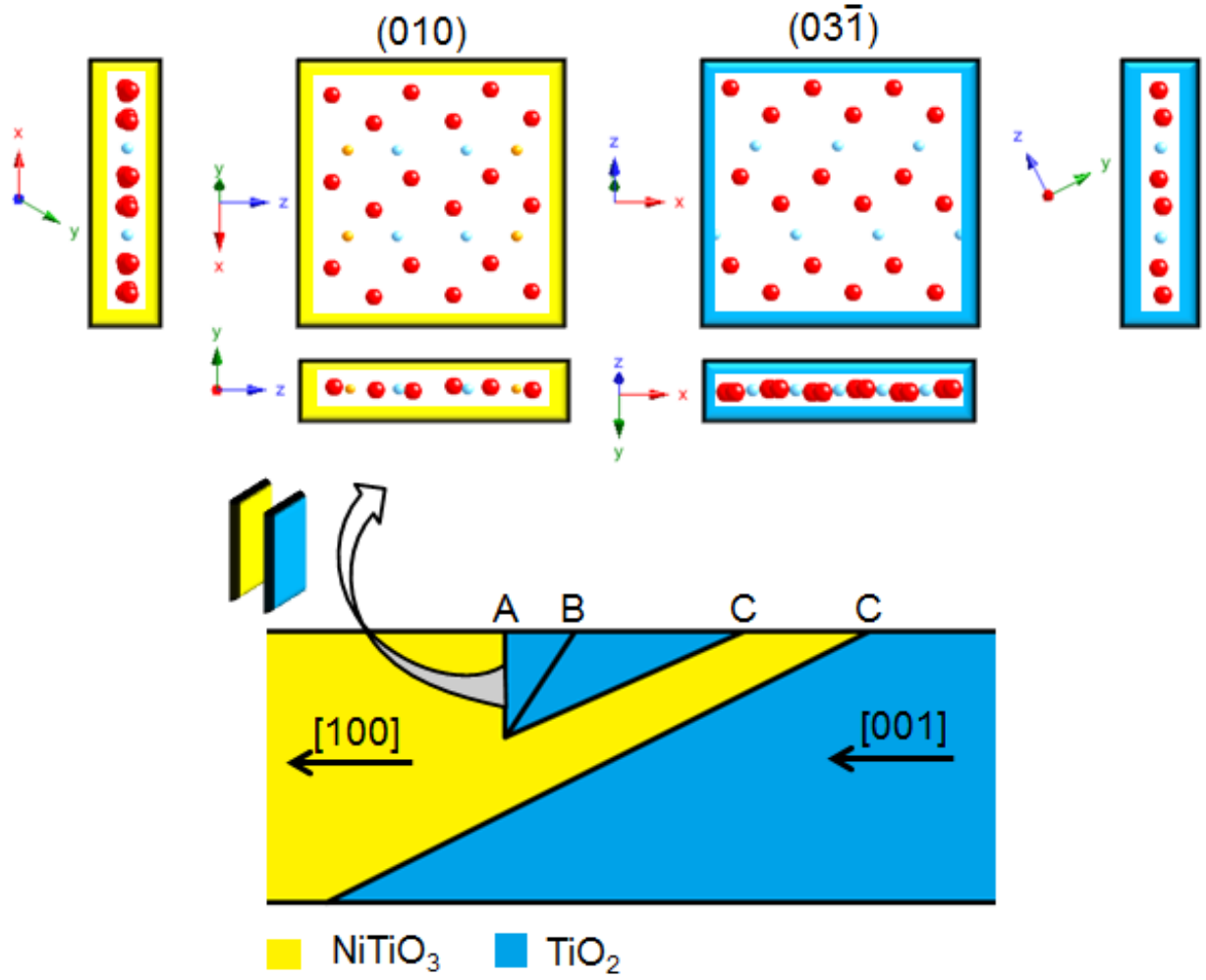

Figure 3.11. A schematic showing the atomic surfaces of TiO_2 and $NiTiO_3$ at one of the interfaces found in the segmented nanowire. Type A and C are both $NiTiO_3\{100\}/TiO_2\{03\bar{1}\}$ interfaces, and Type B is a TiO_2 $(01\bar{1})$ twin plane. The atoms depicted are oxygen (red), titanium (blue), and nickel (yellow). Alternate viewing angles for the (100) slice of $NiTiO_3$ are [100] (bottom) and [001] (left). For the $(03\bar{1})$ slice of TiO_2, viewing angles shown are [013] (bottom) and [100] (right).

The assignment of planes for these interfaces gives us some insight into the strain present in the nanowire lattice. The angle of the Type C interface is 27.4° relative to the TiO_2 growth direction, but the angle of the same interface relative to the [100] direction in $NiTiO_3$ is 30.0°. This deviation likely leads to small bends in an otherwise straight nanowire, as observed in Figure 3.8a. This study does not directly provide mechanistic information about the diffusion of Ni into the TiO_2 lattice, but it lays the foundation for any future mechanistic study of this system by describing in detail the end product of the segmented composite nanowire.

References

(1) Agui, A.; Mizumaki, M. *J. Electron Spectros. Relat. Phenomena* **2011**, *184*, 463–467.
(2) De Haart, L.; De Vries, A.; Blasse, G. *Mater. Res. Bull.* **1984**, *19*, 817–824.
(3) Bin-Daar, G.; Dare-Edwards, M. P.; Goodenough, J. B.; Hamnett, A. *J. Chem. Soc. Faraday Trans. 1 Phys. Chem. Condens. Phases* **1983**, *79*, 1199.
(4) Salvador, P.; Gutierrez, C.; Goodenough, J. *J. Appl. Phys.* **1982**, *53*, 7003–7013.
(5) Blasse, G. In *Complex Chemistry*; Springer, 1991; pp. 153–187.
(6) Suntivich, J.; May, K. J.; Gasteiger, H. A.; Goodenough, J. B.; Shao-Horn, Y. *Science* **2011**, *334*, 1383–1385.
(7) Man, I. C.; Su, H.-Y.; Calle-Vallejo, F.; Hansen, H. A.; Martínez, J. I.; Inoglu, N. G.; Kitchin, J.; Jaramillo, T. F.; Nørskov, J. K.; Rossmeisl, J. *ChemCatChem* **2011**, *3*, 1159–1165.
(8) Rossmeisl, J.; Logadottir, A.; Nørskov, J. K. *Chem. Phys.* **2005**, *319*, 178–184.
(9) Rossmeisl, J.; Qu, Z.-W.; Zhu, H.; Kroes, G.-J.; Nørskov, J. K. *J. Electroanal. Chem.* **2007**, *607*, 83–89.
(10) García-Mota, M.; Vojvodic, A.; Metiu, H.; Man, I. C.; Su, H.-Y.; Rossmeisl, J.; Nørskov, J. K. *ChemCatChem* **2011**, *3*, 1607–1611.
(11) Liu, B.; Chen, H. M.; Liu, C.; Andrews, S. C.; Hahn, C.; Yang, P. **2013**, 8–11.
(12) Yin, M.; O'Brien, S. *J. Am. Chem. Soc.* **2003**, *125*, 10180–10181.
(13) Ould-Ely, T.; Prieto-Centurion, D.; Kumar, A.; Guo, W.; Knowles, W. V.; Asokan, S.; Wong, M. S.; Rusakova, I.; Lüttge, A.; Whitmire, K. H. *Chem. Mater.* **2006**, *18*, 1821–1829.
(14) Feng, J.; Zeng, H. C. *Chem. Mater.* **2003**, *15*, 2829–2835.
(15) Xu, R.; Zeng, H. C. *Langmuir* **2004**, *20*, 9780–9790.
(16) Yankin, A. *Inorg. Mater.* **2002**, *38*, 309–319.
(17) Fuggle, J.; Mårtensson, N. *J. Electron Spectros. Relat. Phenomena* **1980**, *21*, 275–281.
(18) CoO: phase diagram, crystal structure, lattice parameters. *SpringerMaterials - The Landolt-Bornstein Database*, 2010, *41D*.
(19) Schmalzried, H. In *Defects and transport in oxides*; 1973.
(20) Moore, M. C. Metal Oxide Nanostructured Materials for Optical and Energy Applications, 2013.
(21) Nellist, P. D.; Pennycook, S. J. **2008**, *78*, 111–124.
(22) Daneu, N.; Schmid, H.; Recnik, A.; Mader, W. *Am. Mineral.* **2007**, *92*, 1789–1799.

Chapter 4

Introduction to Graphene Aerogels as High Surface-Area Materials for Electrochemical Energy Storage

4.1 Electrochemical energy storage using supercapacitors

Solar water splitting, where the energy from the sun is stored in the form of chemical bonds in H_2 molecules, is just one of many strategies for storing solar energy to be used at times or locations without sunlight. Supercapacitors, also known as ultracapacitors or electrochemical capacitors, are a class of energy storage devices. Like batteries, supercapacitors can be charged, transported, used to deliver power on-demand. They are constructed as a standard electrochemical device, with two electrically connected electrodes and an electrolyte between them. Unlike batteries, however, energy storage in supercapacitors is most often due to a physical separation of charges rather than a chemical transformation.

The most common type of supercapacitor is called an electric double layer capacitor (EDLC). A schematic of EDLC operation is depicted in Figure 4.1, and its performance depends on the capacitance (C) between solution ions and the surface of the polarized electrodes' electric double layer. The energy stored by a standard capacitor is $E = C \cdot V^2/2$, so the maximum possible energy stored in electrolyte would seem to be limited by the relatively small range of voltages tolerated by water before electrolysis occurs. But in an EDLC, the low voltage is compensated for the very large possible values of C. This phenomenon was originally discovered using porous carbon as the electrode material,[1] and activated carbon remains the most common material used in commercial ECs.

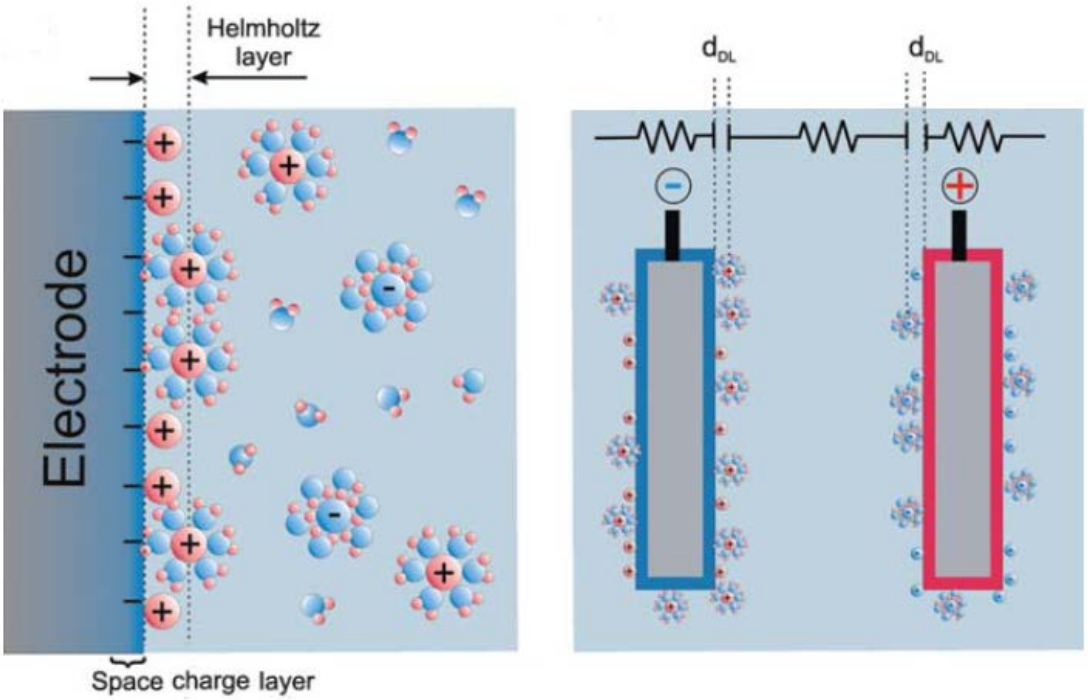

Figure 4.1. Diagram of an electric double layer (left) and the two electrodes of an EDLC (right). Adapted from Biener *et al.*[2]

One reason that porous carbons display such outstanding capacitance compared to planar metal electrodes is that the double layer occupies the entire surface area of the porous carbon-electrolyte interface. The equation for calculating C for any capacitor is $C = A \cdot \varepsilon / d$, where A is the capacitor area, which can be higher than 2000 m^2/g for some porous carbon materials, ε is the dielectric constant in the space between the charged layers, and d is the separation distance between charged layers. Another reason that EDLCs have such high capacitance is that their d value is as small as the width of the double layer itself, i.e. 1 nm or so.

Supercapacitors occupy the low energy density portion (up to 5-10 Wh/kg) of a Ragone plot comparing different methods of storing energy (shown in Figure 4.2). The power density of a supercapacitor is often higher than that of a battery, because charge can be delivered very quickly via electron and ion conduction, rather than an electrochemical reaction. EDLCs also tend to have a long device lifetime (>10^6 cycles), because charging and discharging do not require any changes to the chemical structure of the electrode. Gravimetric energy density (or specific energy), on the other hand, is low for EDLCs, because the charge can only be stored at the electrode-electrolyte interface rather than being stored inside the bulk of the electrode as in a battery. The aim of material development for EDLCs is typically to increase the energy density without sacrificing the power density. An ideal supercapacitor material should have: i) large surface area, ii) high conductivity, iii) pore size distribution to complement the ion size, iv) highly interconnected pores, and v) a wettable surface.[3,4]

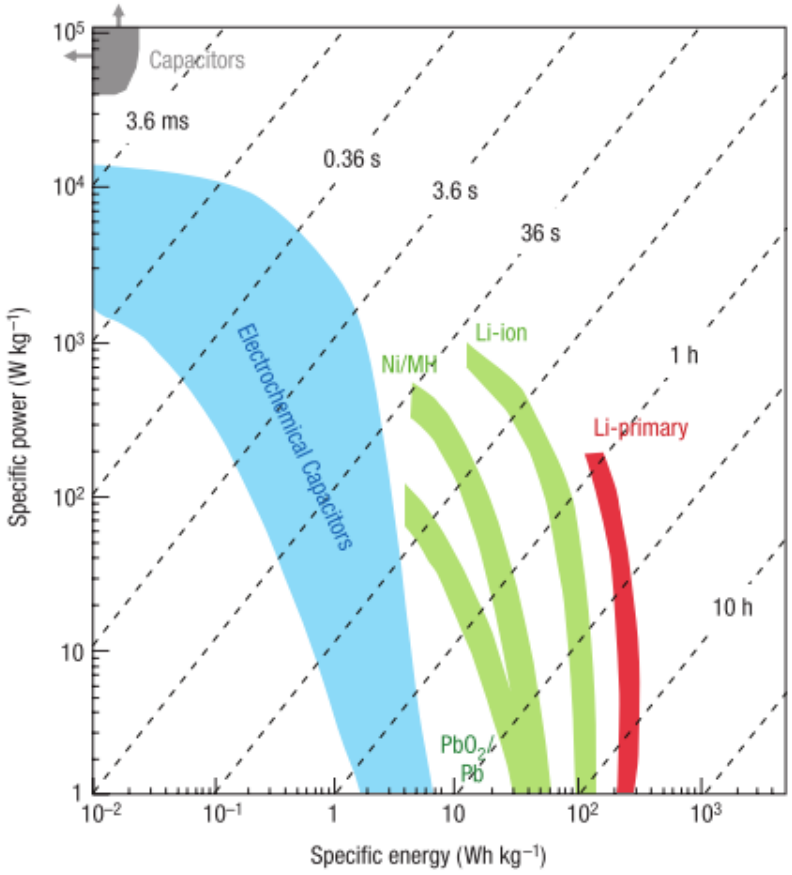

Figure 4.2. Ragone plot showing typical ranges of energy density and power density of supercapacitors, compared to different battery types and standard capacitors. The dashed diagonal lines are time constants for discharge of the device. From Simon and Gogotsi.[5]

4.2 Experimental techniques for supercapacitor characterization

A material intended for use in an EDLC must have high surface area, as explained in section 4.1, but not all surfaces are alike, and not all pores in a porous material are necessarily available to participate in charge storage. Therefore, it is useful to test both the surface area (SA) and the capacitance (C) of a material for comparison with other material candidates for EDLCs. It can be tempting to calculate energy density and power density for a particular electrode following electrochemical testing, but this should be avoided. Both energy and power density depend heavily on the mass of the packaging, i.e. elements in a commercial cell other than the electrode material itself. Additionally, care should be taken to use electrodes dimensions similar to what would be used commercially, as unrealistically thin electrode films can lead to inaccurate measurements of capacitance. Researchers interested in materials optimization should focus on improving the performance of electrodes with realistic thickness, i.e. at least several μm.

4.2.1 Surface area

By far the most common method of determining the available SA for a porous material is to perform nitrogen adsorption porosimetry. In this technique, a sample is placed in an evacuated container and immersed in liquid nitrogen. The vessel is then dosed with fixed volumes of nitrogen gas, and the resulting pressure is measured. The curve of $V_{adsorbed}$ vs. P/P_o is known as an isotherm; P/P_o is known as the relative pressure, and it varies up to 1.0, which is the saturation pressure of N_2 at 77 K, i.e. P_o = 760 mmHg. The shape of the isotherm is governed by the surface properties and porosity of the material. Example shapes that an isotherm may take, along with the IUPAC categorization of each type, are shown in Figure 4.3.

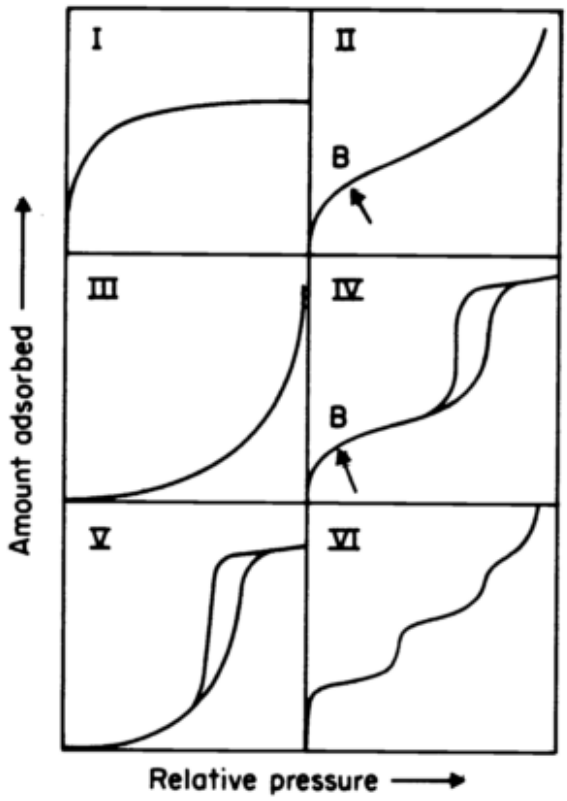

Figure 4.3. Isotherms of Types I-VI that may be obtained from porosimetry measurements. From Sing *et al*.[6]

Developed in 1938, the Brunauer-Emmett-Teller (BET) model for calculating SA of a porous material is still the most commonly reported method.[7] According to the BET model, multilayers of gas molecules are allowed to adsorb to surface sites, and the proportion that remain adsorbed at a particular pressure depends on the enthalpy of adsorption. The BET equation (Equation 4.1) illustrates how a plot of $P/n_{adsorbed}(P_o-P)$ vs. P/P_o can be used to obtain $n_{surface}$, which is the number of surface sites, or the total SA divided by the surface area occupied by a single adsorbed nitrogen molecule. The equation is expected to produce a linear fit in the region of P/P_o = 0.05-0.30.[6]

Equation 4.1

$$\frac{P}{n_{adsorbed}(P_o - P)} = \frac{1}{n_{surface} \cdot C} + \frac{(C-1) \cdot P}{n_{surface} \cdot C \cdot P_o}$$

Limitations of the BET model can be quite restrictive based on the assumptions of the model. These assumptions include: no micropores (<2 nm diameter) in the material, all surface sites are identical, all multilayers are equivalent, and so on. The simplicity of the model has led to its commonplace usage, but care should be taken not to compare SA obtained by the BET method to other SA values, such as those obtained by density functional theory (DFT) calculations on intermolecular interactions in micropores.[8]

As gas is added to the sample and multilayers form on the surface, smaller pores begin to fill completely with adsorbed nitrogen. At these intermediate relative pressures, the isotherm data can also be used to determine the diameter and volume of the pores. The classic model for calculating pore size distribution is the Barrett-Joyner-Halenda (BJH) model.[9] This analysis is less straightforward than the BET model, and the data are easily misinterpreted based on incorrect assumptions about pore shape and interconnectedness of the pore network.[10,11]

4.2.2 Gravimetric capacitance

There are two commonly used ways of determining the capacitance of an electrode, which have been reviewed by Stoller and Ruoff.[12] The first is obtained by performing a galvanostatic (constant current) charge/discharge cycle and measuring the electrode potential. The data will appear as two lines, as the capacitor is charged and then discharged linearly over time. The rate of changing voltage, i.e. the slope of the lines, is determined by the capacitance as described in Equation 4.2.

Equation 4.2

$$C = \frac{I}{dV/dt}$$

A second method is to conduct cyclic voltammetry and measure the current as a result of scanning voltage in the cell. An ideal capacitor produces a rectangular curve, so a section of the curve with constant current can be identified and then used in Equation 4.2 to calculate C. Both of these measurements should be taken in a 2-electrode symmetric device, where the active material is both the anode and the cathode, in order to calculate the true capacitance of the double layer.[12]

In order to obtain an accurate value of gravimetric (i.e. specific) capacitance, the measured value of C should be divided by the total mass of electrode material in the cell (m), and then multiplied by 4 to account for the two electrodes worth of mass and the two electric double layers formed in the experiment. If capacitance per volume is of interest instead, then Equation 4.3 is still used but m is replaced by V, the combined volume of the two electrodes.

Equation 4.3

$$C_{specific} = 4 \cdot \frac{C_{measured}}{m}$$

4.3 Carbon aerogels and GO-based aerogels

Carbon aerogels are three-dimensional porous structures with high surface area and low density, which are promising for widespread applications in addition to electrochemical energy storage, such as hydrogen storage, water desalination, fuel cell catalysis, and oil adsorption for environmental remediation.[2,13] The original aerogels were made from silanes, which can be both acid- and base-catalyzed to form hydrogels at 60 °C.[14] Hydrogels are self-supporting structures with solvent-filled pores. These pores can be evacuated by supercritical drying with liquid CO_2. In this process, a vessel containing the hydrogel is i) pressurized in order to exchange the solvent for CO_2, ii) heated so that the fluid becomes supercritical, and iii) vented so that the CO_2 is replaced with air. This allows evacuation of the pores without any surface tension that would be associated with solvent evaporation, which would collapse the pores and decrease the available surface area.

Carbon aerogels with similar properties to the silica forerunners were first made at Lawrence Livermore National Laboratory in 1989.[15] These gels were constructed from resorcinol and formaldehyde monomers to form polymer networks in a basic environment. The hydrocarbon backbone of a resorcinol-formaldehyde (RF) gel is generally unstable in air at high temperatures. For this reason, gels are typically fired in an inert atmosphere to prevent oxidation; after pyrolysis, the carbon is largely amorphous with small graphitic domains.[2] RF gels have a dark red color until they are fired to become black carbon aerogels.[15–17]

Silica aerogels are non-conducting, which prevents their use in many other applications, and carbon aerogels formed from pyrolysis of an RF gel have limited conductivity due to their amorphous structure. Graphene-based aerogels, on the other hand, are composed of single or few-layer graphene sheets. This imparts extraordinary graphene-like properties to the aerogel, such as high electrical conductivity.[18,19] Porous graphene has also gotten attention for its possible use in water remediation[20] and gas sensing.[21] The aerogel structure serves to amplify the remarkable properties of graphene by increasing the available surface area in any device by many orders of magnitude, compared to a single sheet of atoms with the same geometric footprint.

The most common synthetic method for constructing graphene-based aerogels is a sol-gel reaction, in which a solution of graphene oxide (GO) sheets is induced to form a solid network within a liquid phase. The liquid phase is then removed by critical-point drying, followed by thermal annealing. This method produces aerogels on the order of 10 mg/cm^3,[19] whereas simply allowing the solvent to evaporate yields a material with as high as 1g/cm^3.[22] Carbon nanotubes have also been incorporated into aerogels, either alone or in conjunction with GO.[13,23]

Because the aerogels are constructed from oxidized graphene and can be chemically quite dissimilar to graphene, we choose here to call them “GO-based aerogels.” Many different techniques have been investigated for modifying the synthesis of GO-based aerogels,[24–31] a few

of which we briefly describe here. Wu *et al.* introduced additional porosity by adding a mesoporous SiO_2 layer to the macropore walls of a GO-based aerogel and then coating the mesopores in carbon.[24] Qiu *et al.* showed that freeze-casting GO sheets creates very low-density gels, due to the macropores formed by expanding ice crystals.[25] Zhu *et al.* used a treatment of microwave radiation and KOH treatment to produce high surface area gels with nanometer size pores.[26]

Sol-gel chemistry has been thoroughly investigated for silica and RF gels, as well as for a range of inorganic systems such as metal oxides and chalcogenides.[32,33] Some researchers have examined how various small molecules, polymers, and ions can act as cross-linkers in GO hydrogels,[34] and other have investigated the effect of pH on GO-based gels.[35] However, in general, the sol-gel chemistry of pure GO systems remains relatively unexplored. We attempt to address this deficiency in the next chapter.

4.4 Application of aerogels in supercapacitor devices

Graphene oxide, which is made from chemical oxidation of graphite, is a versatile material; it is synthetically useful for its ability to be dispersed in water, where it can take part in the sol-gel reaction to form a hydrogel. In order to serve as an electrode in an EDLC, however, an aerogel made from GO should be reduced to return to a more graphitic state. Chemical reduction and thermal reduction make carbon aerogels more electrically conductive, which is imperative to their performance in EDLCs.

GO can be chemically reduced by treatment with several reducing agents, such as hydrazine,[36,37] urea,[38] $NaBH_4$,[39] or concentrated base.[40] Curiously, researchers have also shown deoxygenation of GO that is indicative of reduction to graphene, but in the absence of any reducing agents.[41] Low concentrations of GO can be reduced during heating in a sealed vessel using several different solvents, using much lower temperature than would be needed to reduce GO to carbon in a gas environment.[42] This synthetic technique has been applied to the creation of hybrid materials from metal oxide nanoparticles and reduced GO for use as electrochemical catalysts and battery anodes.[43,44] None of the solvents used in these studies are good reducing agents themselves, so it seems that the self-generated pressure inside the vessel is an important factor in the reaction of GO. Furthermore, there is a striking similarity between conditions in these studies and that of hydrothermal gelation, so we must expect to see signs of reduction in GO-based gels. This issue will be explored further in the next chapter.

GO-based aerogels have been tested in the literature for their performance as EDLCs, in addition to other electrochemical applications such as Li ion storage.[31] The benchmark for comparing possible EDLC materials is the commercially available activated carbons which are currently in use. These activated carbons span a range of approximately 50-300 F/g, and the capacitance seems to roughly correlate with the surface area.[45] Within a similar class of materials, researchers are able to express the capacitance of a carbon surface in terms of F/m^2, but this value depends on many factors including method of preparation. As shown in Table 4.1, the capacitance and surface area values for advanced, GO-based porous carbon materials vary widely, due to the large variety of synthetic techniques.

Lead author	SA (m^2/g)	C (F/g)
Wen[30]	465	248
Wu[24]	295	226
Li[28]	1810	178
Zhu[26]	3100	166
Worsley[18]	1314	165
Chmiola[46]	1000	140
Stoller[47]	705	135
Biener[48]	3000	105
Theoretical value for graphene	2630	550

Table 4.1. Experimentally-determined surface area (SA) and specific capacitance (C) of a variety of GO-based porous materials from the cited references. SA for graphene was calculated from the geometry of the graphene unit cell, with 5.24 $Å^2$ per atom of carbon. C for graphene was calculated using the quantum capacitance of graphene in an ionic liquid, 21 $\mu F/cm^2$.[49]

Surface area values listed in Table 4.1 were obtained from the BET model, so they are directly comparable, though perhaps not accurate due to limitations discussed above. For specific capacitance, some authors used galvanostatic discharge to determine C, and some used cyclic voltammetry. Values listed for C are the highest ones measured in the cited reference for a particular sample; therefore, these measurements come from a range of different voltage scan rates or current densities.

Porous carbons dominate the existing market for EDLCs, but there remains a great deal of room for improvement in their properties before supercapacitors become widely competitive with other forms of energy storage. Continued research into new synthetic methods and advanced structure characterization of GO-based aerogels will result in their improved performance in a variety of electrochemical applications.

References

(1) Becker, H. I. Low voltage electrolytic capacitor. 2800616, 1957.

(2) Biener, J.; Stadermann, M.; Suss, M.; Worsley, M. A.; Biener, M. M.; Rose, K. A.; Baumann, T. F. *Energy Environ. Sci.* **2011**, *4*, 656–667.

(3) Pandolfo, A. G.; Hollenkamp, A. F. *J. Power Sources* **2006**, *157*, 11–27.

(4) Davies, A. Development of Electro-active Graphene Nanoplatelets and Composites for Application as Electrodes within Supercapacitors, 2012.
(5) Simon, P.; Gogotsi, Y. *Nat. Mater.* **2008**, *7*, 845–854.
(6) Sing, K.; Everett, D.; Haul, R.; Moscou, L.; Pierotti, R.; Rouquerol, J.; Siemieniewska, T. *Pure Appl Chem* **1985**, *57*, 603–619.
(7) Brunauer, S.; Emmett, P.; Teller, E. *J. Am. Chem. Soc.* **1938**, *60*, 309–319.
(8) El-Merraoui, M.; Aoshima, M.; Kaneko, K. *Langmuir* **2000**, 4300–4304.
(9) Barrett, E.; Joyner, L.; Halenda, P. *J. Am. Chem. Soc.* **1951**, *73*, 373–380.
(10) Kaneko, K. *J. Memb. Sci.* **1994**, *96*, 59–89.
(11) Groen, J. C.; Peffer, L. A. A.; Pérez-Ramírez, J. *Microporous Mesoporous Mater.* **2003**, *60*, 1–17.
(12) Stoller, M. D.; Ruoff, R. S. *Energy Environ. Sci.* **2010**, *3*, 1294.
(13) Sun, H.; Xu, Z.; Gao, C. *Adv. Mater.* **2013**, *25*, 2554–2560.
(14) Buckley, A.; Greenblatt, M. *J. Chem. Educ.* **1994**.
(15) Pekala, R. W. *J. Mater. Sci.* **1989**, *24*, 3221–3227.
(16) Pekala, R. W.; Alviso, C. T.; Kong, F. M.; Hulsey, S. S. *J. Non. Cryst. Solids* **1992**, *145*, 90–98.
(17) Al-Muhtaseb, S. A.; Ritter, J. A. *Adv. Mater.* **2003**, *15*, 101–114.
(18) Worsley, M. A.; Kucheyev, S. O.; Mason, H. E.; Merrill, M. D.; Mayer, B. P.; Lewicki, J.; Valdez, C. A.; Suss, M. E.; Stadermann, M.; Pauzauskie, P. J.; Satcher, J. H.; Biener, J.; Baumann, T. F. *Chem. Commun.* **2012**, *48*, 8428–8430.
(19) Worsley, M. A.; Pauzauskie, P. J.; Olson, T. Y.; Biener, J.; Satcher, J. H.; Baumann, T. F. *J. Am. Chem. Soc.* **2010**, *132*, 14067–14069.
(20) Niu, Z.; Liu, L.; Zhang, L.; Chen, X. *Small* **2014**, *10*, 3434–3441.
(21) Yavari, F.; Chen, Z.; Thomas, A. V.; Ren, W.; Cheng, H.-M.; Koratkar, N. *Sci. Rep.* **2011**, *1*, 166.
(22) Worsley, M. A.; Charnvanichborikarn, S.; Montalvo, E.; Shin, S. J.; Tylski, E. D.; Lewicki, J. P.; Nelson, A. J.; Satcher, J. H.; Biener, J.; Baumann, T. F.; Kucheyev, S. O. *Adv. Funct. Mater.* **2014**, *24*, 4259–4264.
(23) Bordjiba, T.; Mohamedi, M.; Dao, L. H. *Adv. Mater.* **2008**, *20*, 815–819.
(24) Wu, Z.-S.; Sun, Y.; Tan, Y.-Z.; Yang, S.; Feng, X.; Müllen, K. *J. Am. Chem. Soc.* **2012**, *134*, 19532–19535.
(25) Qiu, L.; Liu, J. Z.; Chang, S. L. Y.; Wu, Y.; Li, D. *Nat. Commun.* **2012**, *3*, 1241.
(26) Zhu, Y.; Murali, S.; Stoller, M. D.; Ganesh, K. J.; Cai, W.; Ferreira, P. J.; Pirkle, A.; Wallace, R. M.; Cychosz, K. A.; Thommes, M.; Su, D.; Stach, E. A.; Ruoff, R. S. *Science* **2011**, *332*, 1537–1541.
(27) Wei, W.; Yang, S.; Zhou, H.; Lieberwirth, I.; Feng, X.; Müllen, K. *Adv. Mater.* **2013**, 1–6.
(28) Li, Y.; Li, Z.; Shen, P. K. *Adv. Mater.* **2013**, 2474–2480.
(29) Fechler, N.; Fellinger, T.-P.; Antonietti, M. *Adv. Mater.* **2012**, 1–5.
(30) Wen, Z.; Wang, X.; Mao, S.; Bo, Z.; Kim, H.; Cui, S.; Lu, G.; Feng, X.; Chen, J. *Adv. Mater.* **2012**, *24*, 5610–5616.
(31) Han, S.; Wu, D.; Li, S.; Zhang, F.; Feng, X. *Adv. Mater.* **2014**, *26*, 849–864.
(32) Gash, A. E.; Tillotson, T. M.; Satcher Jr, J. H.; Hrubesh, L. W.; Simpson, R. L. *J. Non. Cryst. Solids* **2001**, *285*, 22–28.
(33) Mohanan, J. L.; Arachchige, I. U.; Brock, S. L. *Science* **2005**, *307*, 397–400.
(34) Bai, H.; Li, C.; Wang, X.; Shi, G. *J. Phys. Chem. C* **2011**, *115*, 5545–5551.

(35) Bi, H.; Yin, K.; Xie, X.; Zhou, Y.; Wan, N.; Xu, F.; Banhart, F.; Sun, L.; Ruoff, R. S. *Adv. Mater.* **2012**, 5124–5129.
(36) Stankovich, S.; Dikin, D. A.; Piner, R. D.; Kohlhaas, K. A.; Kleinhammes, A.; Jia, Y.; Wu, Y.; Nguyen, S. T.; Ruoff, R. S. *Carbon* **2007**, *45*, 1558–1565.
(37) Li, D.; Müller, M. B.; Gilje, S.; Kaner, R. B.; Wallace, G. G. *Nat. Nanotechnol.* **2008**, *3*, 101–105.
(38) Lei, Z.; Lu, L.; Zhao, X. S. *Energy Environ. Sci.* **2012**, *5*, 6391–6399.
(39) Shin, H.-J.; Kim, K. K.; Benayad, A.; Yoon, S.-M.; Park, H. K.; Jung, I.-S.; Jin, M. H.; Jeong, H.-K.; Kim, J. M.; Choi, J.-Y.; Lee, Y. H. *Adv. Funct. Mater.* **2009**, *19*, 1987–1992.
(40) Fan, X.; Peng, W.; Li, Y.; Li, X.; Wang, S.; Zhang, G.; Zhang, F. *Adv. Mater.* **2008**, *20*, 4490–4493.
(41) Dubin, S.; Gilje, S.; Wang, K.; Tung, V.; Cha, K. *ACS Nano* **2010**, *4*, 3845–3852.
(42) Nethravathi, C.; Rajamathi, M. *Carbon* **2008**, *46*, 1994–1998.
(43) Liang, Y.; Li, Y.; Wang, H.; Zhou, J.; Wang, J.; Regier, T.; Dai, H. *Nat. Mater.* **2011**, *10*, 780–786.
(44) Wang, H.; Cui, L.-F.; Yang, Y.; Sanchez Casalongue, H.; Robinson, J. T.; Liang, Y.; Cui, Y.; Dai, H. *J. Am. Chem. Soc.* **2010**, *132*, 13978–13980.
(45) Centeno, T. a.; Stoeckli, F. *J. Power Sources* **2006**, *154*, 314–320.
(46) Chmiola, J.; Yushin, G.; Gogotsi, Y.; Portet, C.; Simon, P.; Taberna, P. L. *Science* **2006**, *313*, 1760–1763.
(47) Stoller, M. D.; Park, S.; Zhu, Y.; An, J.; Ruoff, R. S. *Nano Lett.* **2008**, *8*, 3498–3502.
(48) Biener, J.; Dasgupta, S.; Shao, L.; Wang, D.; Worsley, M. A.; Wittstock, A.; Lee, J. R. I.; Biener, M. M.; Orme, C. A.; Kucheyev, S. O.; Wood, B. C.; Willey, T. M.; Hamza, A. V; Weissmüller, J.; Hahn, H.; Baumann, T. F. *Adv. Mater.* **2012**, *24*, 5083–5087.
(49) Xia, J.; Chen, F.; Li, J.; Tao, N. *Nat. Nanotechnol.* **2009**, *4*, 505–509.

Chapter 5

Toward a Mechanistic Understanding of the Hydrothermal Gelation of Graphene Oxide

5.1 When does graphene oxide become a graphene aerogel?

As discussed in Chapter 4, graphene oxide (GO) is widely used as a precursor for the aqueous synthesis of high surface area materials. Gelation of GO sheets can be accomplished across a range of temperatures utilizing its native chemical functionality, with or without addition of base.[1,2] A better understanding of the GO sol-gel transition understanding is fundamental to precise chemical manipulation of GO sheets in solution and in obtaining GO-based aerogels with controllable properties.

The chemical structure of GO, based on the Lerf-Klinowski model,[3] consists primarily of a carbon network decorated with hydroxyls and 1,2-epoxides. Erickson et al. were able to identify hydroxyl and epoxide groups within a sheet of GO using atomic-resolution transmission electron microscopy (TEM).[4] This study provided evidence of the nanoscale composition of GO, showing heavily oxidized regions interspersed with holes and segments of undisturbed graphene. Worsley et al. have shown that, upon gelation, the peaks from hydroxyl, epoxide, and carboxyl groups in the ^{13}C NMR spectrum of GO disappeared.[1,5] Meanwhile, a peak emerges upfield in the spectrum of gelled GO corresponding to the presence of sp^3-bonded carbon in methylene groups, similar to those observed in the cross-linkages of carbon aerogels.[6] This suggests that covalent linkages between sheets are responsible for the formation of a hydrogel from GO. However, others have speculated that GO sheets are bound together by π-π stacking,[2] so there is not yet a consensus on the bonding mechanism responsible for gelation.

Prior publications on gelation of GO use the conventional nomenclature from the literature, where reduced GO is used as an analogue for graphene; authors typically refer to aerogels following thermal annealing as "graphene aerogels."[10,11] Most of the prior characterization work has been done on these annealed aerogels; much less is known about the intermediate product between "graphene oxide" and "graphene aerogel." Here we aim to more thoroughly characterize the aerogel before it is annealed in order to identify the key chemical and physical changes responsible for the sol-gel transition of pure GO systems. By characterizing GO at various time points during the transition from GO solution to a sol-gel, we show that a number of changes in the physical, chemical, and optical properties emerge simultaneously upon gelation.

5.2 Hydrothermal gelation of graphene oxide

Graphene oxide powder was purchased from Cheap Tubes, Inc. and dispersed in deionized water via overnight bath sonication of 10-20 mg/mL solutions. Hydrogels were produced via two methods for this work:

1. *At lower temperature with base.* As previously reported,[1] GO solution was mixed with 16 % v/v concentrated NH_4OH and was enclosed in a capped glass vial and heated to 80°C. Vials were not agitated for the duration of the reaction, which proceeded over a period of 3 days. Gelation does not proceed on a reasonable time scale at 80°C without addition of base. This synthetic technique can also be performed using two glass slides separated by a gasket and secured with clips to retain the pressure. Care should be used in selecting a gasket material that is appropriate for heated liquid environments, as some silicone products can contaminate the hydrogel.

2. *At higher temperature with no base added*. This method was performed using Teflon-lined pressure vessels purchased from Parr Instrument Company. The vessels were filled with GO solution, with no base added. These GO solutions were reacted for different time periods (up to 18 hours) in a pre-heated oven at 180 °C and then allowed to cool. Reaction temperatures below 180 °C yield small pieces of black hydrogel floating in water, rather than a monolithic hydrogel; the same product results from slow temperature ramping, because the reaction proceeds at a lower temperature before it reaches thermal equilibrium.

Gels of varying sizes can be made by placing smaller glass vials filled with GO solution inside the Teflon liner. In addition to centimeter scale monoliths, thin films of hydrogel were also made by pressing together two glass slides with GO solution in the interstitial volume. When this glass slide assembly is immersed in water and heated inside a pressure vessel, the result is millimeter size flakes that are mostly transparent and black in color.

Monolith samples reacted for longer than 90 minutes were dried using a manual supercritical CO_2 dryer from Structure Probe, Inc. Samples were pressurized and then heated past the critical point of CO_2 (31 °C and ~1100 psi) to create a supercritical fluid. The pressure was then released and the fluid became a gas as it cooled, thereby circumventing the critical point. Before supercritical drying, the water in the hydrogel pores must be exchanged for a solvent that is miscible with liquid CO_2, such as isopropanol or acetone. Gels are allowed to soak repeatedly in fresh solvent until the solvent exchange is complete. Agitation of the vial is necessary to expedite this mixing process.

Additionally, it is important to allow a sufficient soaking time and number of soak cycles during supercritical drying, or else the pores that retain liquid solvent at room temperature will collapse during evaporation. Gels that are incompletely dried have lower surface area and higher density. This is a similar effect to the density control of porous carbons demonstrated by Yang et al.,[12] wherein the carbon pores are penetrated by a volatile/nonvolatile solvent mixture and then exposed to vacuum. The density, and thus the pore volume, of the material is determined by the ratio of volatile to nonvolatile solvent.

5.3 Physical structure of graphene oxide gelation product

After undergoing heat treatment within the pressure vessel, the samples are visually inspected to assess any macroscopic changes to the GO solution. The graphene oxide hydrogels made via both methods take the shape of their container, but are approximately 50% smaller in each dimension. Hydrogels made by the low-temperature method could be observed to shrink over the course of the reaction—most dramatically during the first 24 hours. For the high-temperature method, the pressure vessel is not transparent, so the samples were removed from the oven at discrete time points for observation.

In order to precisely track the progress of the reaction vs. time spent in the oven, one needs to know the rate of temperature change inside the reaction mixture. Temperature inside the pressure vessel under true reaction conditions was not directly measured because of the need for a tight seal. We were able to measure the heating inside an empty pressure vessel, as well as the heating inside a vessel with water below its boiling point, by inserting a thermocouple into the center of the Teflon liner. Based on the results in Figure 5.1, we estimate that at least 60 minutes must elapse before the solution reaches the reaction temperature.

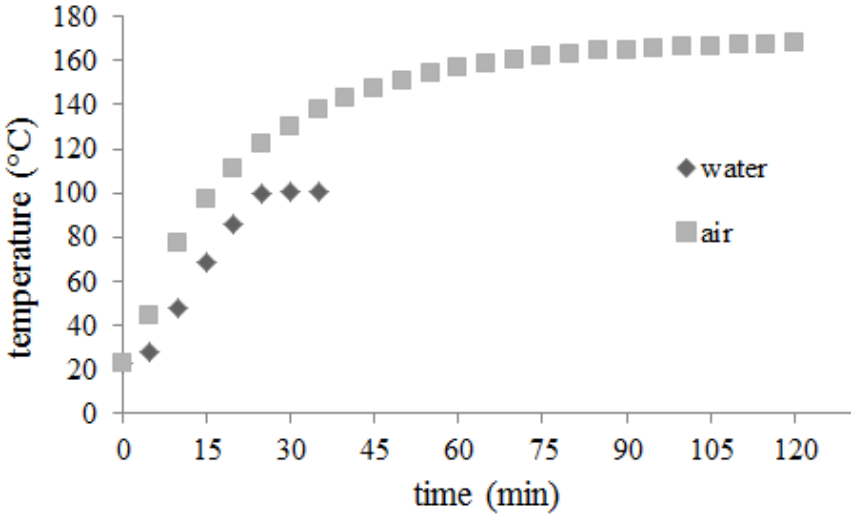

Figure 5.1. Plot showing temperature vs. heating time inside a Parr pressure vessel placed in an oven at 180 °C. The upper curve was measured with an empty vessel (air), and the lower curve was measured with water inside.

For samples heated to 180 °C for up to 60 minutes, at which point the mixture is expected to have reached equilibrium temperature, the resulting solution appears by eye to be a continuous dark brown solution, similar to the starting material but with higher viscosity (Figure 5.2a). At approximately the 75 minute time point, a dramatic transition in density occurs—by 90 minutes of reaction, the GO solution has transformed into a black hydrogel suspended in water (Figure 5.2b). Characterization by transmission electron microscopy (TEM) shows that the changes in macroscopic physical structure of the samples are also reflected on the nanoscale. TEM was done using a JEOL 2010 microscope at 80 kV. The GO sheets after 60 minutes of gelation at 180 °C mostly lie flat, with some texture observed around the edges (Figure 5.2c). However, after 90

minutes, there are no flat portions of GO remaining; the entire sample is composed of a heavily textured matrix with high curvature and nanoscale pore structure (Figure 5.2d-e). (Because the TEM samples are prepared by dropcasting fragments of the hydrogel, we expect some structural changes associated with drying of these fragments in air. The TEM images in Figure 5.2 are therefore indirectly correlated with the structure of the as-made hydrogel.)

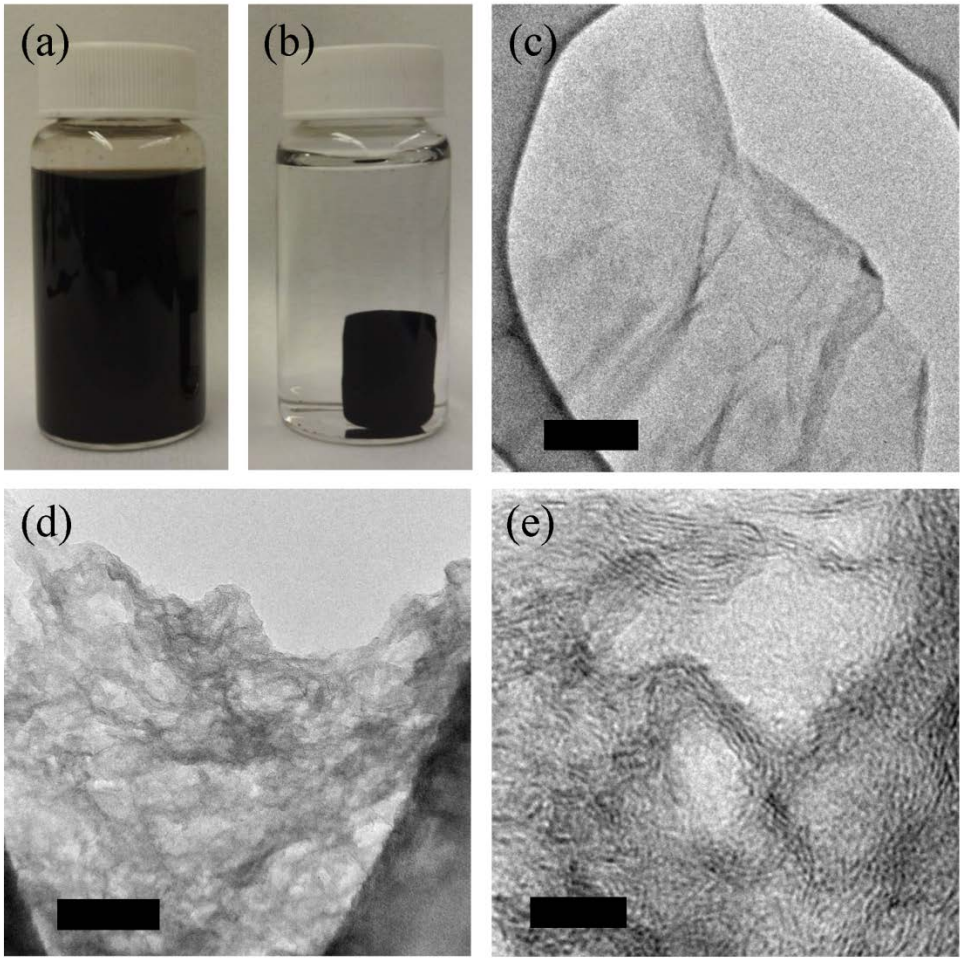

Figure 5.2. Photographs of a GO solution (a) and a formed hydrogel (b) inside a 20 mL vial, and representative TEM images of hydrogel reacted for 60 (c) and 90 (d, e) min. Scale bars are (c) 200 nm, (d) 50 nm, and (e) 5 nm. From Goldstein *et al*.[13]

The TEM images shown in Figure 5.2d-e are representative of fully-formed hydrogels made by both low- and high-temperature synthetic methods. The fact that, upon gelation, the 2-D GO sheets have developed 3-D nanoscale features suggests that chemical bonding is changed throughout the entire GO sheet, not only at the edges. Additionally, the change in morphology suggests that bonds are forming between different GO sheets after approximately 75 min. of reaction time, as the crumpling of the sheets causes a simultaneous macroscopic shrinkage of the gel.

The wrinkled nanoscale structure results in highly porous aerogels after the samples are dried. We used nitrogen adsorption porosimetry to investigate the aerogels' gravimetric surface area and pore volume with a Micromeritics ASAP 2020 porosimeter. Two typical isotherms obtained by this method are shown in Figure 5.3. The shape of the isotherm is best described as Type IV based on nomenclature recommended by the IUPAC,[14] with Type H3 hysteresis. The branches of the hysteresis loop are neither horizontal nor vertical, and there is no saturation of nitrogen uptake at high relative pressure. This isotherm shape is characteristic of a material with pores that are slit-shaped pores and covering a broad distribution of diameters in the mesoporous region (2-50 nm).

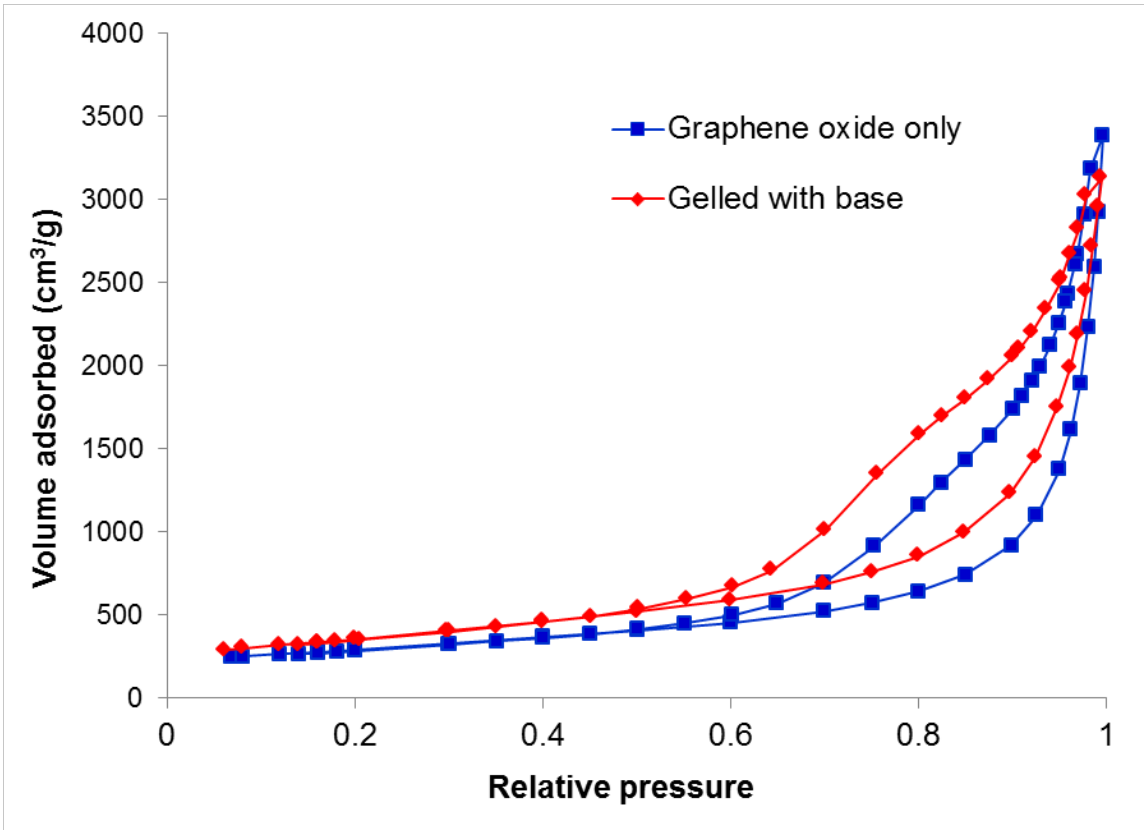

Figure 5.3. Nitrogen adsorption isotherm for two aerogels, formed from GO with NH_4OH at 80 °C (red diamonds) and formed from GO with no base at 180 °C (blue squares).

Porosimetry results (shown Table 5.1) indicate a similar physical structure for aerogels formed at 80°C and those formed at 180°C. Samples made with base at the lower temperature have higher surface area and higher micropore volume, but lower mesopore volume. Because the higher temperature process is faster and free of possible effects of nitrogen incorporation, hydrogel samples analyzed further in this work were formed directly from aqueous GO solution at 180°C unless otherwise stated.

	Graphene oxide only	With NH_4OH	Percent change with NH_4OH

	Graphene oxide only	With NH_4OH	Percent change with NH_4OH
BET surface area (mesopore analysis)	1019.3 m^2/g	1255.4 m^2/g	+23%
BJH adsorption pore volume (17-3000 Å)	5.24 cm^3/g	4.90 cm^3/g	-6.5%
Micropore volume (≤ 29.49 Å)	0.38 cm^3/g	0.45 cm^3/g	+18%

Table 5.1. Surface area and pore volume from porosimetry analysis of samples made by high-temperature (graphene oxide only) and low-temperature (with NH_4OH) synthetic methods.

It is important to note that when collecting porisimetry data on monolithic aerogels, the macroscopic state of the sample can have a significant effect on the measurement outcome. For example, we measured the surface area and pore volume of a dried monolith of gelled GO, and then crushed the aerogel into a powder and repeated the measurement. The result for the crushed gel was only very slightly increased surface area (6%), but a 60% increase in mesopore volume. This effect is likely due to the destruction of pores during the crushing process. The creation of additional macroscopic surface area (the outside of a flake in the powdered gel) should not impact the mesopore SA measurement, because the same total wall area is available for nitrogen adsorption, but it does apparently create more total volume for liquid nitrogen to condense.

In terms of sample handling, it is convenient to only measure porosimetry of aerogel monoliths, which are very easily inserted into the sample tube and then removed. However, the accuracy of the measurement requires that the total amount of surface area is on the order of 10-100 m^2. So if the gravimetric surface area of a sample is low, researchers may be compelled to crush the aerogel to obtain enough material in the sample tube, which has a standard diameter of ½". Whichever technique is used, consistent sample treatment (e.g. grinding with a mortar and pestle, or using monoliths of similar size) is necessary to obtain comparable measurements.

5.4 Chemical structure of graphene oxide gelation product

While the GO sheets are undergoing physical wrinkling and shrinkage to create a porous hydrogel structure, data from a variety of characterization methods show that chemical changes are also taking place within the carbon sheet.

5.4.1 Energy-dispersive x-ray spectroscopy (EDS) and X-ray photoelectron spectroscopy (XPS)

X-ray photoelectron spectroscopy (XPS) was performed using a Omicron EA 125 system with a monochromated Al source at 1486.6 eV. Samples were sonicated and dropcast on an Au thin film, and the Au 4f peak was used to verify the binding energy. Energy-dispersive x-ray

spectroscopy (EDS) data were collected using an EDAX Genesis 2000 x-ray analyzer. In Figure 5.4a, we show that the carbon network of graphene oxide undergoes significant deoxygenation during gelation, based on an increase in the C/O atomic ratio with reaction time. The C/O ratio increases from 3 to 12. The C/O values obtained from EDS are less surface sensitive than XPS, and the spectra have lower energy resolution, but are nonetheless very useful for relative comparisons between samples.

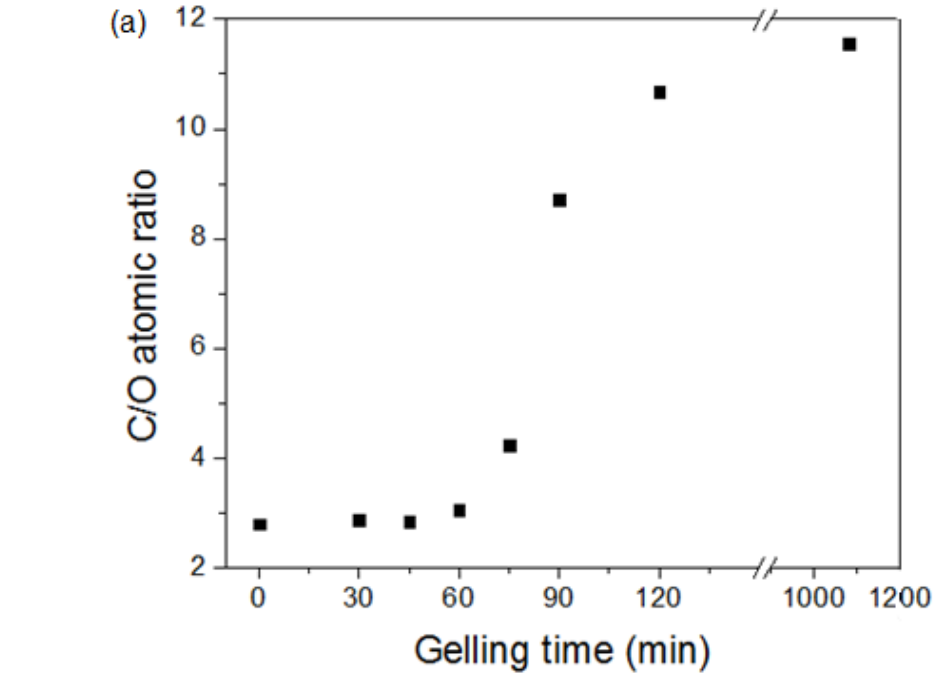

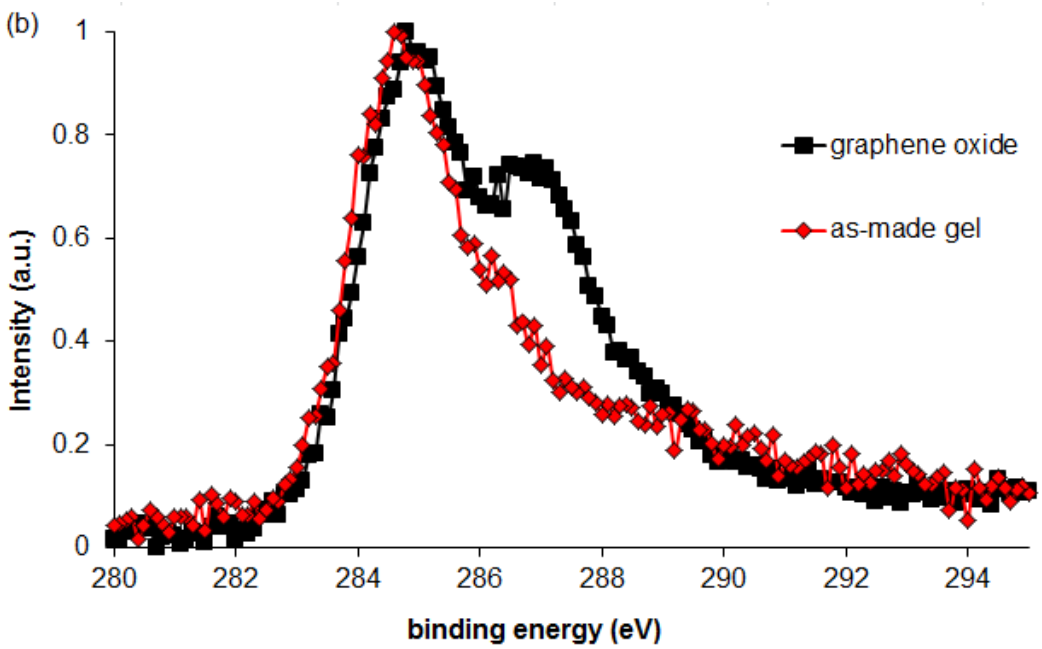

Figure 5.4. (a) Atomic ratios of carbon to oxygen based on EDS signal. (b) XPS data for GO powder and a fully reacted gel. Spectra are normalized at the maximum signal and baseline subtracted.

Deoxygenation during gelation is also observed based on the change in shape of the carbon K-edge by XPS (Figure 5.4b). The peak between 286 and 290 eV is commonly observed in graphene oxide due to carbon-oxygen bonding. This region of the spectrum is assigned to carbon-oxygen bonds of different types: C-O single bonds (285.8-286.7 eV), C=O double bonds (287.0-288.0 eV), and carboxylic groups (288.5-290.0 eV).[15] The C1s spectrum of both the as-made aerogel and the annealed aerogel are dominated by the C-C bonding portion of the peak (284.5-285.0 eV). The major change in peak shape between graphene oxide and the gel is the loss of C=O double bonds and, to a lesser extent, C-O single bonds.

The carbon K-edge for the gelled sample appears to have even less oxygen functionality than previously reported spectra of GO reduced either by hydrazine at 70°C or in H_2 at 500°C,[16] despite the fact that our reaction was carried out with simply GO and water. This significant change in the oxygen content cannot be explained solely by bonding changes along the edges of the GO sheets, but rather suggests a decrease in C-O and C=O bonding throughout the entire sheet. This is consistent with the evolution of the gel's physical appearance, which indicates that changes in bonding occur throughout the body of the GO sheets as they contract and wrinkle. Therefore, the physical and the chemical changes that occur during the sol-gel transition seem to be related, as bonding within and between GO sheets is accompanied by a loss of oxygen functional groups.

XPS data were also used to calculate the elemental composition of these samples. Shirley background subtraction was performed, spectra were fit to obtain the component sub-peaks, and the ratio between raw peak intensities was converted to an atomic ratio using the cross-sections for photoemission of carbon and oxygen atoms. The C/O ratio for each sample was then calculated by two methods:

i. Integrating the background-subtracted intensities of the C1s and O1s peaks, and converting these to atomic ratios
ii. Comparing the O-bonded C1s components to the overall C1s intensity, after scaling by number of bonded oxygen atoms per carbon atom.

The second method is less reliable in the present case, because the C-O single bonded component could represent carbon atoms in functional groups with different C/O ratios (e.g. 1:1 for hydroxyls and 2:1 for epoxides). The C/O ratio calculated from the first method is 1.9 for GO, which is consistent with literature reports for fully oxidized GO.[17] For the as-made aerogel, the C/O ratio increases to 3.2. These values follow the same trend as the qualitative comparison of C1s components above, indicating loss of oxygen during gelation. Table 5.2 contains the full results of peak fitting for GO before and after gelation.

		GO powder	As-made gel

Assignment	Expected Range[a] (eV)	Energy (eV)	Area	Energy (eV)	Area
C-C (1)	*284.5-285.0*	284.9	57.4%	284.5	49.8%
C-C (2)	*285.2-285.9*	--	--	285.4	11.9%
C-O	*285.8-286.7*	286.7	18.6%	286.3	7.5%
C=O	*287.0-288.0*	287.4	7.3%	287.0	9.5%
O-C=O	*288.5-290.0*	288.4	15.5%	288.8	16.5%
$\pi-\pi^*$	--	290.8	1.2%	292[b]	4.7%
C 1s/ O1s atomic ratio		1.9		3.2	
C/O ratio from C1s fit[c]		1.7-2.1		1.9-2.1	

Table 5.2. Selected XPS fitting parameters from the C1s peak of three samples. a: From Yumitori.[15] b: Peak was constrained due to noise in the high energy region. Area totals may not add to 100% due to rounding error. c: The lower and upper limits are given here by assuming that the C-O peak is due to hydroxyls and epoxides/ethers, respectively.

Graphitic samples typically have asymmetric C1s peaks by XPS, which can be fit by either an asymmetric peak shape or by inclusion of a 2nd symmetric peak component.[15] Additionally, sp^3 carbon yields a C-C bonding peak that is shifted toward slightly higher binding energy.[18] After gelation, we see a trend toward increasing sp^2 bonding based on three changes: the addition of a 2nd graphitic peak for the hydrogel, a shift to lower energy of the graphitic peaks, and the increasing proportion of π bonding based on the π-π^* plasmon peak at >290 eV.[18]

There are some limitations in the peak fitting results presented here, due to noise in the measurement and multiple overlapping peak components. Also, in the case of the as-made aerogel, the C/O ratio calculated from the components of the C1s peak fitting (method i) does not match well with the ratio calculated from the C1s and O1s integrated peak intensities (method ii). This could result from a fitting error causing overestimation of the presence of oxygen-bonded carbon. Alternatively, there could be a non-carbon-bonded source of oxygen present in the sample, such as adsorbed water molecules. Ultimately, we recognize that mixed sp^2-sp^3 samples are difficult to fit reliably, so we derive conclusions only from a qualitative comparison of the overall peak shapes.

5.4.2 Thermogravimetric analysis (TGA)

One consequence of losing a large percentage of oxygen is that, following gelation, the aerogels have remarkable thermal stability. Thermogravimetric analysis (TGA) of the reacted GO after drying in air are shown in Figure 5.5. TGA data were collected using a TGA 7 from Perkin Elmer. Samples were heated at 10°C/minute in a 4:1 mixture of Ar and O_2 gases. GO undergoes a significant mass loss at around 200°C, due to loss of oxygen functional groups.[7,19] Samples that were reacted for less than 60 min. show similar results to the starting material. However, the low-temperature degradation is somewhat lessened for samples reacted for 75 minutes, and it is completely absent for reaction times of 90 min. or longer. The weight remaining after oxygen removal increases from 65% in GO to over 95% after 90 minutes of gelation. The timescale of the evolving thermal properties during gelation exactly matches that of the above characterizations, which again demonstrates that the sol-gel transition requires significant deoxygenation of GO.

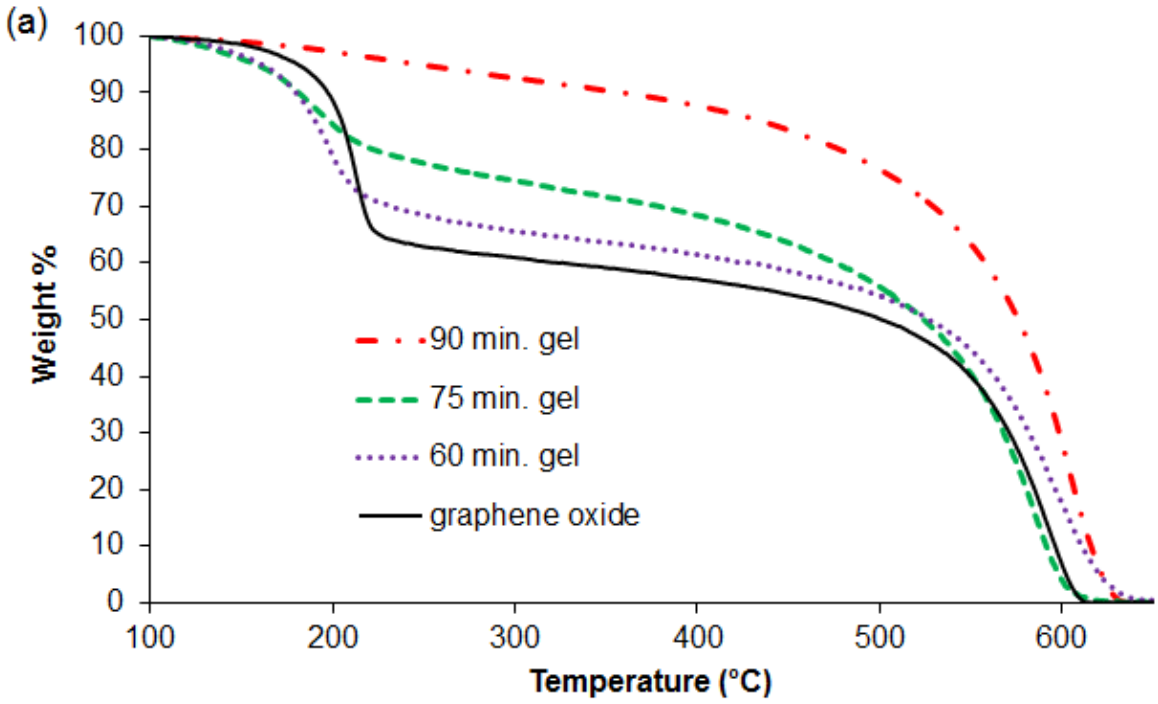

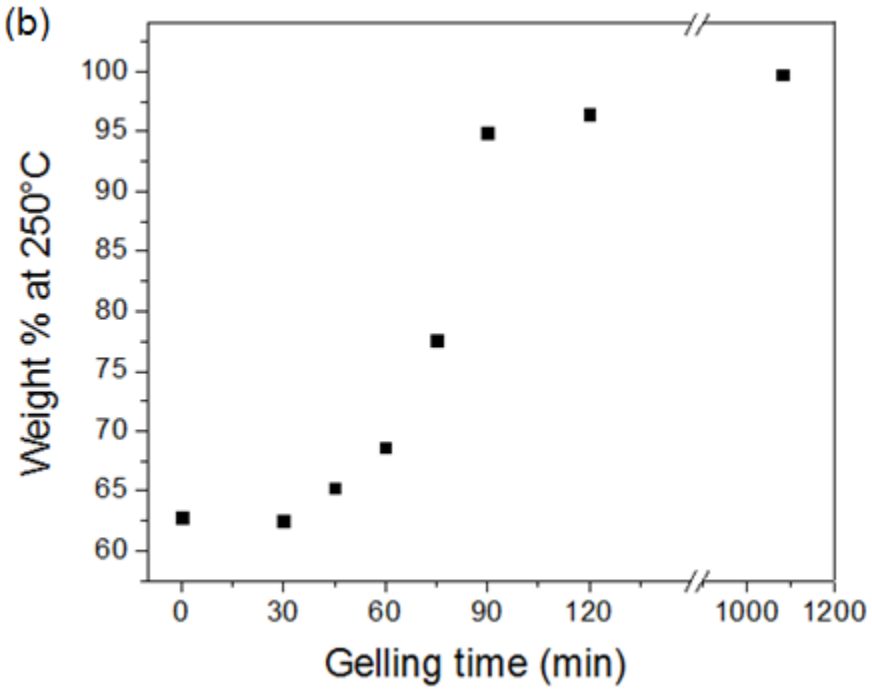

Figure 5.5. (a) TGA results normalized at 100 °C, baseline subtracted. (b) Plot of low-temperature mass loss as a percent of the original mass vs. gelation time.

5.4.3 UV-visible absorption spectroscopy (UV-vis) and Raman spectroscopy

Further evidence for the coupling of the chemical and physical changes during gelation comes when we monitor the UV-visible absorption spectrum of GO samples reacted for different times (Figure 5.6a). UV-visible absorption spectroscopy (UV-vis) was done with a Genesys 10S spectrometer from Thermo Scientific. Graphene oxide and the 60 minute sample were sonicated for approximately 10 seconds before UV-vis analysis; other samples were sonicated 2-3 minutes to create a stable suspension. Not all solid material was suspended, thus the solutions are of unknown concentration. For this reason, absorption values are arbitrary, and the spectra are normalized at 300 nm in order to compare their shape.

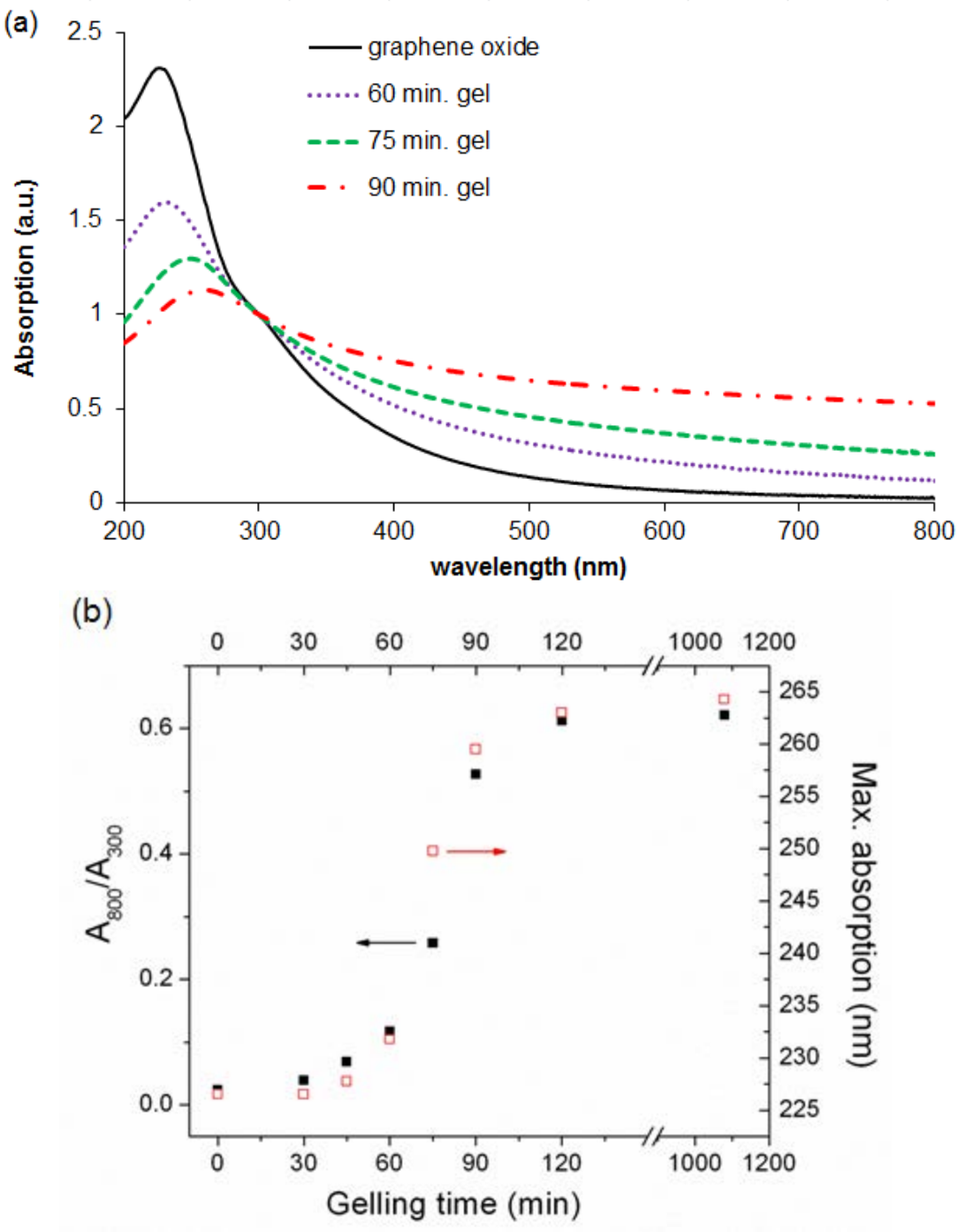

Figure 5.6. (a) UV-vis spectra of GO at various time points of hydrothermal gelation. Spectra have been normalized at 300 nm. Samples reacted for 0 and 60 minutes were sonicated approximately 10 seconds; samples reacted for 75 and 90 minutes were more solid and required 2-3 minutes sonication. (b) Overlaid plot of peak absorption wavelength and visible/UV absorption ratio vs. gelation time.

The starting GO material shows a large UV absorption peak at ~230 nm and a decaying absorption in the visible region, consistent with its brown color. This spectrum remains

unchanged until 60-75 minutes of reaction time, when the absorption in the visible region begins to change in two ways: i) the peak absorption is red-shifted and ii) the relative UV absorption is significantly decreased. After 90 minutes, the position of the maximum in UV-visible absorption spectrum has shifted from 230 nm to 265 nm, while the relative absorption at 800 nm to that at 300 nm has increased from ~0.02 to 0.6. Absorption across the spectrum becomes quite flat after gelation, giving rise to the sample's black color. Plotting both the wavelength of the absorption peak and the ratio of absorption between near-IR and near-UV, we see that the most dramatic change in color occurs between 60 and 90 minutes. The spectrum continues to change after 90 minutes of reaction, but the rate of change becomes much slower.

The decrease in the height of the UV absorption peak for GO (~230 nm) has been ascribed to loss of oxygen-containing functional groups.[19] Additionally, the peak wavelength for UV absorption in chemically reduced graphene oxide has been observed to shift to longer wavelengths (~270 nm).[8] This shift is analogous to that observed in conjugated polymers or polycyclic aromatic molecules of increasing size. In Figure 5.6b, we see that these two phenomena happen on a nearly identical timescale for GO hydrothermal gelation. These changes can be explained as simultaneous deoxygenation and reparation of the sp^2 network, creating larger areas of conjugation to absorb across a broad range of wavelengths.[17]

If the GO sheet is indeed repaired to form larger conjugated regions during gelation, we should see an impact on the in-plane vibrations of the carbon sheet. To address this questions, Raman spectroscopy was performed on the GO before and after gelation. Raman spectra were collected using a Renishaw inVia microscope and the 514 nm line of an Ar ion laser. Gelling appears to have no significant effect on the Raman spectrum. In Figure 5.7, the spectrum for GO itself overlaps almost perfectly with the spectrum of the as-made aerogel. If the carbon sheets were being significantly repaired during gelation, we would expect to see narrower and more intense Raman peaks, as well as a change in the I_D/I_G ratio.[22]. Apparently, the change in domain size associated with gelation is not dramatic enough to register a change in the Raman spectrum. Phonons traveling through the material still experience an extremely defective and disordered lattice in the as-made aerogel, and the in-sheet vibrations are not changed by removal of oxygen.

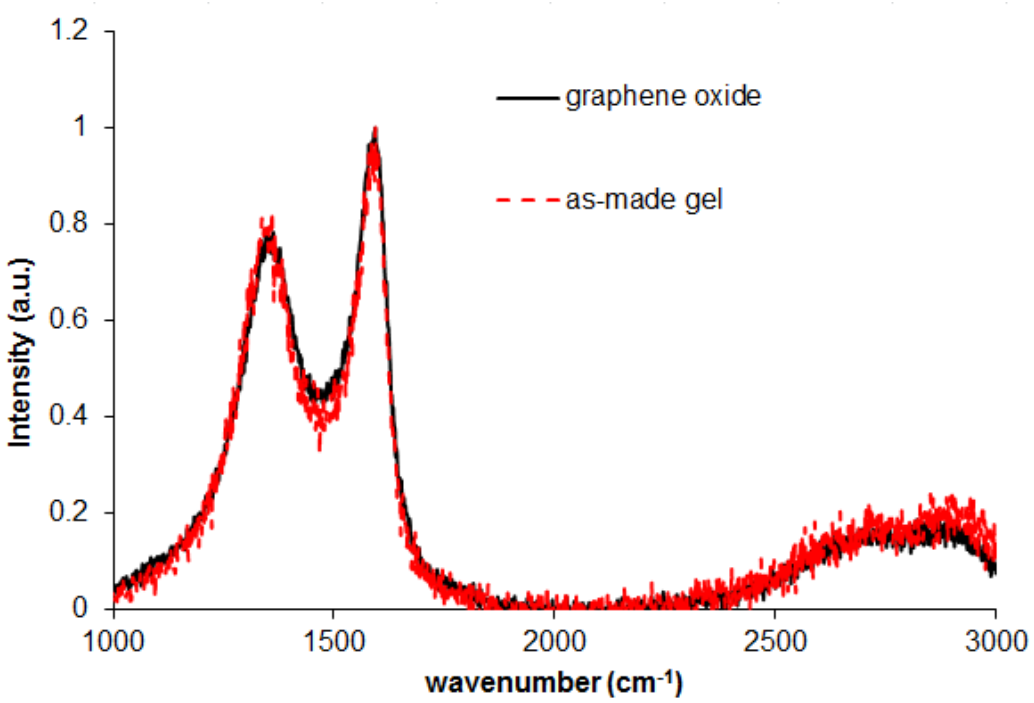

Figure 5.7. Raman spectra of GO before and after gelation. Spectra are background subtracted and normalized at the G peak (~1580 cm^{-1}).

5.5 Summary of changes during gelation

Through physical, chemical, and optical characterization at various time points in the sol-gel reaction, we have shown GO undergoes the following simultaneous and dramatic changes:

1) Densification and formation of a monolith
2) Change in texture from flat to wrinkled
3) Decrease in the oxygen concentration
4) Increase in thermal stability
5) Decrease in intensity of UV light absorption, relative to visible light
6) Shift of the UV light absorption peak to lower energy

The densification and formation of a monolith, along with the wrinkling of the constituent sheets (observations 1 and 2), confirm that GO sheets are in fact bound together during gelation, causing the gel to shrink as the sheets wrinkle to form a porous structure. Observations 3, 4, and 5 originate from a loss of oxygen-containing functional groups. The extent of the oxygen loss is too great to be ascribed solely to reactions at the edges of GO sheets. Therefore, the reaction is simultaneously a cross-linking between sheets and a chemical transformation within the body of the sheet, whereby oxygen is removed from the material.

Applications of reduced GO that rely on the low-cost of carbon as a feedstock will benefit from the realization that GO can be both gelled and deoxygenated at temperatures as low as 80 °C, avoiding the need for costly higher-temperature processes. However, a great deal remains to be

discovered about this process. For example, while these results offer an important insight into the dynamics of GO gelation, they do not settle the matter of whether sheets are bound covalently or through weaker forces such as π-π stacking.

5.6 Possible mechanisms for GO gelation

In order to better understand the gelation mechanism, we consider existing explanations in the literature for the deoxygenation of GO. Recent work by Dimiev et al.[19] shows that treating GO with strong base leads to C-C bond breakage and deoxygenation by loss of CO_2. An example chemical reaction that may occur in this process is depicted in Figure 5.8a. Though sometimes mistaken for "reduction" of GO, the overall reaction is more appropriately regarded as disproportionation, since the oxidation of carbon atoms and evolution of CO_2 are accompanied by electron donation to the remaining carbon network. Their result was found under basic conditions at temperatures up to 60 °C; it is reasonable to assume that the same effects may take place under gelation conditions, either with base at 80 °C or without base at 180 °C. The fact that we observe gas bubbles inside the reaction vessel following gelation, indicating CO_2 evolution, supports this explanation.

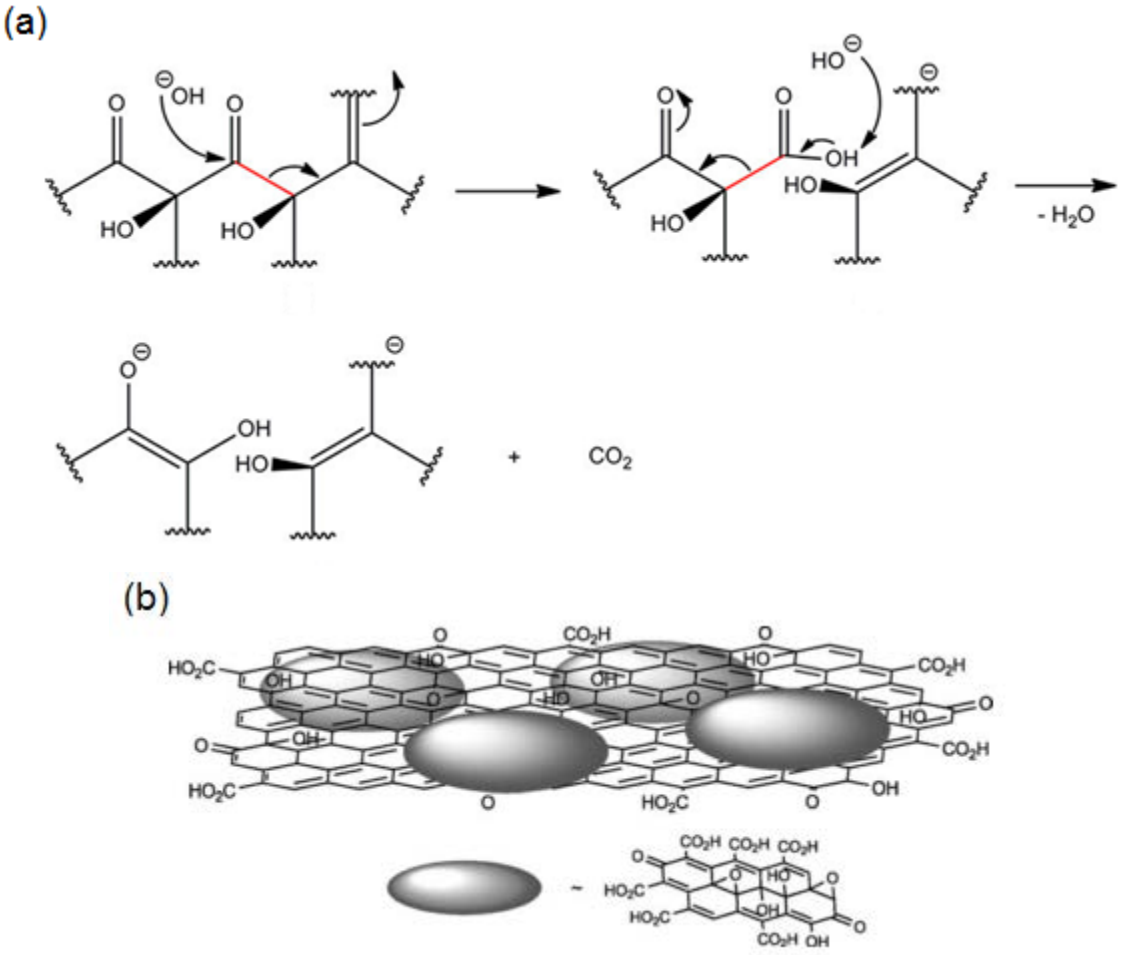

Figure 5.8. (a) Adapted from Dimiev et al.[19] The C-C bonds broken are depicted in red. In both cases, the bonding electrons are donated to the body of carbon material surrounding the oxidized carbon atom. (b) From Rourke et al.[20] A GO sheet is coated in oxidative debris, and a possible chemical structure for oxidative debris is depicted below.

An alternative mechanism for deoxygenation of GO has been proposed by Rourke and coworkers, wherein GO sheets as-made are covered in oxidative debris; base treatments remove this debris revealing hydrophobic single-layer GO sheets.[20,21] The oxidative debris takes the form of small molecular fragments which can be recovered from solution. When we use rotary evaporation to remove volatile components of the liquid phase remaining after gelation, we obtain a white solid, suggesting that some of the deoxygenation observed is indeed due to removal of small organic molecules.

In order to distinguish between these two explanations, we aim to determine the chemical nature of the mass lost. Based on the reaction in Figure 5.8a, where the carbon body incorporates two hydroxyl ions and evolves one water molecule and one CO_2 molecule, the C/O atomic ratio for the mass lost would be exactly 1 (one oxygen atom for every carbon atom lost). The balanced equation can be written as: R-CO (s) + 2 OH^- (aq) $\rightarrow$ R + H_2O + CO_2.

On the other hand, if gelation does consist primarily of the removal of such oxidative debris, the mass lost during hydrothermal gelation would be oxidized to a lesser degree. Using the example molecule shown in Figure 5.8b, we may suppose that a typical C/O ratio for oxidative debris is 1.5. So we can calculate the C/O ratio of the mass lost during gelation, expecting it to be between 1.0 and 1.5. A volume of sonicated GO solution was vacuum-filtered and compared to a dried aerogel synthesized from the same volume. The mass loss associated with gelation is found to be 44%. Equations 5.1 and 5.2 combine this mass loss with the change in oxygen concentration after gelation, and allows us to estimate the C/O ratio in the material removed from the GO after gelation: $(C/O)_{lost}$.

Equation 5.1

$$\frac{C}{O}_{lost} = \frac{\frac{C}{O}_{GO} - \left(\frac{C}{O}_{gel} \cdot \frac{m_{gel}}{m_{GO}} \cdot \Delta\right)}{1 - \frac{m_{gel}}{m_{GO}} \cdot \Delta}$$

Equation 5.2

$$\Delta = \frac{mass\%\ O_{gel}}{mass\%\ O_{GO}} = \frac{1 + \frac{3}{4} \cdot \frac{C}{O}_{GO}}{1 + \frac{3}{4} \cdot \frac{C}{O}_{gel}}$$

All C/O values are expressed here in terms of atomic ratios. The three known quantities from experiment are the i) C/O ratio of the starting material, $(C/O)_{GO}$, ii) the C/O ratio of the fully reacted gel, $(C/O)_{gel}$, and iii) the fractional mass remaining after gelation, m_{gel}/m_{GO}. The quantity Δ represents the change in oxygenated mass of the sample, expressed as a ratio of mass percent oxygen in the gel to mass percent oxygen in GO; the ratio of ¾ appears when converting mass ratios to atomic ratios using the atomic weights of carbon and oxygen.

From Equation 5.1, we find the calculated value of $(C/O)_{lost}$ to be 0.45. This ratio indicates that the majority of carbon is indeed lost as CO_2 (C/O ratio of 0.5). This is surprising, as both of the above explanations for deoxygenation would yield a C/O ratio of 1 or more. It should be noted that Equation 5.1 is very sensitive to the measured value of mass lost, so the mass measurement is a likely source of error in this calculation. We cannot rule out either explanation, and it may be the case that both play a role in hydrothermal gelation.

If reactions like the one shown in Figure 5.8a are taking place during gelation, then we might expect to see evidence of an expanding sp^2 network, as additional π bonds are created near the vacancies formed from loss of CO_2. The red-shift of peak UV-vis absorbance (Figure 5.6) is associated with chemical reduction of the carbon network, so we speculate that it may be caused by increasingly large areas of electronic conjugation, i.e. expansion of the graphitic areas imaged as seen by Erickson et al in reduced GO.[4] However, as discussed in section 5.4, we see no change in the Raman spectrum between GO and the aerogel samples as-made, so it is unclear just how much the carbon sheet is repaired during gelation. While we have shown that gelation involves loss of oxygen defects, we know also that an entirely new source of defects is introduced in the form of wrinkled sheets. The aerogels as-made are extremely disordered compared to flat graphitic sheets, so their 3D structure may also be a factor in the Raman signal.

In any case, the explanations for deoxygenation of GO from Dimiev and from Rourke both rely on the presence of base. Because gelation is successful with or without the addition of ammonium hydroxide, further work is needed to determine the mechanism for deoxygenation of GO in distilled water (pH = 5). Furthermore, no published mechanisms of GO deoxygenation are known to be associated with wrinkling of the GO sheets. One possible cause for this phenomenon would be if new C-C bonds are formed around vacancies, e.g. creation of a 5-membered ring following loss of a single carbon atom.[23] If stabilized by additional reactions with aqueous species, such defects would cause bending in an otherwise flat sheet. To our knowledge, no chemical mechanism has been demonstrated for this type of C-C bond formation during gelation, so the exact atomic rearrangements that take place remain unknown.

Further investigation into the sol-gel reaction mechanism should include detailed characterization of the intermediate chemical species in the solid product, the reaction solution, and any evolved gases. More advanced monitoring techniques should be implemented to track the reaction *in situ* under high-pressure conditions.

References

(1) Worsley, M. A.; Kucheyev, S. O.; Mason, H. E.; Merrill, M. D.; Mayer, B. P.; Lewicki, J.; Valdez, C. A.; Suss, M. E.; Stadermann, M.; Pauzauskie, P. J.; Satcher, J. H.; Biener, J.; Baumann, T. F. *Chem. Commun.* **2012**, *48*, 8428–8430.

(2) Xu, Y.; Sheng, K.; Li, C.; Shi, G. *ACS Nano* **2010**, *4*, 4324–4330.

(3) Lerf, A.; He, H.; Forster, M.; Klinowski, J. *J. Phys. Chem. B* **1998**, *102*, 4477–4482.

(4) Erickson, K.; Erni, R.; Lee, Z.; Alem, N.; Gannett, W.; Zettl, A. *Adv. Mater.* **2010**, *22*, 4467–4472.

(5) Worsley, M. A.; Charnvanichborikarn, S.; Montalvo, E.; Shin, S. J.; Tylski, E. D.; Lewicki, J. P.; Nelson, A. J.; Satcher, J. H.; Biener, J.; Baumann, T. F.; Kucheyev, S. O. *Adv. Funct. Mater.* **2014**, *24*, 4259–4264.
(6) Pekala, R. W.; Alviso, C. T.; Kong, F. M.; Hulsey, S. S. *J. Non. Cryst. Solids* **1992**, *145*, 90–98.
(7) Stankovich, S.; Dikin, D. A.; Piner, R. D.; Kohlhaas, K. A.; Kleinhammes, A.; Jia, Y.; Wu, Y.; Nguyen, S. T.; Ruoff, R. S. *Carbon* **2007**, *45*, 1558–1565.
(8) Li, D.; Müller, M. B.; Gilje, S.; Kaner, R. B.; Wallace, G. G. *Nat. Nanotechnol.* **2008**, *3*, 101–105.
(9) Dreyer, D. R.; Park, S.; Bielawski, C. W.; Ruoff, R. S. *Chem. Soc. Rev.* **2010**, *39*, 228–240.
(10) Worsley, M. A.; Pauzauskie, P. J.; Olson, T. Y.; Biener, J.; Satcher, J. H.; Baumann, T. F. *J. Am. Chem. Soc.* **2010**, *132*, 14067–14069.
(11) Wu, Z.-S.; Sun, Y.; Tan, Y.-Z.; Yang, S.; Feng, X.; Müllen, K. *J. Am. Chem. Soc.* **2012**, *134*, 19532–19535.
(12) Yang, X.; Cheng, C.; Wang, Y.; Qiu, L.; Li, D. *Science* **2013**, *341*, 534–537.
(13) Goldstein, A. P.; Mickelson, W.; Machness, A.; Lee, G.; Worsley, M. A.; Woo, L.; Zettl, A. *submitted* **2014**.
(14) Pierotti, R.; Rouquerol, J. *Pure Appl Chem* **1985**, *57*, 603–619.
(15) Yumitori, S. *J. Mater. Sci.* **2000**, *35*, 139–146.
(16) Yang, D.; Velamakanni, A.; Bozoklu, G.; Park, S.; Stoller, M. D.; Piner, R. D.; Stankovich, S.; Jung, I.; Field, D. A.; Ventrice, C. A.; Ruoff, R. S. *Carbon* **2009**, *47*, 145–152.
(17) Dimiev, A.; Kosynkin, D. V; Alemany, L. B.; Chaguine, P.; Tour, J. M. *J. Am. Chem. Soc.* **2012**, *134*, 2815–2822.
(18) Díaz, J.; Paolicelli, G.; Ferrer, S.; Comin, F. *Phys. Rev. B* **1996**, *54*, 8064–8069.
(19) Dimiev, A. M.; Alemany, L. B.; Tour, J. M. *ACS Nano* **2013**, *7*, 576–588.
(20) Rourke, J. P.; Pandey, P. A.; Moore, J. J.; Bates, M.; Kinloch, I. A.; Young, R. J.; Wilson, N. R. *Angew. Chemie Int. Ed.* **2011**, *50*, 3173–3177.
(21) Thomas, H. R.; Day, S. P.; Woodruff, W. E.; Valles, C.; Young, R. J.; Kinloch, I. A.; Morley, G. W.; Hanna, J. V; Wilson, N. R.; Rourke, J. P. *Chem. Mater.* **2013**, *25*, 3580–3588.
(22) Ferrari, A. C.; Robertson, J. *Phys. Rev. B* **2000**, *61*, 95–107.
(23) Meyer, J. C.; Kisielowski, C.; Erni, R.; Rossell, M. D.; Crommie, M. F.; Zettl, A. *Nano Lett.* **2008**, *8*, 3582–3586.

Chapter 6

Chemical Structure of Graphene Aerogels Following High-Temperature Annealing and Chemical Conversion to Boron Nitride

6.1 Thermal reduction of GO-based aerogels

The extent of oxygenation in 2D carbon materials is a key factor in determining their electronic, mechanical and structural properties.[1] In the previous chapter, we described several methods of chemical reduction that use solution-phase reactants to remove oxygen from a sample of graphene oxide (GO). Reduced GO is more conductive than as-made GO, so it is often studied as an analogue for graphene, but the residual oxygen present will impact the measured properties. Caution should be taken to characterize the amount of oxygen remaining in the material as a measure of its true similarity to graphene.

Thermal annealing has been shown by many to be a highly effective strategy for removing most of the oxygen from a carbon sample.[2–5] Requiring high temperatures would make the reduction process prohibitive for cheap, large-scale processing, but thermally annealed GO may ultimately be necessary for applications that require maximizing conductivity. W. Gao *et al.* showed that a process of sequential chemical reduction and thermal annealing resulted in a graphitic 2D material with as low an oxygen content as bulk graphite, ~0.5%.[4] Favorable mechanisms for removal of hydroxyl and carboxyl functional groups (-OH and COOH) during thermal deoxygenation have been shown in calculations by X. Gao *et al.*[3] However, Bagri *et al.* showed that removal of epoxy groups leaves holes in the reduced GO sheet via loss of CO and CO_2,[5] so if an intact graphene sheet is to be obtained by reduction of GO, the chemical pathway should be carefully considered.

In this chapter, we show the effect of annealing at high temperatures in an inert atmosphere on GO-based aerogels. In most cases, samples were annealed by heating to 1050 °C in a tube furnace under nitrogen flow for 2 hours. Some samples were heated under similar conditions to 1600 °C. Samples were covered in a graphite foil before annealing (Graftech GTA 3333), in order to prevent reaction between the carbon sample and the silicon in the quartz tube. Annealing aerogels increased the mesopore surface area dramatically, as measured by nitrogen porosimetry; for one representative sample, the surface area nearly doubled after annealing, going from 600 to 1160 m^2/g. Furnace ramping rate appears to have no effect on the change surface area.

6.1.1 Transmission electron microscopy (TEM) on annealed aerogels

In order to understand the structure of the annealed gels in greater detail, aberration-corrected TEM data were collected at 80 kV on the TEAM I microscope at the National Center for Electron Microscopy (NCEM) at Lawrence Berkeley National Laboratory. For the aerogel annealed at 1050 °C, the images in Figure 6.1 show sheets of aerogel composed of few atomic layers of carbon. Unfortunately, there was excessive sample movement under the electron beam (possibly due to *in situ* reduction of residual oxygen), so it was difficult to collect atomically-resolved images. High-resolution TEM was also performed on an aerogel that had been annealed at 1600 °C. This sample was much more stable under the beam, and the data are higher quality as a result. The difference in sample stability, though it prevents comparison of the two samples' atomic structure, is itself an interesting and useful change in the material.

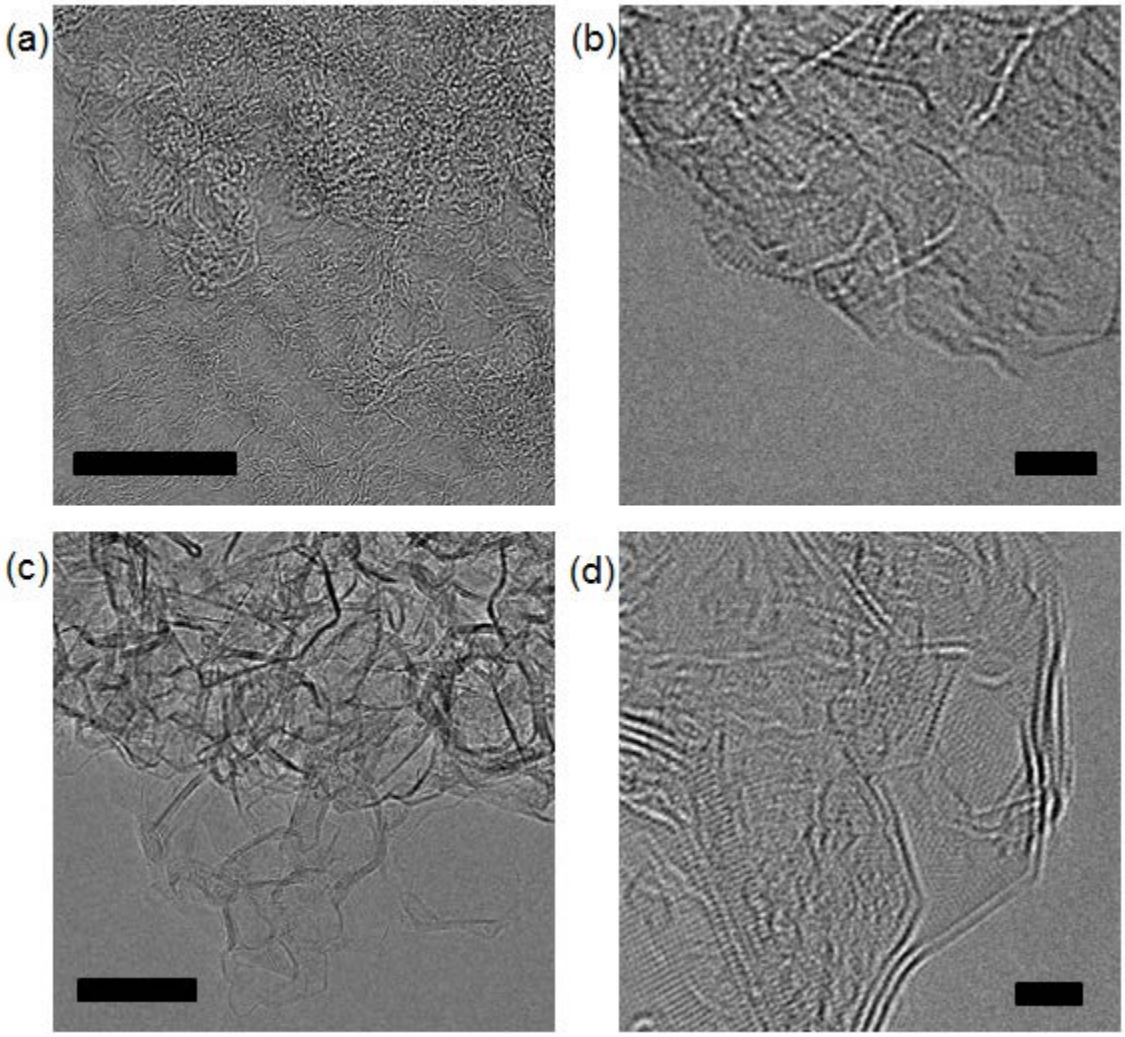

Figure 6.1. TEM images of a GO-based aerogel after annealing at (a, b) 1050 °C and (c, d) 1600 °C. Scale bars are (a, c) 20 nm and (b, d) 2 nm.

Comparing parts a and b to parts c and d of Figure 6.1, we see that the sheets of the higher-temperature annealed aerogel form longer, straighter lines, meaning that the atomic layers have become more crystalline and less defective. Some areas in both samples appear to be relatively flat sheets with atomic contrast like a graphene lattice, but it was not feasible to rotate the sample onto a zone axis using just a few atomic layers in a 3D textured structure. Over all the images collected in the 1600 °C annealed sample, we measure a range of angles formed wherever two sheets met at a sharp junction. These angles measured between 107° and 156°, but these values are likely not the true angles between sheets. To measure the correct angle in a junction, both sheets would need to be aligned parallel to the electron beam. However, each TEM image only captures a small cross-section of the sheet in the imaging plane, so we cannot say that any particular sheet is parallel to the electron beam. In fact, some regions of the aerogel change in appearance with very small changes of the microscope's focal conditions, indicating that the atomic layers within the sheet are still somewhat disordered on the nanometer scale.

Beyond annealing in an inert environment such as Ar or N_2, there is also evidence that annealing with hydrogen gas creates a more strongly reducing environment for GO.[5] We attempted to demonstrate this effect experimentally using *ex situ* heating of a TEM grid containing GO-based aerogel fragments. One challenge in this experiment was the use of holey Si_3N_4 membrane from Ted Pella, which is 200 nm thick and has 2.5 μm diameter holes. The regularly-spaced holes were ideal for sample mapping, but the membrane is non-conductive and appears to charge significantly at high magnification under electron illumination. Charging disturbs the aerogel sample and prevents imaging above 15,000X. This challenge was overcome by sputtering a few nm of Pt onto the membrane to provide a conducting pathway to the TEM holder; with the Pt-coated membrane, we were able to image up to 300,000X.

The results shown in Figure 6.2 are of an aerogel that had been previously annealed in N_2 at 1050 °C and was then subjected to annealing in H_2 at 400 °C. At lower magnification, no changes are apparent. Some small changes in the placement of the atomic layers are observed at higher magnification, though it is difficult to say whether these changes could be due to small rotations or differences in focal conditions between imaging sessions. We conclude that the physical structure of the aerogel is not significantly altered by these conditions. More research in this direction should be pursued in order to directly observe the reduction process in a single location, which necessitates a TEM substrate that can withstand the high temperature (>1000 °C) reducing environment.

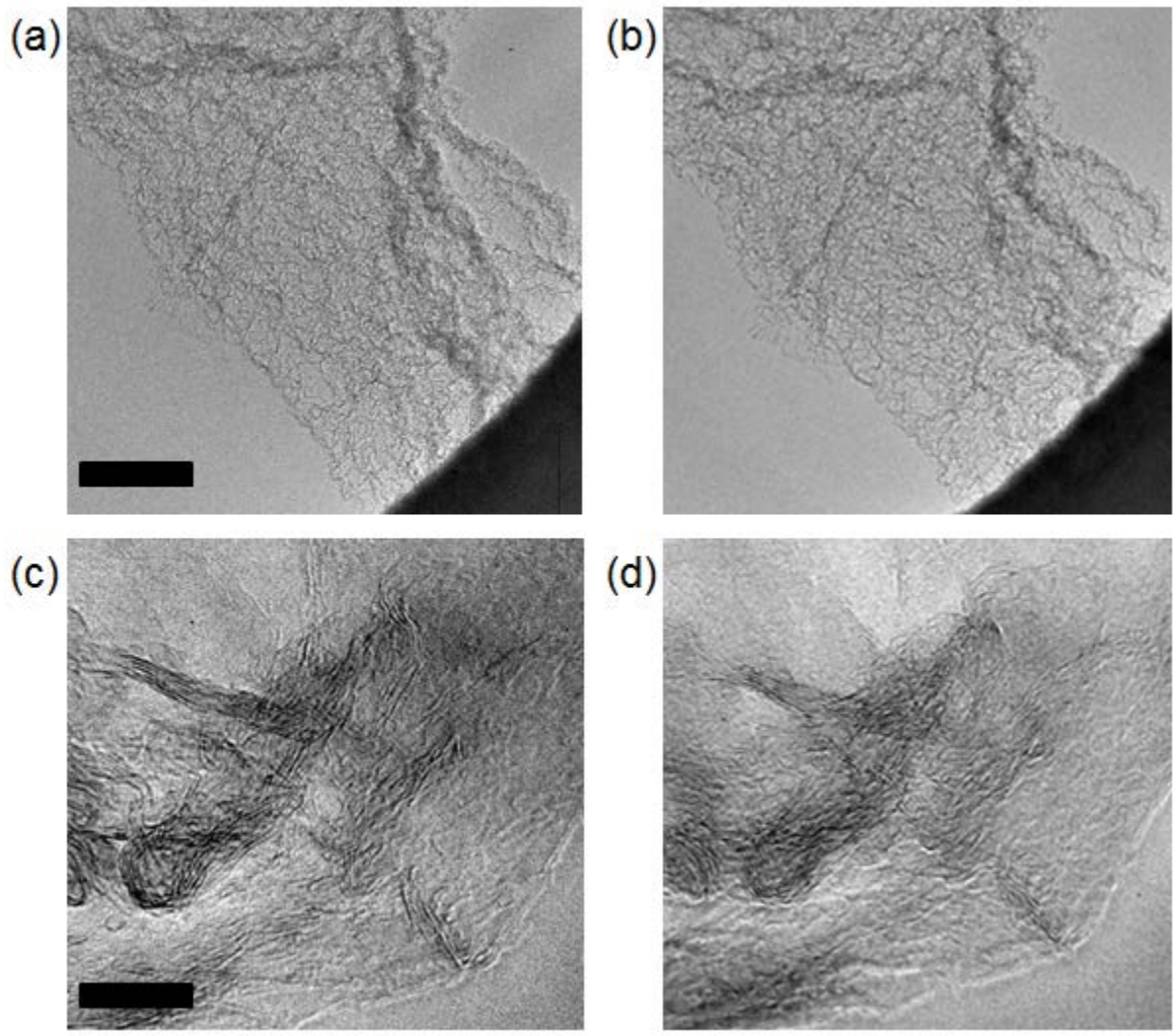

Figure 6.2. TEM images of GO-based aerogels (a) before and (b) after annealing in hydrogen gas at 400 °C for 4 hours. Higher magnification TEM images were obtained for another region (c) before and (d) after annealing in hydrogen gas at 400 °C for 1 hour. Scale bars are (a, b) 200 nm and (c, d) 10 nm.

6.1.2 Deoxygenation during annealing

We have used evidence from several experimental techniques to show that gelation entails significant deoxygenation.[6] These experiments were repeated here for the annealed aerogels. We find from XPS and UV-vis data that thermal annealing of the aerogel causes deoxygenation to progress further. Both trends observed in the evolution of the optical properties during gelation of GO are further developed following thermal annealing, as seen in Figure 6.3. The UV-vis absorption spectrum becomes very flat, and the peak absorption is red-shifted to ~270 nm, matching the spectrum of chemically-reduced GO.[7] Additionally, in the XPS spectra shown in Figure 6.4, there is some loss of signal across the entire carbon-oxygen bonding region (~286-290 eV) after annealing, though the change is less dramatic than was seen in the gelation step.

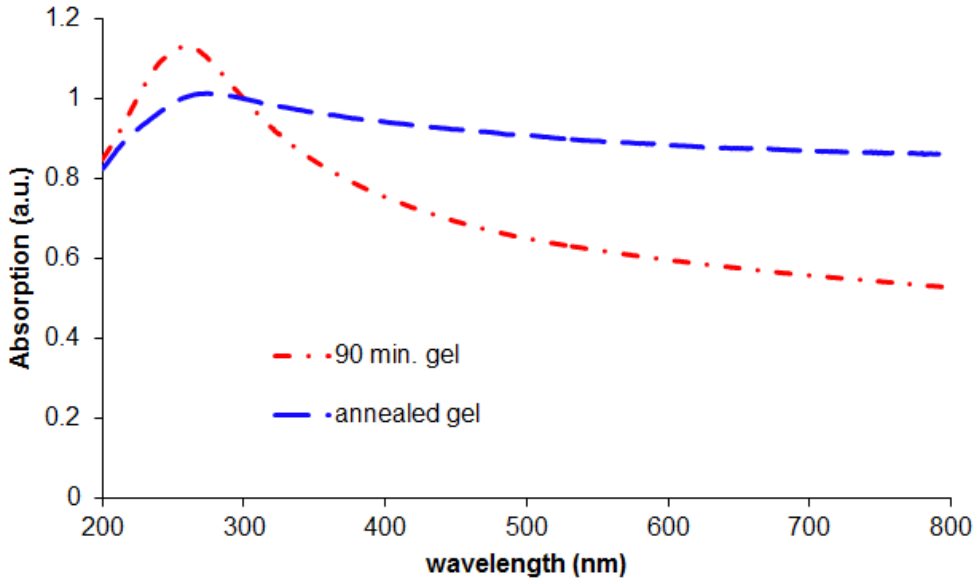

Figure 6.3. UV-vis spectra of a GO-based aerogel before and after annealing at 1050 °C. Samples were dispersed in water by sonication for 2-3 minutes. Spectra are normalized at 300 nm.

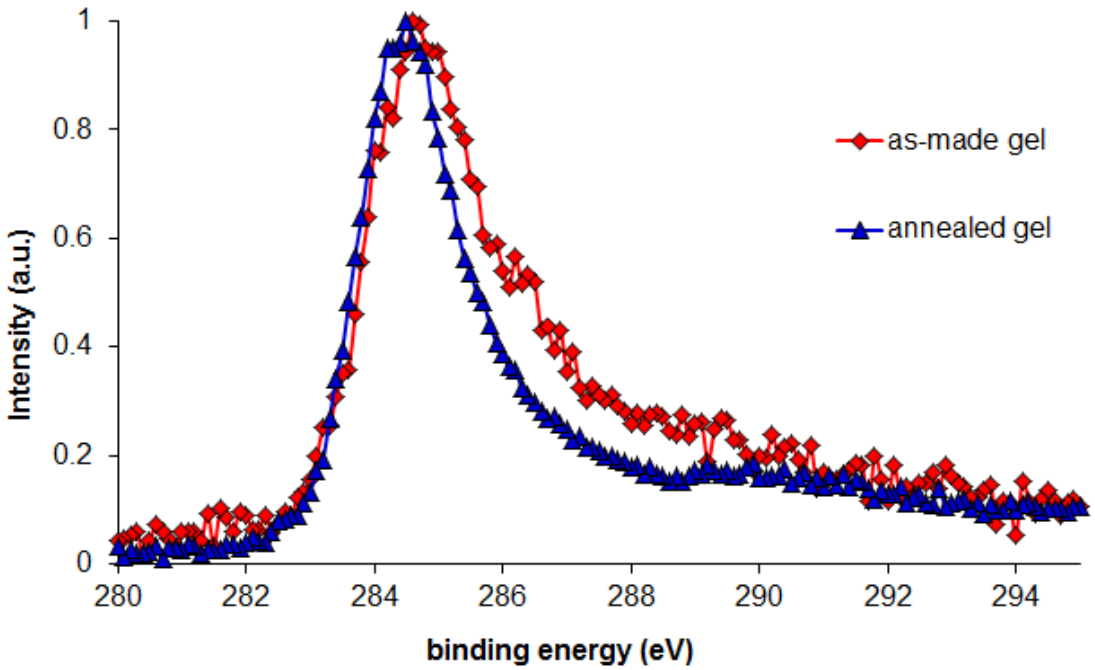

Figure 6.4. XPS data for an as-made aerogel and an aerogel annealed at 1050 °C. Spectra are normalized at the maximum signal and baseline subtracted. Data for as-made gel are the same as those presented in Figure 5.4b

XPS data were used in Chapter 5 to demonstrate that sp^2 bonding in the GO sheets increases after gelation. After annealing, we see from the XPS data in Table 6.1 that sp^2 bonding has further increased, based on the three signature effects:

i. The growth of the 2nd graphitic peak for the annealed gel
ii. A shift to lower energy of the graphitic peaks
iii. The increasing proportion of π-π^*.

The C/O ratio calculated for the aerogel after annealing at 1050 °C is 11.5, which is a surprising increase over the C/O ratio of the as-made aerogel, compared to the relatively subtle difference in the shape of the C1s peak for these samples. It should be noted that for the fired aerogel, we do not obtain a fit that includes a component for single-bonded C-O, though the absence of these functional groups after firing has not been explained. We also find that the C/O ratio calculated for the annealed sample from the components of the C1s peak fitting is not a good match for the ratio calculated from the C1s and O1s integrated peak intensities. As described in Section 5.4, these measurements suffer from several sources of uncertainty and are most useful for relative comparisons.

		As-made gel		Annealed gel	
Assignment	Expected Range[a] (eV)	Energy (eV)	Area	Energy (eV)	Area
C-C (1)	*284.5-285.0*	284.5	49.8%	284.3	43.1%
C-C (2)	*285.2-285.9*	285.4	11.9%	285.2	42.3%
C-O	*285.8-286.7*	286.3	7.5%	--	--
C=O	*287.0-288.0*	287.0	9.5%	287.6	5.8%
O-C=O	*288.5-290.0*	288.8	16.5%	289.4	2.8%
$\pi-\pi^*$	--	292[b]	4.7%	290.9	5.9%
C 1s/ O1s atomic ratio		3.2		11.5	
C/O ratio from C1s fit[c]		1.9-2.1		8.2	

Table 6.1. Selected XPS fitting parameters from the C1s peak of aerogel samples before and after annealing at 1050 °C. a: From Yumitori.[8] b: Peak was constrained due to noise in the high energy region. Area totals may not add to 100% due to rounding error. c: The lower and upper limits are given here by assuming that the C-O peak is due to hydroxyls and epoxides/ethers, respectively. Data for as-made gel are the same as those presented in Table 5.2.

6.1.3 Electronic and vibrational changes

The electron energy-loss spectrum (EELS) of the aerogel before and after annealing gives us insight into the changing electronic environment of the carbon atoms. EELS data were collected using a FEI Tecnai TEM equipped with a Gatan Imaging Filter and operating at 200 kV. Comparing the C-K region of the spectra, beginning with the π* peak at 284 eV in Figure 6.5, we see that the annealed aerogel has sharper features than the as-made aerogel. This is exactly the opposite of the spectral evolution observed during amorphization of graphite.[9] Additionally, the EEL spectrum of the as-made aerogel displayed a small peak from the N-K edge, because this sample's gelation was catalyzed by NH_4OH in the low-temperature method described in Chapter 5. This peak disappears after annealing, indicating that N is also lost from the aerogel during thermal reduction.

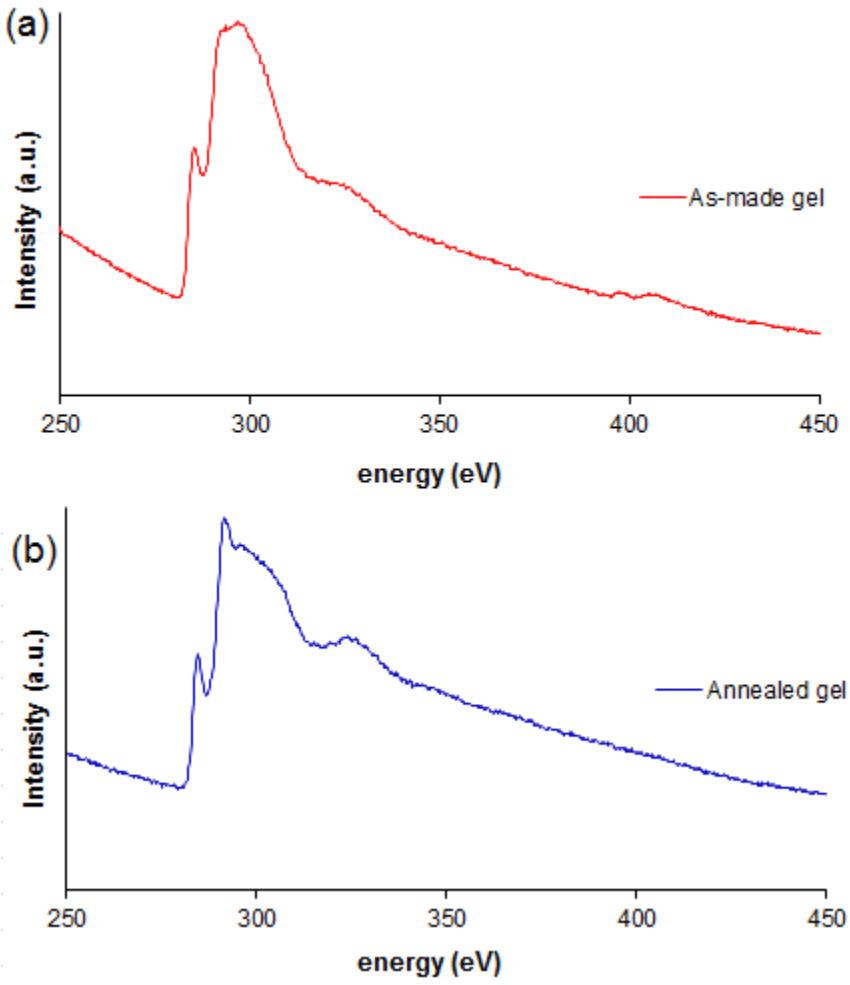

Figure 6.5. C-K edge of the EEL spectrum GO-based aerogels (a) before and (b) after annealing at 1050 °C.

Annealing also has a drastic impact on the vibrational properties of the GO-based aerogel. After annealing at 1050 °C, the Fourier transform infrared (FTIR) spectrum of the aerogel (data not shown) is completely featureless in the 700-4000 cm^{-1} region, as would be expected for a completely graphitic sample.[10] All peaks associated with C-O bonding have disappeared, corroborating the evidence above for deoxygenation. However, the Raman spectrum does not change dramatically after annealing at 1050 °C, as shown in Figure 6.6. Annealing increases the I_D/I_G ratio from 0.83 to 0.95, but the rest of the spectrum remains identical. Based on this minimal impact on the Raman spectrum, we conclude that the removal of oxygen at at 1050 °C does not facilitate the propagation of phonons through the carbon sheets.

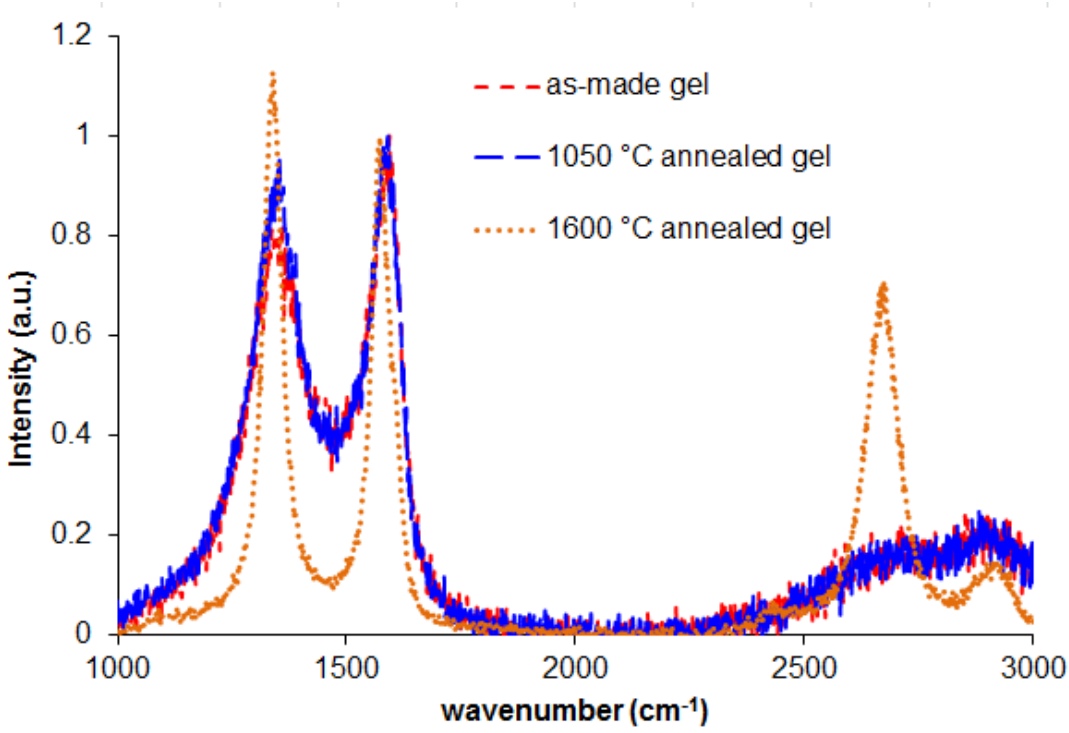

Figure 6.6. Raman spectra of graphene oxide and aerogels exposed to various annealing conditions. Spectra are background subtracted and normalized to the G peak.

Annealing at 1600 °C, on the other hand, has several notable effects: the D and G peak are red-shifted, the D and G peak become narrower, the I_D/I_G ratio increases significantly to 1.13, and the 2D peak becomes much more prominent.[11] The increase in I_D/I_G ratio is likely due to a departure from the Tuinstra-Koenig relation at high levels of disorder. Contrary to the expectation for single-crystal graphene, in this case, increasing the size of sp^2 domains actually enhances the height of the D peak for nanocrystalline domains. We conclude, therefore, that even at 1050 °C and above, the extent of reformation of the sp^2 network in the carbon sheets depends heavily on the annealing temperature.

6.2 Carbothermal conversion to boron nitride

BN-based structures, despite being isoelectronic with carbon, have not gained adequate attention.[12] The ionic bonding of boron and nitrogen makes sp^2-bonded BN an insulator, regardless of its crystal structure.[13] Additionally, BN-based structures exhibit comparable mechanical strength and thermal conductivity to carbon materials, but with a much higher oxidation temperature.[13] The similarity in structure and properties make sp^2-BN an alternative and complementary material for carbon-based nanostructures, a number of which were reviewed by Golberg and co-workers.[14] However, the complexity of the chemistry, the need for hazardous precursors, and the high-temperature synthesis have somewhat hindered the production and application of BN-related structures.[15–17]

6.2.1 Mechanism for conversion of C to BN

Han *et al*. first presented the conversion of carbon to boron nitride in nanotubes by carbothermal reduction.[18] Using reference values for the heats of formation and entropies of formation for reactants in Table 6.2, we calculate the thermodynamics of three possible reactions for carbothermal synthesis of BN from B_2O_3. Reaction I is favored in entropy, but enthalpically uphill. The situation is reversed for Reaction II: favored in terms of enthalpy, but not entropy. In terms of ΔG, CO formation is thermodynamically favorable (exergonic) at all temperatures above 29 K. CO_2 formation, on the other hand, becomes less favorable with higher temperature; Reaction II is not favored above 1421 °C. Because our synthesis takes place at or above 1600 °C, we suppose that Reaction I is the operative mechanism. A third reaction, III, is simply the difference between the two previous reactions: II-I. Reaction III is the oxidation of CO by B_2O_3 to form CO_2, and could be concurrent with (a) by consuming the CO produced; however, Reaction III itself is not exergonic above 942 °C.

	Reaction	ΔH^o (kJ/mol)	ΔS^o (J/mol·K)	T where $\Delta G < 0$ (°C)
I	B_2O_3 (g) + 3 C (s) + N_2 (g) → 2 BN (s) + 3 CO (g)	3.5	121.7	> 244
II	2 B_2O_3 (g) + 3 C (s) + 2 N_2 (g) → 4 BN (s) + 3 CO_2 (g)	-510.5	-301.4	< 1421
III	B_2O_3 (g) + 3 CO (s) + N_2 (g) → 2 BN (s) + 3 CO_2 (g)	-514	-423.1	< 942

Table 6.2. Three possible chemical reactions that produce boron nitride from a carbon precursor exposed to boron oxide vapor, and their associated change in enthalpy and entropy. Values were calculated from standard enthalpies and entropies of formation from the CRC Handbook.[19]

According to the mechanism proposed by Golberg *et al.*, the boron oxide vapor and nitrogen gas react to gradually substitute carbon atoms for boron an nitrogen, forming areas of pure BN amidst graphitic carbon regions.[20] The isoelectronic properties of BN and C, and the high diffusion rate due to high synthesis temperature, ensure the maintenance of both micro- and macroscopic structures after conversion. Several BN structures have been successfully synthesized so far by carbothermal conversion, including aligned BN nanotubes,[21] activated BN,[22] and BN sheets.[23] Previous studies on the conversion of BN nanotubes and sheets have offered little information about the change in crystal structures and bonding after the conversion.

6.2.2 Synthesis of BN aerogels

We previously reported the successful synthesis of boron nitride aerogels from graphene aerogels.[24] (The term "graphene aerogel" lacks clarity when used to refer to an aerogel as-made from GO, so we use it here only to refer to an aerogel which has been previously annealed to at least 1050 °C.) The as-prepared BN aerogels have high surface area, mesopores, high crystallinity and high chemical purity. Representative TEM images of the BN aerogel are shown in Figure 6.7. TEM was performed on a JEOL 2010 microscope at 80 kV.

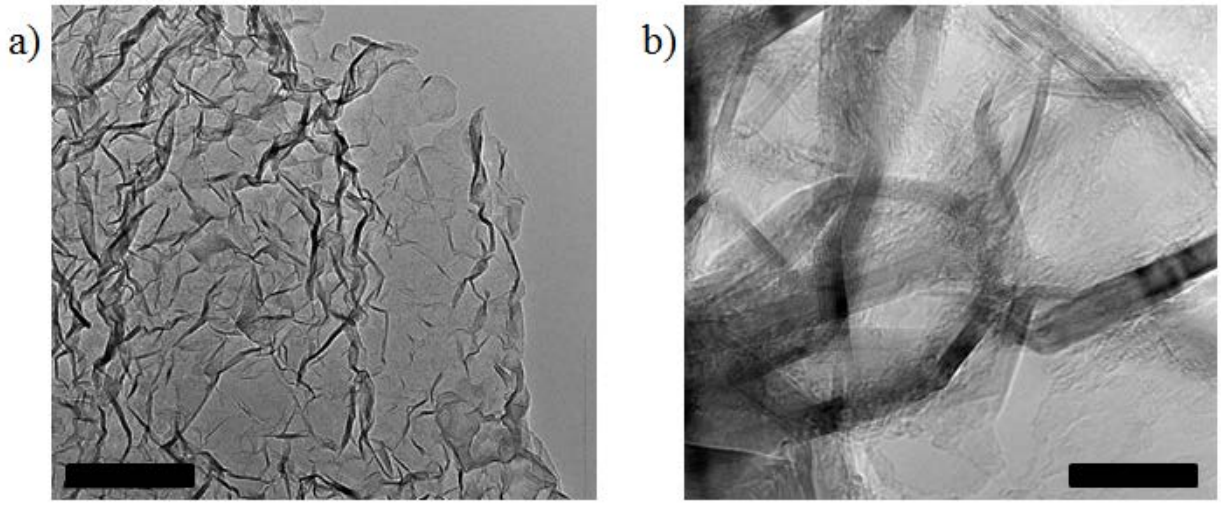

Figure 6.7. Low-magnification TEM of BN aerogel, showing the pores formed by the crystalline BN sheets. Scale bars are (a) 200 nm, and (b) 20 nm.

Compared to other methods of carbothermal conversion, our unique separation of the boron oxide source and carbon materials prevents the collapse of pores from capillary effects. In our synthesis of sp^2-bonded BN aerogels, boron oxide powder (Alfa Aesar) is loaded into a cylindrical graphite crucible. The graphene aerogels, synthesized by a previously published method,[25] are placed in the middle of the crucible in a separate graphite sample holder. The

center and the bottom of the sample holder are perforated with small holes to ensure the adequate flow of reactant vapors. The crucible is then heated to 1600-1800 °C by a radio frequency induction furnace under 2000 sccm flow of N_2 gas. The N_2 gas is directed through a center tube to the bottom of the crucible, where it mixes thoroughly with boron oxide vapor before flowing upward to react with the graphene aerogels. Our earlier work includes more synthetic details, including a schematic of the reaction chamber.[24]

To better understand this unique material, the crystal structure and the chemistry of the BN aerogels have been systematically investigated and compared to the parent graphene aerogels.[26] BN can be synthesized in a variety of crystal structures, including cubic, wurtzite, and hexagonal (h-BN). A lesser-known structure is rhombohedral (r-BN), which has the same 2-dimensional sp^2-bonded atomic layers of h-BN, but with a different registry between the layers, as seen in Figure 6.8. Another related structure is turbostratic BN (t-BN), which has no particular ordering between the atomic layers. In the next section, we attempt to identify the relationship between BN layers in the aerogels after conversion.

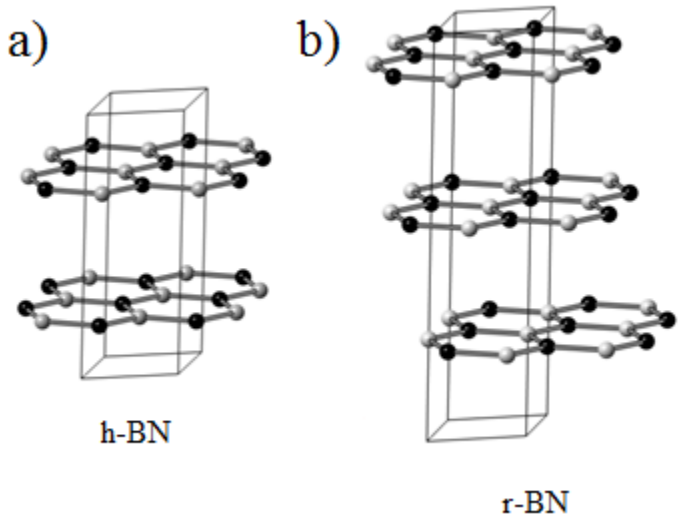

Figure 6.8. Selected atoms from crystal structure models of (a) hexagonal BN and (b) rhombohedral BN, where boron atoms are black and nitrogen atoms are white.

6.2.3 Chemical structure of BN aerogels

For graphitic carbon materials, X-ray diffraction (XRD) has been useful for characterizing the size of the crystallites, the fluctuation in the interlayer spacing, and the curvature of the layers.[27] Here, we use XRD to identify the crystal structure of our BN aerogel and compare with the graphene aerogel. Powder XRD patterns were collected on a Bruker D8 Advance diffractometer with Cu-Kα radiation. The BN aerogel displays an XRD pattern that is indicative of t-BN, as shown in Figure 6.9.[28,29] The XRD pattern shows only two features: one broad peak centered around 25.8° corresponding to an expanded interplanar spacing of ~3.45 Å between layers, and another broad, tailing peak with its maximum at 41.5° indicating $\{10\bar{1}0\}$ planes.[30] The absence of a distinct $\{10\bar{1}1\}$ peak, which would be expected for h-BN at 43.8°, indicates that there is no

large-scale order in the relative orientation of BN layers in the aerogel. In comparing the BN aerogel to its precursor material, we see that graphene aerogels have significantly broader XRD peaks, characteristic of an amorphous material.[25,31,32] This difference in XRD features illustrates the increase in crystallinity that occurs in the aerogel following conversion, as observed previously via TEM showing reduced curvature in the BN sheets.[24]

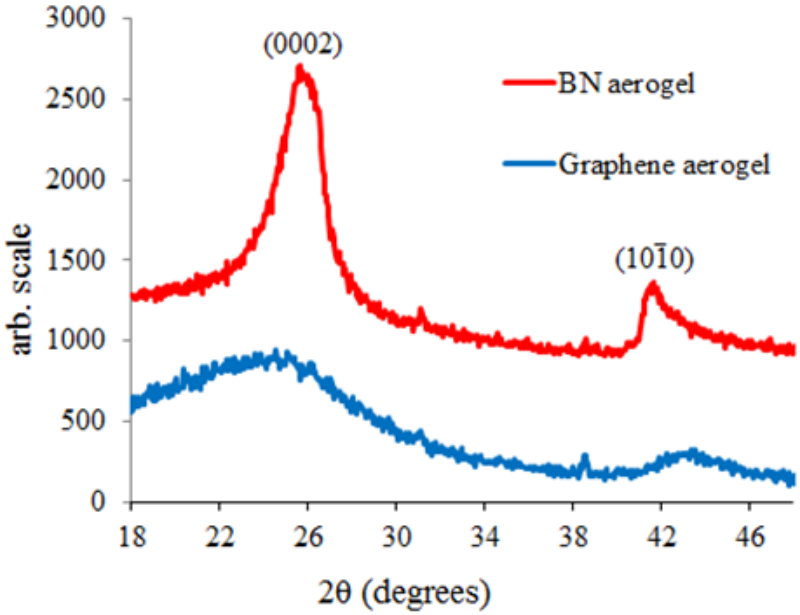

Figure 6.9. XRD patterns of graphene aerogel (blue line) and BN aerogel (red line).

Nuclear magnetic resonance (NMR) was also used to probe the bonding of boron and nitrogen atoms in the BN aerogel. All ^{11}B solid state NMR analyses were carried out on a Bruker Avance III NMR spectrometer operating at a 600 MHz ^{1}H Larmor frequency and using a Bruker 1.3mm Very Fast Magic Angle Spinning (MAS) broadband – ^{1}H/D probe. 10 mg samples were powdered and packed into 1.3 mm zirconia rotors. ^{11}B spectra were obtained using a standard solid echo sequence optimized for ^{11}B with at sample spinning rates of 55 kHz, using a 90° pulse length of 1 μs at 10 Watts and a recycle delay of 10 seconds. All ^{11}B spectra were referenced to a trimethylborate (TMB) standard. For comparison with the BN aerogel, h-BN powder with a purity of >99% was obtained from M K Impex, Canada.

From the ^{11}B NMR data in Figure 6.10, we see that the electronic environment of the boron is very similar to that of the h-BN control sample, *i.e.* a single repeating BN_3 unit structure, as evidenced by the similar line shapes and chemical shifts of 24.1 and 22.1 ppm in the BN aerogel and h-BN control respectively. These features are consistent with those reported by Marchetti *et al.* for BN.[33] In conjunction with the XRD data, which show that the BN sheets are not necessarily composed of hexagonally stacked atomic layers, it appears that the ^{11}B NMR trace is only sensitive to the in-layer bonding and not to the registry between adjacent layers.

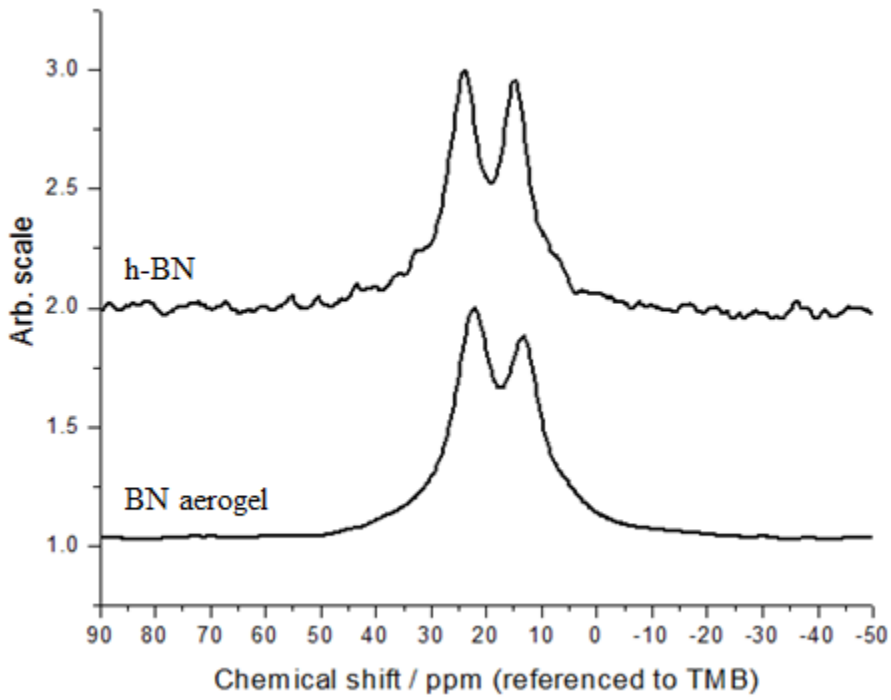

Figure 6.10. Stack plot showing the solid-state ^{11}B NMR spectra of h-BN and the BN aerogel.

In order to better understand the stacking relationship between atomic layers, the BN aerogel was further characterized by aberration-corrected TEM. Aberration-corrected TEM images were collected using the TEAM I microscope at NCEM operating at 80 kV. TEM images such as the one shown in Figure 6.11a contain many areas where the sheets lie parallel to the beam and a Moiré pattern is observed due to the overlapping atomic layers. There are also many areas where the sheets are perpendicular to the electron beam, which appear as bright lines of alternating contrast. Both orientations give new information regarding the crystal structure of BN in the as-made aerogel.

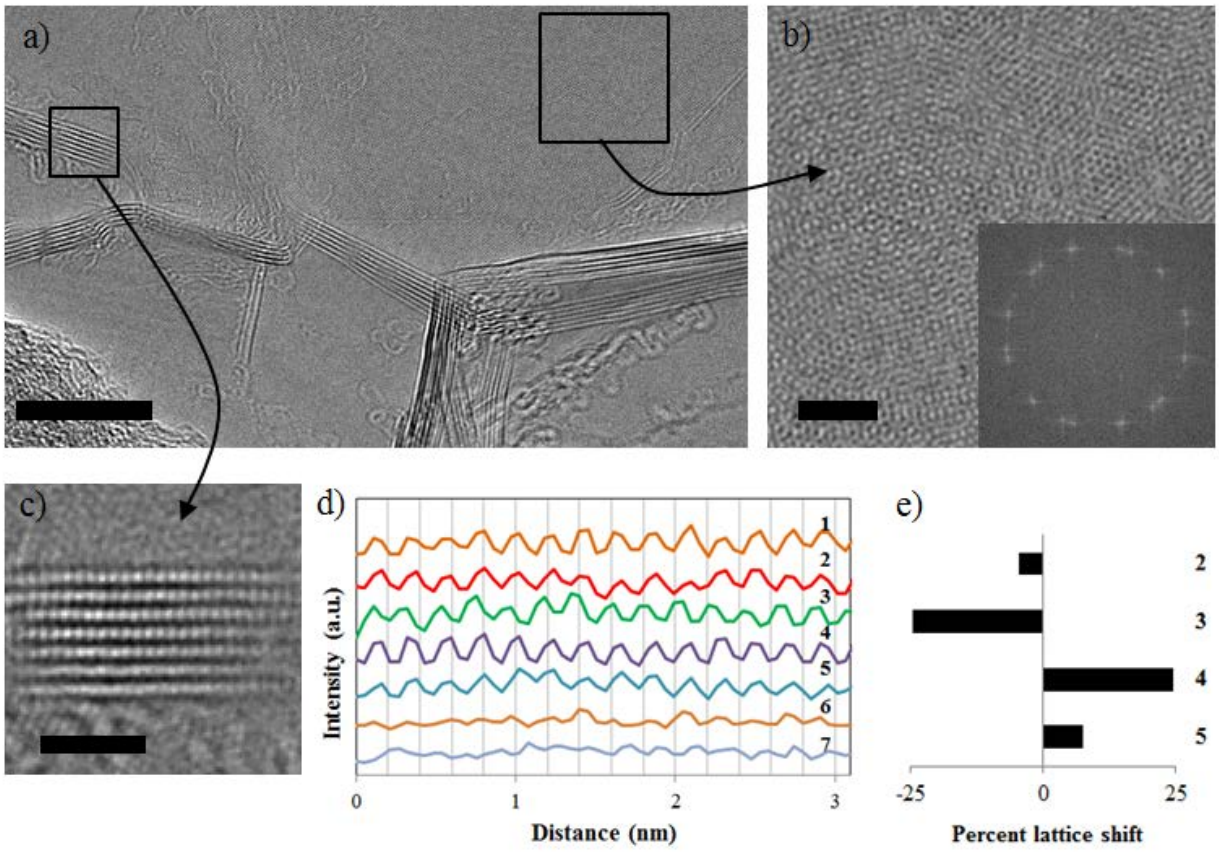

Figure 6.11. (a) High-resolution TEM of a portion of BN aerogel and (b) a magnified region of the image in part a, showing a portion of BN sheets lying parallel to the imaging plane. Inset: FFT of this region. (c) Another magnified region of the image in part a, where the BN layers lie perpendicular to the imaging plane. (d) Plot of gray scale intensity through the center of each of the layers in part c, and (e) the average shift in register of layers 2-5 each relative to the layer above it. Scale bars are 10 nm (a) and 2 nm (b, c).

As shown in Figure 6.11b, there are sheets perpendicular to the beam where we find that the atomic layers of BN have no particular relationship to each other in terms of their rotation. A fast Fourier transform (FFT) of the cropped image shown in Figure 6.11b results in a ring of 5 distinct hexagonal spot patterns, with a spacing of 0.22 nm. This distance corresponds to the $\{10\bar{1}0\}$ spacing of a single sp^2-bonded BN layer. The angles between these spot patterns appear to be arbitrary (relative to one chosen spot, the other four appear at 2°, 31°, 34°, and 39°). The analysis of Figure 2b is representative of results from other segments of BN aerogel. For additional examples of rotational misorientation among layers of BN, see Figures 6.12 and 6.13. There are also some sheets that display only a single hexagonal pattern, due to the ordered stacking of h-BN (Figure 6.14). However, almost all the analyzed segments of aerogel displayed a concurrence of multiple spot patterns, which suggests t-BN and corroborates our findings from XRD.

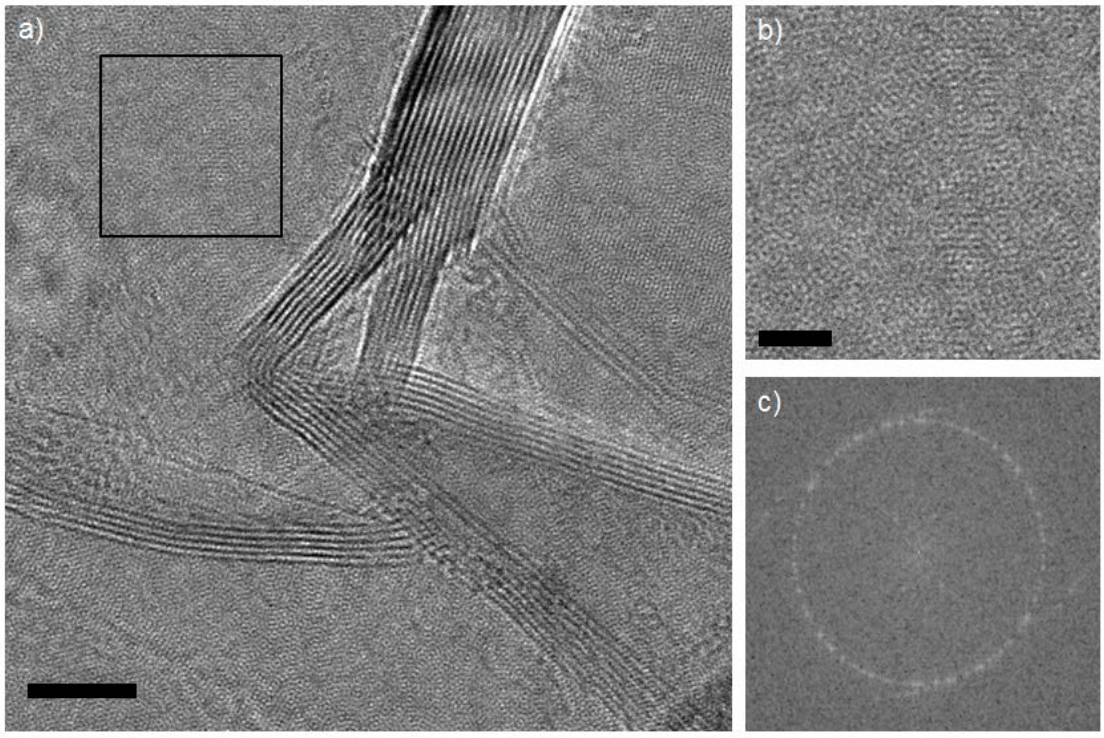

Figure 6.12. (a) TEM of a portion of BN aerogel and (b) a magnified region of the image in part a, showing a portion of BN sheets lying parallel to the imaging plane. (c) FFT of this region with at least 10 overlapping hexagonal spot patterns. Scale bars are (a) 5 nm and (b) 2 nm.

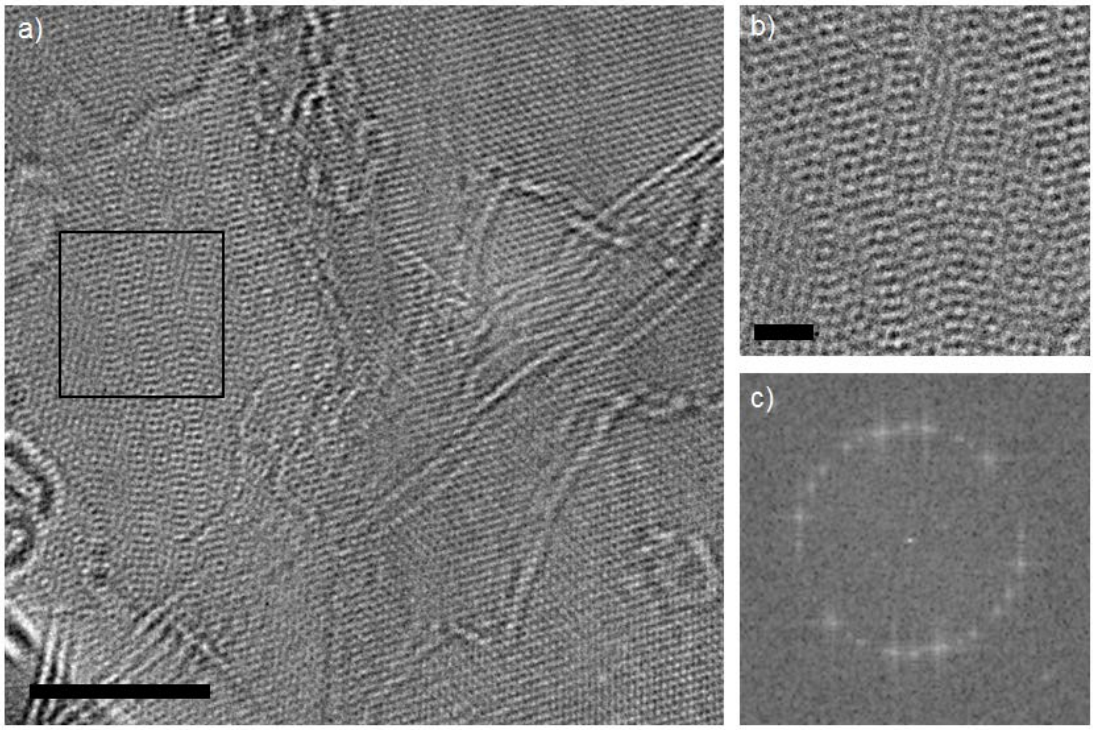

Figure 6.13. (a) TEM of a portion of BN aerogel and (b) a magnified region of the image in part a, showing a portion of BN sheets lying parallel to the imaging plane. (c) FFT of this region with at least 5 overlapping hexagonal spot patterns. Scale bars are (a) 5 nm and (b) 1 nm.

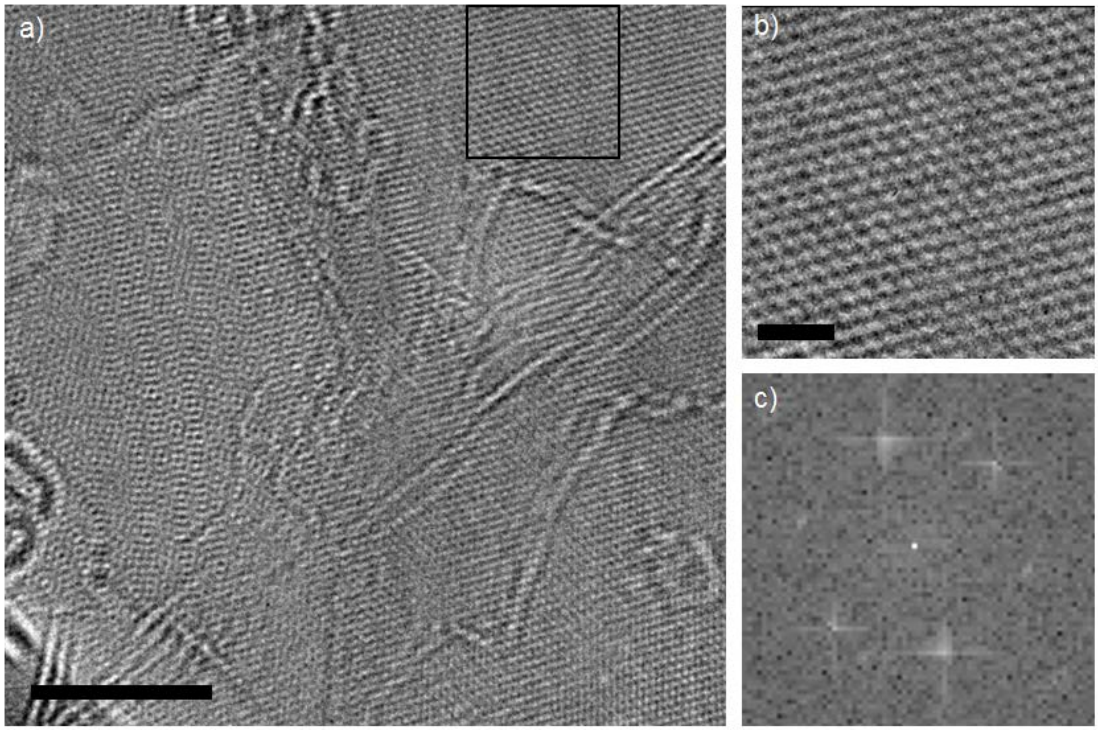

Figure 6.14. (a) The same TEM image from Figure 6.13 and (b) a different magnified region of the image. (c) FFT of this region with a single hexagonal spot pattern. Scale bars are (a) 5 nm and (b) 1 nm.

Analysis of a sheet that lies parallel to the electron beam, shown in Figure 6.11c, gives a different point-of-view on the relationship between BN layers. Of the seven layers visible in this sheet, the top five are well aligned with the electron beam and produce a high contrast pattern plotted in Fig. 6.11d. Based on the in-layer spacing of 0.21-0.22 nm for these five layers, we infer that the bright spots are overlapping stacks of B and N atoms in the same layer. Meanwhile, the two layers at the bottom of the sheet yield a low contrast pattern and cannot be assigned a lattice spacing. We conclude that these two sheets have a different rotational orientation from the other five, so they are not able to be atomically resolved at this viewing angle. This provides a side-on view of the rotational misorientation that is similarly observed in Figure 6.11b.

Because the top five layers in Figure 6.11c are oriented in the same rotation, we can use the register shift between them to understand the type of stacking present in this segment. In terms of atom placement in the hexagonal lattice, h-BN exhibits no shift between adjacent sp^2-bonded layers, whereas each adjacent layer of r-BN (Fig. 6.8a) is shifted by 33% of the lattice parameter in the $<10\bar{1}0>$ direction. The shifts observed between adjacent layers in this sheet are -2%, -25%, 27, and 11%, as shown in Fig. 6.11e, indicating no consistent translational relationship between the layers. This is further supporting evidence that the BN sheets are neither ordered h-BN nor r-

BN, but are in fact largely t-BN with different degrees of rotational and translational ordering across the sample. The reason for the lack of ordered stacking may be the large number of defects, including bent and folded sheets, which lock the layers into place and prevent them from shifting to minimize strain. Even a segment of perfect h-BN layers is almost certain to create a stacking fault across a bend in the sheet.

6.2.4 Physical structure of BN aerogels

In addition to characterizing its chemical structure, we have also analyzed the physical structure of the BN aerogel by resonant soft x-ray scattering (RSoXS). RSoXS is an x-ray scattering method using soft x-rays near the absorption edges that provide elemental/chemical sensitivity. It offers statistical information of morphological heterogeneity over a large sample area (100 μm × 100 μm) and covers a broad size scale (nm-μm). With polarized x-rays, RSoXS is sensitive to the molecular bond orientation, especially local molecular orientation that cannot be observed with other methods.[34–36]

RSoXS experiments were conducted at ALS BL11.0.1.2.[37] BN aerogel samples were sonicated briefly in isopropanol and dropcast on 100-200 nm silicon nitride membranes. The beam size was 100 um x 100 um. RSoXS data was collected in transmission geometry using an in-vacuum CCD camera using different photon energies near the Boron K-edge (~191 eV), Carbon K-edge (~285 eV) and Nitrogen K-edge (~400 eV). Both horizontally S and vertically P polarized x-rays were used to identify scattering anisotropy caused by the local molecular ordering. RSoXS data was reduced using SAXS analysis software Nika.[38]

The RSoXS data give new information on the size and composition of the aerogel's pores before and after conversion to BN. As shown in Fig. 6.15a, the graphene aerogel has a broad scattering feature centered at ~0.035 A^{-1}, which corresponds to a distribution of real space structure of 18 nm, and we assign this to the average wall-to-wall distance for the porous structure. The boron nitride shows a scattering feature at ~0.023 A^{-1}, which corresponds to an average wall-to-wall distance of 27 nm. The increased pore size for BN confirms our previous observations by TEM, as well as nitrogen adsorption porosimetry, wherein the isotherm for the BN aerogel displayed hysteresis at a higher relative pressure.[24] This expansion may be a consequence of the conversion mechanism,[23] wherein boron and nitrogen substitute for carbon. At high temperature, this substitution drives out atomic defects and increases crystallinity within the sheets. As the sheets become less wrinkled and more flat, the pores that they encase grow larger.

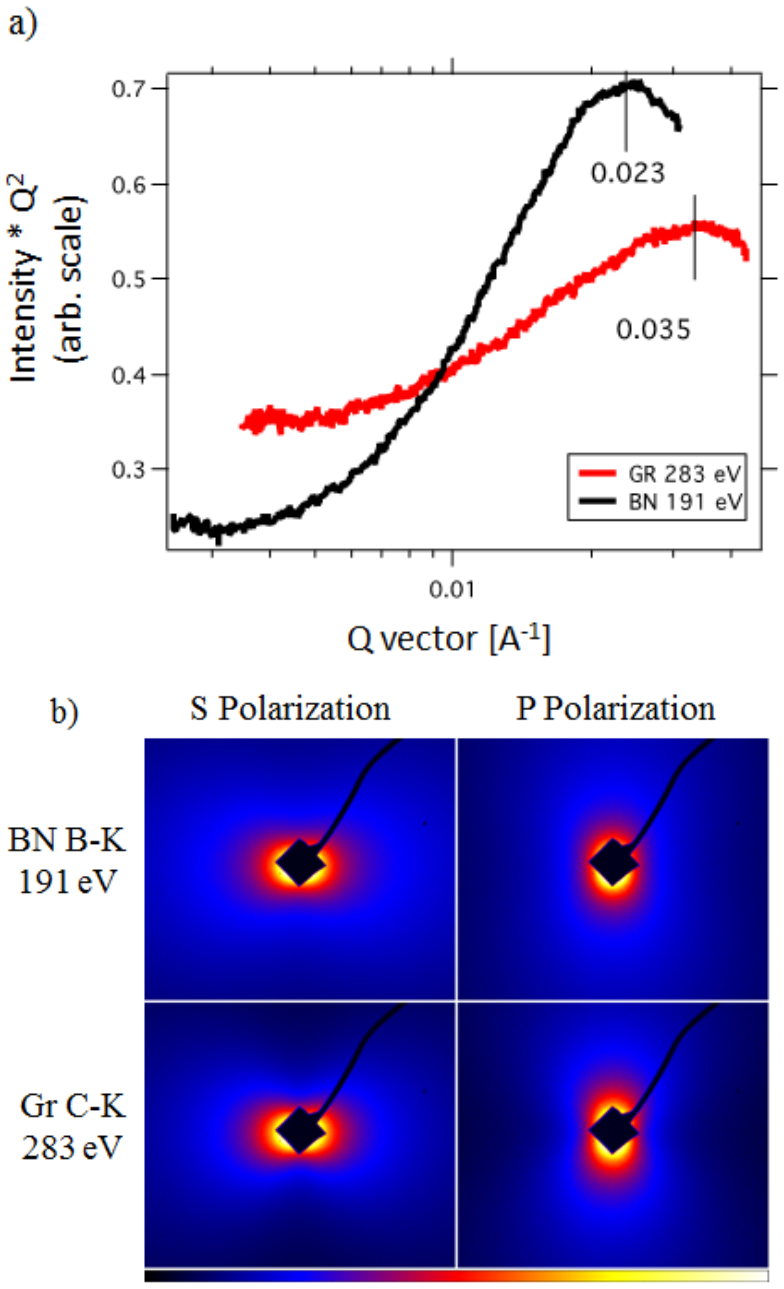

Figure 6.15. a) Soft X-ray scattering data for graphene (GR) and BN aerogels. The scattering peaks correspond to the pore size distribution. b) Scattering anisotropy of BN and graphene aerogels with polarized X-rays near the resonance energies.

Resonant scattering anisotropy was observed for all the samples near the absorption edges, seen in Figure 6.15b. This is an indication that an ordered molecular structure is present within the walls of the porous aerogel. The scattering contrast between the walls and the pores changes as a function of x-ray photon energy. For the BN aerogel, the scattering anisotropy was most significant near the boron K-edge (191 eV) and was also observed for the nitrogen K-edge. The strong 1s-π* resonance at ~191 eV does not appear in sp^3-bonded BN, thus demonstrating that

the BN in the aerogel is sp^2-bonded.[39] This result agrees well with the TEM and XRD data. For the graphene aerogel, the scattering anisotropy was visible near the carbon K-edge (285 eV), which is also from 1s-π^* resonance, while it is completely isotropic at the boron or nitrogen edges (data not shown).

An anisotropic response from RSoXS demonstrates that the atomic layers have a particular orientation relative to the vacuum-aerogel interface, i.e., the π orbital of the C-C or B-N bonds lies parallel to the vacuum-aerogel interface. The bonding environment of atoms in the aerogel is anisotropic along the surface of the pore, meaning that the graphene/BN layers are wrapped around the pore walls rather than being stacked perpendicular to the interface. The similarity between anisotropy of scattering for the BN aerogel and the graphene aerogel indicates that the placement of the 2D sheets with respect to the pores was preserved during conversion.

6.2.5 Mechanical and wetting properties of BN aerogels

To see how the converted structure of the aerogel impacts its physical properties, we performed nanoindentation measurements both before and after conversion to BN. Samples were indented at room temperature in the load-controlled mode in an MTS XP nanoindenter with a spherical sapphire indenter with a radius of 496 μm. A series of partial indents with multiple load-unload cycles (with complete unloading) were performed. Both loading and unloading rates were kept constant to maintain an indentation strain rate of 10^{-3} s^{-1}.[40] Young's modulus (E) and indentation stress (average contact pressure) were calculated based on the initial slope of the unloading curve according to the Oliver-Pharr method.[41] Indentation stress-strain curves were derived from spherical indentation load-displacement data as described previously.[40]

Figure 6.16 compares load-displacement curves and the corresponding indentation stress-strain curves for graphene and BN aerogels. It reveals that the BN aerogel is much more compliant than the graphene aerogel. Both aerogels are characterized by significant energy dissipation during the load-unload cycle. The BN and graphene aerogels have Young's moduli of 1.6 and 56 MPa, respectively. One explanation for the change in mechanical strength between the parent graphene aerogels and the converted BN aerogels is their difference in density. The graphene aerogel has a density of around 120 mg/mL and that of BN aerogel is 40 mg/mL. More void space in the aerogel means there is less material to resist indentation.

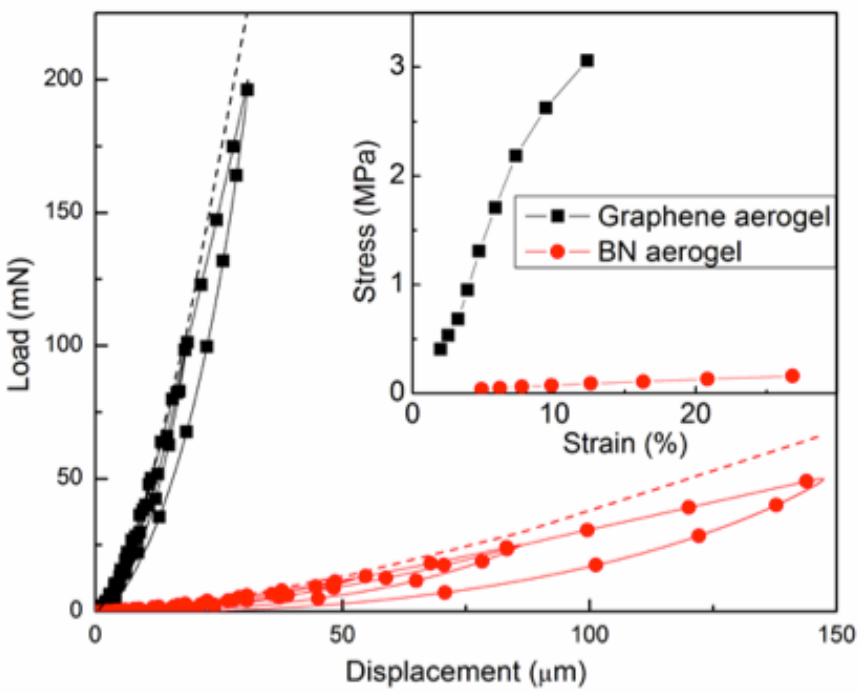

Figure 6.16. Representative load-displacement curves of graphene and boron nitride aerogels. For clarity, only every 100th experimental point is depicted. Dashed lines are fits with the Hertzian model. Inset: indentation stress-strain curves of the two aerogels.

In order to characterize the surface roughness for both annealed and converted aerogels, their wettability is measured. The contact angle measurement was carried out by static sessile drop method using a 10 μL drop of deionized water. Five different positions on each aerogel sample were examined using a Rame–Hart Model 290 Automated Goniometer equipped with DROPimage Advanced software. In each measurement, the static contact angle between the aerogel and the liquid droplet was computed by defining the interfaces of solid/liquid and liquid/vapor. Both angles from the left and the right sides of the droplet were measured and then averaged.

Before annealing, GO-based aerogels are easily wet by water, due to the residual oxygen present following gelation. Graphene and BN aerogels, on the other hand, resisted wetting. Graphene aerogels annealed at 1050 °C had a contact angle of 100°, and the converted BN aerogels are extremely non-wetting, with a contact angle of 155°, as presented in Figure 6.17. Materials with contact angle >150° are generally considered superhydrophobic. Experimental studies have shown that homogeneous h-BN films are quite hydrophilic,[42,43] due to the ionic character of the B-N bond, which enhances its interaction with polar water molecules. However, in our case, the BN material is not a flat film, so the observed hydrophobicity must come from factors other than its surface chemistry, such as the macroscopic roughness of aerogel surface. The texture of the graphene aerogel is also likely a determining factor in its wettability, since the contact angle of water on multilayer graphene is ~91°.[44]

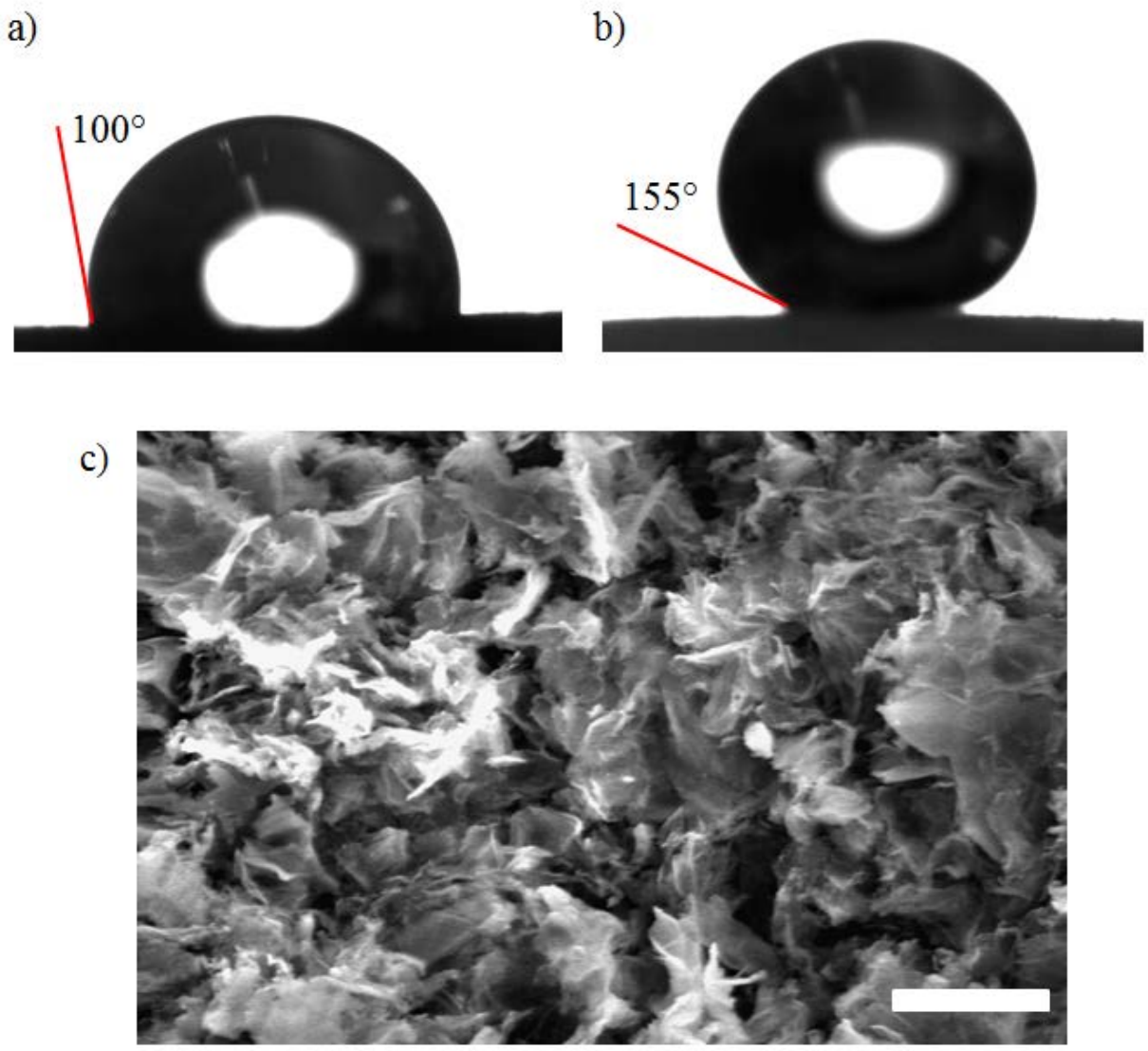

Figure 6.17. Contact angle measurements of a 10 μL droplet on samples of (a) graphene aerogel annealed at 1050 °C and (b) BN aerogel. (c) SEM of an exposed inner surface of the BN aerogel. Scale bar is 100 μm.

In the Cassie-Baxter model for surface wetting,[45] in which a water droplet can bridge the composite surface of BN aerogel sheets and air pockets created between, the relationship between contact angle and surface roughness is:[46]

Equation 6.1

$$\cos\theta_{CB} = f_s\,(1 + r \cdot \cos\theta_e) - 1$$

where f_s is the fraction of solid contacting the liquid, r is the roughness of wet area, which is the ratio of real surface area to geometric surface area, and θ_e is the contact angle for a flat surface, that is 51°-67° for BN.[42,43] According to Equation 6.1, the contact angle θ_{CB} will increase when f_s decreases. Thus the high contact angle for the aerogels can be attributed to a small fraction of

water and solid in contact. The gravimetric surface area of BN aerogels was found to be less than the graphene aerogel precursors,[24] so this model does not explain the increase in contact angle and emergence of superhydrophobicity following conversion to BN. More detailed research is needed into the changes in pore size and shape during conversion to understand the impact of conversion to BN on the wettability of the aerogel.

The coupling of superhydrophobicity and highly porous structure in BN aerogels open up a potential application in oil absorption. The absorption capacity of BN is quite high,[47] and we have shown elsewhere that BN aerogels are also good oil absorbers, with an absorption capacity of up to 1500%.[26] In addition, the BN aerogel is highly thermally stable, so it can be regenerated following oil absorption by burning in a flame or by annealing in air at 650 °C. The nanoscale structure is retained following regeneration, and its oil absorption capacity is almost completely restored. This ability to be regenerated and re-used would make BN aerogels more cost-efficient for use in environmental clean-up projects.

References

(1) Pei, S.; Cheng, H.-M. *Carbon* **2012**, *50*, 3210–3228.
(2) Yang, D.; Velamakanni, A.; Bozoklu, G.; Park, S.; Stoller, M. D.; Piner, R. D.; Stankovich, S.; Jung, I.; Field, D. A.; Ventrice, C. A.; Ruoff, R. S. *Carbon* **2009**, *47*, 145–152.
(3) Gao, X.; Jang, J.; Nagase, S. *J. Phys. Chem. C* **2010**, *114*, 832–842.
(4) Gao, W.; Alemany, L. B.; Ci, L.; Ajayan, P. M. *Nat. Chem.* **2009**, *1*, 403–408.
(5) Bagri, A.; Mattevi, C.; Acik, M.; Chabal, Y. J.; Chhowalla, M.; Shenoy, V. B. *Nat. Chem.* **2010**, *2*, 581–587.
(6) Goldstein, A. P.; Mickelson, W.; Machness, A.; Lee, G.; Worsley, M. A.; Woo, L.; Zettl, A. *submitted* **2014**.
(7) Li, D.; Müller, M. B.; Gilje, S.; Kaner, R. B.; Wallace, G. G. *Nat. Nanotechnol.* **2008**, *3*, 101–105.
(8) Yumitori, S. *J. Mater. Sci.* **2000**, *35*, 139–146.
(9) Kushita, K. N.; Hojou, K. *Ultramicroscopy* **1991**, *35*, 289–293.
(10) Nemanich, R.; Lucovsky, G.; Solin, S. *Solid State Commun.* **1977**, *23*, 117–120.
(11) Ferrari, A. C.; Basko, D. M. *Nat. Nanotechnol.* **2013**, *8*, 235–246.
(12) Golberg, D.; Bando, Y.; Tang, C. C.; Zhi, C. Y. *Adv. Mater.* **2007**, *19*, 2413–2432.
(13) Cohen, M. L.; Zettl, A. *Phys. Today* **2010**, *63*, 34–38.
(14) Golberg, D.; Bando, Y.; Huang, Y.; Terao, T.; Mitome, M.; Tang, C.; Zhi, C. *ACS Nano* **2010**, *4*, 2979–2993.
(15) Paine, R. T.; Narula, C. K. *Chem. Rev.* **1990**, *90*, 73–91.
(16) Lindquist, D. A.; Borek, T. T.; Stephen, J.; Narula, C. K.; Johnston, G.; Schaeffer, R.; Smith, D. M.; Paine, R. T. *J. Am. Ceram. Soc.* **1990**, *73*, 757–760.
(17) Dibandjo, P.; Bois, L.; Chassagneux, F.; Miele, P. *J. Eur. Ceram. Soc.* **2007**, *27*, 313–317.
(18) Han, W.-Q.; Bando, Y.; Kurashima, K.; Sato, T. *Appl. Phys. Lett.* **1998**, *73*, 3085.
(19) *CRC Handbook of Chemistry and Physics*; 81st ed.; CRC Press: Boca Raton, FL, 2000.
(20) Golberg, D.; Bando, Y.; Han, W.-Q.; Kurashima, K.; Sato, T. *Chem. Phys. Lett.* **1999**, *308*, 337–342.

(21) Han, W.-Q.; Cumings, J.; Huang, X.; Bradley, K.; Zettl, A. *Chem. Phys. Lett.* **2001**, *346*, 368–372.
(22) Han, W.-Q.; Brutchey, R.; Tilley, T. D.; Zettl, A. *Nano Lett.* **2004**, *4*, 173–176.
(23) Han, W.-Q.; Yu, H.-G.; Liu, Z. *Appl. Phys. Lett.* **2011**, *98*, 203112.
(24) Rousseas, M.; Goldstein, A. P.; Mickelson, W.; Worsley, M. A.; Woo, L.; Zettl, A. *ACS Nano* **2013**, *7*, 8540–8546.
(25) Worsley, M. A.; Kucheyev, S. O.; Mason, H. E.; Merrill, M. D.; Mayer, B. P.; Lewicki, J.; Valdez, C. A.; Suss, M. E.; Stadermann, M.; Pauzauskie, P. J.; Satcher, J. H.; Biener, J.; Baumann, T. F. *Chem. Commun.* **2012**, *48*, 8428–8430.
(26) Pham, T.; Goldstein, A. P.; Lewicki, J.; Kucheyev, S. O.; Wang, C.; Russell, T. P.; Worsley, M. A.; Woo, L.; Mickelson, W.; Zettl, A. *submitted* **2014**.
(27) Li, Z. Q.; Lu, C. J.; Xia, Z. P.; Zhou, Y.; Luo, Z. *Carbon* **2007**, *45*, 1686–1695.
(28) Thomas, J. J.; Weston, N. E.; O'Connor, T. E. *J. Am. Chem. Soc.* **1963**, *84*, 4619–4622.
(29) Sato, T. *Proc. Japan Acad. Ser. B* **1985**, *61*, 459–464.
(30) Moussa, G.; Salameh, C.; Bruma, A.; Malo, S. *Inorganics* **2014**, *2*, 396–409.
(31) Worsley, M. A.; Olson, T. Y.; Lee, J. R. I.; Willey, T. M.; Nielsen, M. H.; Roberts, S. K.; Pauzauskie, P. J.; Biener, J.; Satcher, J. H.; Baumann, T. F. *J. Phys. Chem. Lett.* **2011**, *2*, 921–925.
(32) McAllister, M. J.; Li, J.-L.; Adamson, D. H.; Schniepp, H. C.; Abdala, A. A.; Liu, J.; Herrera-Alonso, M.; Milius, D. L.; Car, R.; Prud'homme, R. K.; Aksay, I. A. *Chem. Mater.* **2007**, *19*, 4396–4404.
(33) Marchetti, P. S.; Kwon, D.; Schmidt, W. R.; Interrante, L. V; Maciel, G. E. *Chem. Mater.* **1991**, *3*, 482–486.
(34) Wang, C.; Lee, D. H.; Hexemer, A.; Kim, M. I.; Zhao, W.; Hasegawa, H.; Ade, H.; Russell, T. P. *Nano Lett.* **2011**, *11*, 3906–3911.
(35) Tumbleston, J. R.; Collins, B. A.; Yang, L.; Stuart, A. C.; Gann, E.; Ma, W.; You, W.; Ade, H. *Nat. Photonics* **2014**, *8*, 385–391.
(36) Collins, B. A.; Cochran, J. E.; Yan, H.; Gann, E.; Hub, C.; Fink, R.; Wang, C.; Schuettfort, T.; McNeill, C. R.; Chabinyc, M. L.; Ade, H. *Nat. Mater.* **2012**, *11*, 536–543.
(37) Gann, E.; Young, A. T.; Collins, B. A.; Yan, H.; Nasiatka, J.; Padmore, H. A.; Ade, H.; Hexemer, A.; Wang, C. *Rev. Sci. Instrum.* **2012**, *83*, 045110.
(38) Ilavsky, J. *J. Appl. Crystallogr.* **2012**, *45*, 324–328.
(39) Terminello, L. J.; Chaiken, A.; Lapiano-Smith, D. A.; Doll, G. L.; Sato, T. *J. Vac. Sci. Technol. A* **1994**, *12*, 2462–2466.
(40) Kucheyev, S. O.; Hamza, A. V; Satcher Jr., J. H.; Worsley, M. A. *Acta Mater.* **2009**, *57*, 3472–3480.
(41) Oliver, W. C.; Pharr, G. M. *J. Mater. Res.* **1992**, *7*, 1564–1583.
(42) Li, G.-X.; Liu, Y.; Wang, B.; Song, X.-M.; Li, E.; Yan, H. *Appl. Surf. Sci.* **2008**, *254*, 5299–5303.
(43) Pakdel, A.; Zhi, C.; Bando, Y.; Nakayama, T.; Golberg, D. *ACS Nano* **2011**, *5*, 6507–6515.
(44) Rafiee, J.; Mi, X.; Gullapalli, H.; Thomas, A. V.; Yavari, F.; Shi, Y.; Ajayan, P. M.; Koratkar, N. A. *Nat. Mater.* **2012**, *11*, 217–222.
(45) Cassie, A. B. D.; Baxter, S. *Trans. Faraday Soc.* **1944**, *40*, 546.
(46) Pakdel, A.; Bando, Y.; Golberg, D. *Langmuir* **2013**, *29*, 7529–7533.
(47) Lei, W.; Portehault, D.; Liu, D.; Qin, S.; Chen, Y. *Nat. Commun.* **2013**, *4*, 1777.